Development of Microstrip-Coupled Lumped-Element Kinetic Inductance Detectors for Astronomy

A thesis submitted in partial fulfilment of the requirements

for the degree of

Doctor of Philosophy

by

Amber Loren Hornsby

November 2020

Abstract

Lumped-element Kinetic Inductance Detectors (LEKIDs) are superconducting Inductor-Capacitor (LC) resonators that have been utilised in large-format arrays of detectors for millimetre-wave astronomy. LEKIDs are highly multiplex-able by design and have been demonstrated to reach the photon-noise limit required for astronomy. However, coupling such structures directly to low loss superconducting transmission lines and filtering structures has proved challenging. The research presented in this thesis is aimed at developing techniques for coupling a LEKID to an antenna structure and microwave transmission line, which would be compatible with existing device architecture used in existing Cosmic Microwave Background (CMB) experiments.

Several important developments towards realising large arrays of multi-chroic, polarisation-sensitive pixels suitable for future Cosmic Microwave Background experiments are presented in this thesis. These include coupling a Kinetic Inductance Detector (KID) to an antenna and microstrip, which is made possible by the separated inductor and capacitor architecture of a LEKID. The results presented in this thesis demonstrate that a dielectric can be deposited over the inductor only, to form a coupling microstrip structure, while leaving the LEKID relatively immune to the noise created by the typically noisy dielectrics. The section of microstrip between the antenna and KID can then be utilised to introduce on-chip filtering structures which limit the band of frequencies reaching the detector. Initial measurements of single-colour prototype devices suggest the current devices are susceptible to stray light, an issue that needs to be considered in future design iterations. However, the overall results presented in this thesis still represent an important step towards realising large arrays of multi-chroic, polarisation-sensitive detectors required for future studies of the CMB.

Contents

List of Figures

List of Tables

List of Acronyms

ADS Advanced Design System

AC Alternating Current

BCS Bardeen, Cooper, Schrieffer theory

BP Band-pass (filter)

CMB Cosmic Microwave Background

CPW CoPlanar Waveguide

DAQ Data Acquisition System

DC Direct Current

EM ElectroMagnetic

FFT Fast Fourier Transform

FWHM Full Width Half Maxima

G-R Generation Recombination (noise)

IDC InterDigital Capacitor

IQ In-phase and Quadrature

KID Kinetic Inductance Detector

LC Inductor-Capacitor (circuit)

LEKID Lumped-Element Kinetic Inductance Detector

LNA Low Noise Amplifier

LO Local Oscillator

LPE Low-Pass-Edge (filter)

mc-LEKID microstrip-coupled LEKID

NEP Noise Equivalent Power

PSD Power Spectral Density

RF Radio Frequency

RLC Resistor-Inductor-Capacitor (circuit)

SNR Signal to Noise Ratio

SQUID Superconducting QUantum Interference Device

TES Transition Edge Sensor

TLS Two-Level System (noise)

VNA Vector Network Analyser

List of Variables

α Kinetic inductance fraction [Dimensionless]

β Imaginary component of the propagation constant, γ [dB/m]

δ_0 Dielectric loss tangent [Dimensionless]

Δ Superconducting energy gap [eV]

$\mathbf{\Delta_0}$ Superconducting energy gap at 0 K [eV]

$\mathbf{\Delta f}$ Filter bandwidth [Hz]

ϵ Dielectric constant [Dimensionless]

ϵ_{r} Relative dielectric constant [Dimensionless]

η Quasi-particle creation efficiency factor [Dimensionless]

Θ Angular distance from the antenna/lenslet system [Degrees]

λ Wavelength [m]

$\mathbf{\lambda_c}$ Characteristic wavelength of transmission line [m]

$\mathbf{\lambda_L}$ London penetration depth [m]

$\mathbf{\lambda_L(0)}$ London penetration depth at 0 K [m]

$\mathbf{\mu_0}$ Permeability of vacuum [H/m]

$\mathbf{\nu_s}$ Superconducting electron velocity [m/s]

ρ Resistivity [Ωm]

σ Conductivity [S/m]

σ_1 Real component of conductivity [S/m]

σ_2 Imaginary component of conductivity [S/m]

σ_{amp} Amplifier noise [W/Hz$^{1/2}$]

σ_{n} Normal-state conductivity [S/m]

σ_{s} Conductivity due to the superconducting electron population [S/m]

σ_{tot} Total conductivity [S/m]

τ Characteristic scattering time [s]

τ_{qp} Quasi-particle lifetime [s]

τ_{res} Resonator ringdown time [s]

τ_0 Characteristic electron-phonon interaction time [s]

ω Angular frequency [rad/s]

ω Angular frequency of microwave probe signal [rad/s]

ω_0 Resonant frequency [rad/s]

ω_{res} Resonant frequency of a resonator coupled to the feedline [rad/s]

ϕ Beam radiation pattern about the Y-axis [Degrees]

Ψ Complex di-gamma function [Dimensionless]

$\hbar$ Reduced Planck constant [J/s]

$\mathbf{A}$ Magnetic vector potential [Tm]

$\mathbf{A}$ Cross-sectional area [m^2]

$\mathbf{A_f}$ A parameter of ABCD matrix for a one-stub filter [Dimensionless]

$\mathbf{A_L}$ A parameter of ABCD matrix for a microwave transmission line [Dimensionless]

$\mathbf{A_S}$ A parameter of ABCD matrix for a filter stub [Dimensionless]

$\mathbf{B}$ Magnetic flux [Wb]

$\mathbf{B_f}$ B parameter of ABCD matrix for a one-stub filter [Dimensionless]

$\mathbf{B_L}$ B parameter of ABCD matrix for a microwave transmission line [Dimensionless]

$\mathbf{B_S}$ B parameter of ABCD matrix for a filter stub [Dimensionless]

$\mathbf{C}$ Capacitance [F]

$\mathbf{C_c}$ Coupling capacitance [F]

$\mathbf{C_f}$ C parameter of ABCD matrix for a one-stub filter [Dimensionless]

$\mathbf{C_L}$ C parameter of ABCD matrix for a microwave transmission line [Dimensionless]

$\mathbf{C_{res}}$ Capacitance of resonator [F]

$\mathbf{C_S}$ C parameter of ABCD matrix for a filter stub [Dimensionless]

$\mathbf{D_f}$ D parameter of ABCD matrix for a one-stub filter [Dimensionless]

$\mathbf{D_L}$ D parameter of ABCD matrix for a microwave transmission line [Dimensionless]

$\mathbf{D_S}$ D parameter of ABCD matrix for a filter stub [Dimensionless]

$\mathbf{d}$ Distance between neighbouring filter stubs [m]

$\mathbf{E}$ Electric field strength [V/m]

$\mathbf{E}$ Energy of photon (in Mattis Bardeen equations) [J]

$\mathbf{E_{stored}}$ Energy stored in system [J]

e Charge of electron [J]

e_{shot} Photon shot noise [W/Hz$^{1/2}$]

e_{wave} Photon wave noise [W/Hz$^{1/2}$]

f Frequency [Hz]

f_0 Resonant frequency [Hz]

F Fill factor [Dimensionless]

I Current [A]

I Real component of S_{21} [V]

I_{loss} Current loss via coupling capacitor [A]

I_0 Modified bessel function of first kind [Dimensionless]

J Current density [A/m^2]

J_{qp} Current density due to n_{qp} [A/m^2]

J_s Current density due to n_s [A/m^2]

J_{tot} Total current density [A/m^2]

K_0 Modified bessel function of second kind [Dimensionless]

k_b Boltzmann constant [J/K]

L Inductance [H]

L_g Geometric inductance [H]

L_{int} Internal inductance [H]

L_k Kinetic inductance [H]

L_m Magnetic inductance [H]

L_{total} Total inductance [H]

l Length of filter stub or feedline [m]

m_e Effective electron mass [kg]

n Number density of electrons [e$^-$ per m^{-3}]

n_{qp} Number density of quasi-particles [e$^-$ per m^{-3}]

n_s Number density of superconducting electrons [e$^-$ per m^{-3}]

N_G Number of quasi-particles generated per second [Number of particles/s]

N_{qp} Number of quasi-particles [Number of particles]

N_R Number of quasi-particles generated per second [Number of particles/s]

N_s Normalised quasi-particle density of states [μm^{-3} eV^{-1}]

N_{xs} Excess number of quasi-particles [Number of particles]

$\mathbf{N_0}$ Single spin density of states at the Fermi level [μm^{-3} eV^{-1}]

$\mathbf{N_{xs}}$ Excess number of quasi-particles [Number of particles]

NEP Noise equivalent power [W/Hz$^{1/2}$]

$\mathbf{NEP_{GR}}$ Noise equivalent power due to generation-recombination noise [W/Hz$^{1/2}$]

$\mathbf{NEP_{photon}}$ Noise equivalent power due to photon noise [W/Hz$^{1/2}$]

$\mathbf{P_{opt}}$ Optical power [W]

$\mathbf{P_{loss}}$ Energy loss per cycle [J]

Q Imaginary component of S_{21} [V]

Q Quality factor [Dimensionless]

$\mathbf{Q_c}$ Coupling quality factor [Dimensionless]

$\mathbf{Q_i}$ Intrinsic quality factor [Dimensionless]

$\mathbf{Q_{tot}}$ Total quality factor [Dimensionless]

R Resistance [Ω]

$\mathbf{R_{det}}$ Total detector responsivity [Dimensionless]

$\mathbf{R_n}$ Normal-state resistance [Ω]

$\mathbf{R_s}$ Surface resistance [Ω/□]

$\mathbf{S_N}$ Power spectral density[N^2/Hz.]

T Temperature [K]

t Film thickness [m]

$\mathbf{T_c}$ Characteristic critical temperature [K]

$\mathbf{U_k}$ Total kinetic inductance per unit length [H/m]

$\mathbf{V_c}$ Voltage [V]

$\mathbf{V_{Al}}$ Absorbing volume of detector [m^3]

$\mathbf{V_T}$ Volume of detector [m^3]

W Width of film [m]

$\mathbf{W_e}$ Average energy stored in the capacitor [J]

$\mathbf{W_m}$ Average energy stored in the inductor [J]

$\mathbf{X_s}$ Surface reactance [Ω/□]

$\mathbf{x_r}$ Fractional frequency shift of the resonator [Dimensionless]

$\mathbf{Z_C}$ Impedance of capacitive side of the circuit [Ω]

$\mathbf{Z_{Cc}}$ Impedance of coupling capacitor [Ω]

$\mathbf{Z_{in}}$ Input impedance [Ω]

$\mathbf{Z_L}$ Impedance of inductive side of the circuit [Ω]

$\mathbf{Z_{res}}$ Total impedance of the resonator (excluding coupling capacitor) [Ω]

$\mathbf{Z_s}$ Surface impedance [$\Omega/\square$]

$\mathbf{Z_{tot}}$ Total impedance of the resonator (including coupling capacitor) [Ω]

$\mathbf{Z_0}$ Characteristic impedance of transmission line [Ω]

To my beautiful cat, little North.

You were the best thesis buddy.

I'll miss you so much.

Acknowledgements

The last eight years in the wonderful city of Cardiff, Wales, the majority of my adult life, have been incredible. From the beauty of the trees in Bute Park to all the coffee shops who have kept me caffeinated throughout, I will forever be grateful for being adopted by this lovely, Welsh city. Diolch yn fawr.

I would like to acknowledge my fantastic supervisors – Simon Doyle and Pete Barry. Thank you for your support over the last few years, Simon. You've always been patient and kind, whilst encouraging me to achieve the best I can. And thank you, Pete, for always helping me get through tricky (read last minute) work for deadlines and for you, Kayleigh and Hendrix hosting me in Chicago. To my brilliant collaborators, Erik Shirokoff and Amy Tang – thank you! I hope we get to work together again in the future.

From trips to the pub and technical support in the lab, my PhD wouldn't have been possible without the lovely people I've worked with during my time at Cardiff. To my fellow PhD pals – you're fantastic and you will (if you haven't already) finish this thing. Thank you to my fellow Ladies Wot Science for a constant supply of pet photos and to my Virtual Writing Group.

Thank you so much to everyone in the astronomy instrumentation group for having me for almost 8 years. To Sam Rowe, Georgina Klemencic, Nadia Aoudjane and Paul Moseley – thank you for always being there to cheer me on when things were tough and to help me celebrate every little success. Thank you to Enzo Pascale, Chris Dunscombe and Andreas Papageorgiou for sharing expertise over the years and making my work possible. For introducing me to the joys of astronomy instrumentation back in 2013, and your continuous support and guidance since, thank you Peter Ade and Carole Tucker. I honestly can't imagine doing anything else.

Whilst in Cardiff, I have been fortunate enough to live with some truly wonderful

people whose support I couldn't have done this without. So thank you to Luke Berry, Reva Pandya, Nathan Ahmed, Matthew Rhys Jones, Georgia Gillard, Jess Price, Hannah Chawner (and, unofficially, Andrew May), Kirsty Richards, Ciaran Hiscox, Kane Bailey and Emma Williams. Thank you for years of fun and laughter over many cups of tea, coffee and the occasional glass of prosecco. And, although I've never officially lived with Dan Neenan, Rahul Modhvadia, Matthew Peach and, of course, Kieran Flay, I've spent so much time with you all that I might as well have. I love you all so much. Thank you and I suspect, unfortunately for you all, that you'll probably never be free of me. Here's to all of the future weddings we'll dance at and all of the babies I'll be a cool auntie to.

I'm also lucky enough to have some very special friends outside of Cardiff. To Suzanne Callighan, thank you for some truly wonderful times over the years that usually involved prosecco and pizza with Hannah and Georgia. You three really made sure I took a step back from Physics and had some fun. To Alice Booth, the best thing to come out of my brief time at Oxford, thank you so much for your constant support, photos of Ollie and incredible music suggestions. You are amazing. To Mike Adams, thank you for always being there throughout my (many!) physics-related meltdowns over the years and for reliably being a night owl during my terrible thesis writing hours. I think it's your turn to buy coffee?

I owe a lot of my success to the phenomenal support my family have given me over the years. Starting with my little dog George, my big ginger bean cat, Simba and to my princess Luton – thanks for being the best pets ever. To my wonderful Grandma and Grandad, I love you both and thanks for incredible and continuous support. To my mum, thank you for encouraging my love of science and learning from a young age, and for taking me to Sherwood observatory all those years ago. Also, for always answering the phone. To my dad, thank you for only complaining a little every time I needed help moving and for calling me a rocket scientist. It's not a particularly accurate title, but it let me know that you were proud of me. To my little sister, the inspirational Jade Loren Hornsby, thank you for cheering me up with talk of chicky nuggies and smol puppers. You really are the best sister in the Universe and I hope you're as proud of me as I am of you.

"Sometimes you need darkness to see. Sometimes you need light"

– *Sara Seager*

1

Introduction

Observing the temperature and polarisation fluctuations of the Cosmic Microwave Background (CMB) offer a unique insight into how our Universe began. The signature of the hidden, polarised B-modes are vital for testing models of inflation, making the detection of primordial B-modes one of the main objectives for future CMB experiments [1, 2].

Current experiments, with focal planes based on arrays of Transition-Edge Sensors (TESs), now routinely operate with sensitivity close to the background-limit [3, 4, 5]. With detectors typically operating at the photon-noise limit, more detectors are required to further increase sensitivity. Moreover, it is now well known that observations at multiple frequencies are necessary in order to constrain and remove foreground contamination [3]. To maximise focal plane efficiency, each on-sky pixel must have dual-band, dual-polarisation sensitivity, with each pixel requiring four detectors. The large numbers of detectors required by the next generation of CMB experiments presents a significant technical challenge.

Kinetic inductance detectors (KIDs) are superconducting resonators whose res-

onant frequency and quality factor are modified with absorbed optical power [6]. Large arrays of KIDs can be constructed without the need for ancillary multiplexing components, significantly reducing the cryogenic complexity of an experiment. Currently, most existing CMB experiments implement an on-chip, microstrip-optical-coupling architecture, where radiation is guided onto a thin-film microstrip line and then routed to the detector, enabling multi-chroic, polarisation-sensitive pixels.

An example pixel (the long-term goal this research is targeting) is shown in figure 1.1. In this pixel, light is captured by an antenna, centrally located at the focus of a horn or lenslet system, before travelling down the T-junction towards the filtering system. When the transverse electric mode, TE_{11}, is incident on the antenna, it induces a signal which travels down the two opposites probes, with one signal 180 degrees out of phase with the other (see inset (a) of figure 1.1). Depending on which frequency band the signal belongs to, the signal splits at the T-junction and travels down the filtering arms towards the hybrid coupler. In the future, this could easily be extended to a triplexer filtering system, targeting three frequency bands instead of two [4]. The hybrid coupler is necessary to select a mode of polarisation by operating as a 180-degree power combiner. If the signals on port 3 and 4 are 180 degrees out of phase, then they are added together and are directed towards the detector (see inset (b) of figure 1.1). If they are in phase, then the signals are directed towards port 2 and absorbed by a length of transmission line (not shown in diagram).

To take advantage of existing CMB pixel architecture, and the separated inductive and capacitive elements of a lumped-element KID (LEKID), a new type of device architecture has been developed - the microstrip-coupled LEKID (mc-LEKID) [7, 8]. The goal of the mc-LEKID is to provide a simple and reliable design for coupling a microstrip transmission line structure to a LEKID. Here, the resonator inductor doubles both as a high-Q microwave lumped-element inductor and an absorbing millimetre-wave microstrip line. Radiation is collected by an antenna and guided along a microstrip line which is galvanically connected to the centre of a hairpin-style inductor. Any radiation incident along the input microstrip line is split and is absorbed along the length of the inductor. Feeding at the centre of the inductor enables a direct connection to the microwave resonator without affecting

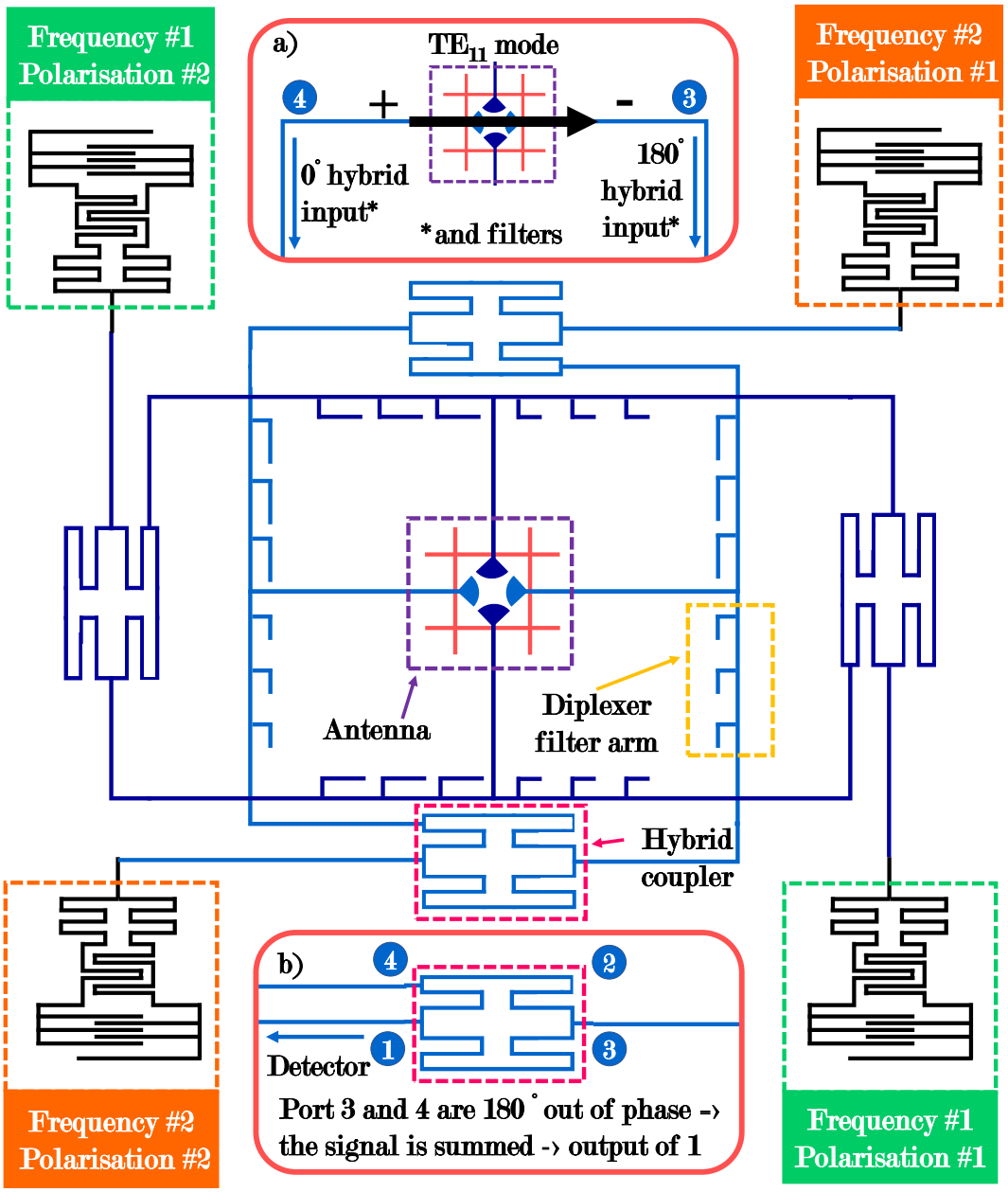

Figure 1.1: An ideal pixel design for multi-chroic, polarisation-sensitive observations. Light is captured by the antenna structure in the centre of the pixel before travelling down the diplexer T-junction. Depending on the frequency of the signal, the signal splits and travels down the filtering diplexer arms towards the hybrid coupler. The hybrid coupler selects one mode, coupled in via the antenna structure (a), which enables polarisation selection before being deposited onto a detector (b).

the performance of the resonator system. Here, the microstrip-inductor connection must be an impedance-matched junction to minimise reflection back towards the antenna, enabling the signal to see a smooth transition.

However, the microstrip dielectric is formed from an amorphous dielectric material that is deposited over the KID, which has a tendency to degrade the quality factor and low-frequency noise performance of the KID resonator through the introduction of two-level systems (TLSs) [9, 10]. It is possible to restrict lossy dielectrics to regions of the device where the electric field is low, owing to the spatially separated architecture of a LEKID.

Separating out L and C provides a region of reduced electric field density in the inductive meander section, enabling an amorphous dielectric to be added without the device becoming susceptible to TLSs. The result of which is a reduced predisposition to dielectric loss tangents, which limit the detector's quality factors (where high quality factors are advantageous for multiplexing) and a decreased susceptibility to TLS noise contributions [11].

Coupling the LEKID to a microstrip transmission line is an important step towards realising the large arrays of multi-chroic, polarisation-sensitive pixels required for future CMB experiments. This is because once the microstrip coupling is proven, it is simple to utilise the transmission line to add the filtering structures and hybrid structures depicted in figure 1.1.

1.1 Cosmic Microwave Background

The concept of an overall temperature for the Universe has been discussed since the late 19^{th} century, following the theoretical and experimental confirmation of the relationship between bolometric flux and temperature of a blackbody by Stefan and Boltzmann [12, 13]. Some of the earliest estimations of the temperature of space include: (i) 5-6 K by Guillaume in 1986, and (ii) 3.18 K by Eddington in 1926, who estimated the non-thermal radiation of starlight in the galaxy [14, 15]. It is important to note that this work pre-dates Hubble's proof of the existence of external galaxies in 1926 [16].

By the 1950s, Gamow was regularly trying to predict the actual temperature of

interstellar space, starting at 50 K before refining estimates to 7 K and 6 K [17, 18]. Alpher and Herman also put forward temperatures of 5 K and later 28 K, whilst Dicke proposed 40 K [18]. Dicke, Peebles and Wilkinson believed the CMB signal, composed of radiation from the Big Bang, should be detectable but it will have been red-shifted to microwave frequencies [19]. However it wasn't until 1964 that theory and experiments came together when Penzias and Wilson, using a 20-foot horn-reflector antenna, detected the CMB [20]. This represents a major milestone for modern cosmology, shifting the Big Bang versus Steady State Universe debate in favour of the former [21].

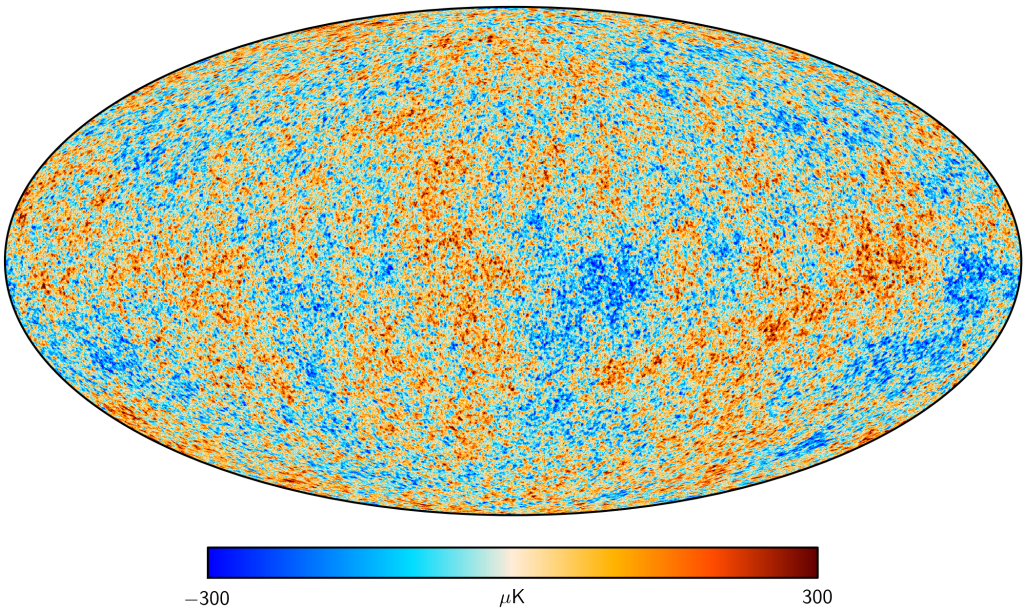

Figure 1.2: Planck's view of the Universe - a full-sky map of the temperature fluctuation in the Cosmic Microwave Background. *Image credit: ESA and the Planck Collaboration.*

The CMB is a faint background radiation which fills all of space, consisting of the oldest photons in the Universe, with a peak wavelength and temperature (as determined by Wien's peak in the blackbody intensity spectrum) of 1 mm and 2.73 K [22, 23]. It is homogeneous and isotropic in nature, but as technology improved in both sensitivity and resolution, tiny temperature fluctuations (anistrophies) emerged from the uniformity and were first observed by Smoot, Gorenstein and Muller in 1977 [24]. The most recent all-sky observations of the temperature fluctuations, as measured by the Planck satellite, are shown in figure 1.2 [25].

In accordance with standard cosmology, the CMB is a snapshot of the Universe once it had expanded and had therefore cooled enough for protons and electrons to combine to form hydrogen, allowing photons to travel freely. This is known as the surface of last scattering and represents a time when the Universe was 380,000 years old [26]. Moreover due to Thompson scattering of radiation in the early Universe, before hydrogen could form, the CMB is linearly polarised [27]. Information gained through measurements of the polarisation is complementary to information from temperature anisotropies, but the signal is much smaller in amplitude and is therefore more difficult to measure.

1.1.1 B-modes - Hidden in the Anisotropies

Measurements of the CMB anisotropies provide valuable information about the early Universe, the formation of large-scale structure and the cosmological parameters which govern the Universe. The need for better, more sensitive measurements is heavily motivated by the search for one of the most compelling pieces of evidence for and predicted by inflation - the detection of B-modes.

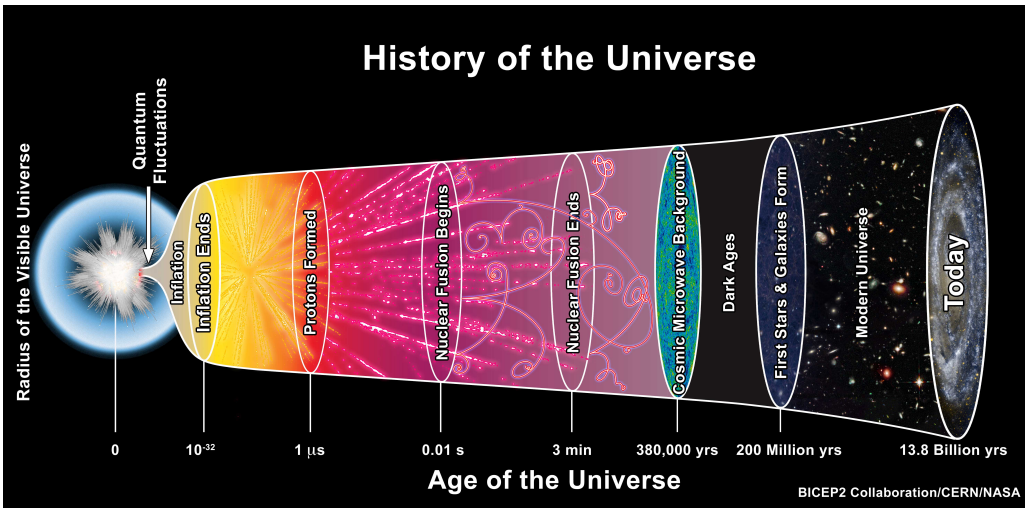

Figure 1.3: The history of the Universe, depicting the timeline of quantum fluctuations growing to form the Universe observed today, made possible by a rapid period of expansion - Inflation. *Image credit: BICEP2 Collaboration/CERN/NASA*

Predicted by Guth in 1981, inflation represents a period of time when the Universe undertook a period of rapid expansion and is the accepted explanation for

how the primordial density perturbations grew into the CMB anistrophies we observe today [28]. Moreover, if inflation theory is correct, it predicts the existence of a primordial gravitational wave which will have imprinted a characteristic polarisation pattern in the CMB - the B-modes [28, 29]. As depicted by figure 1.3, the maximum lookback time is set by the oldest photons, the photons from the CMB, whereas detecting the B-modes, the primordial gravitational wave, opens up a new window to study the Universe at the earliest possible moment.

A detection of the B-mode polarisation pattern will provide great insight into the very early Universe because the strength of the signal, encoded in the tensor-to-scalar ratio r, provides a direct measurement of the expansion rate of the Universe during inflation [30]. Combined observations from Planck, the BICEP2/Keck Array through the 2015 season and WMAP placed an upper constraint of $r < 0.06$ [31]. The smaller the r, the more difficult it becomes to detect and the more theories of inflation get ruled out.

Improved measurements of the CMB will yield much more information than just the B-modes. From the nature of dark matter to the properties of neutrinos, the wealth of information extracted from measurements of the CMB, combined with information from other wavelengths, will benefit many astronomers [30]. The next generation of experiments, often referred to as CMB-Stage-4 experiments (CMB-S4), are expected to uncover many secrets the Universe is hiding with their improved sensitivity and resolution, and already has an impressive set of instrumental requirements [32].

1.1.2 Focal-plane Requirements

For a ground-based instrument targeting the CMB, the basic requirements for the detector focal plane revolve around three main themes: (i) multiple frequencies for the removal of galactic foregrounds (ii) sensitivity to polarisation and (iii) many photon-noise-limited detectors. Current telescopes with cutting-edge instruments are successfully tackling the first two themes, based on a pixel architecture similar to that depicted in figure 1.1; the third requirement, a large number of detectors operating at the photon-noise limit, although improving with every new instrument, still requires some development.

To measure a clean CMB signal and correctly calculate cosmological parameters, it is crucial to remove contaminating galactic foreground which requires spectral observations at multiple frequencies [33]. In a ground-based microwave experiment, there are four useful atmospheric transmission windows available, including: 30-50 GHz, 75-110 GHz, 130-170 GHz and a wide band from 200-325 GHz. To characterise foreground components, such as thermal dust shown in figure 1.4, it is a balance between large bandwidths which enable fast mapping speeds and the need for narrower frequency bands to resolve all of the necessary spectral features. Thus future experiments, such as the ground-based CMB-S4, will target multiple frequency bands within the atmospheric windows [32].

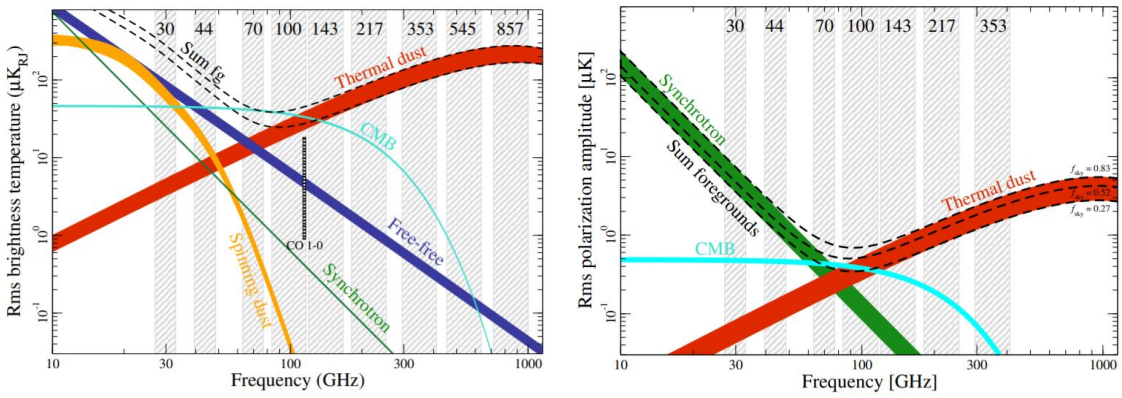

(a) (b)

Figure 1.4: The brightness temperature rms as a function of frequency and astrophysical component for temperature (left) and polarisation (right), as observed by Planck. *Image credit: Planck Collaboration* [34, 35]

Many ground-based experiments for mapping the CMB typically include filtering structures on the device wafer, between the antenna and detector, to limit the incoming frequencies [36, 37, 38, 39, 40]. On-chip filters, such as the distributed style implemented by ACTPol, are often composed of microstrip transmission lines to form quarter-wave resonating stubs [38]. Increasing the number of stubs, or poles, provides greater control over the pass-band of the filter, but can lead to an overall reduction in filter transmission due to dielectric losses [41].

Moreover, as indicted by the polarised astrophysical components in figure 1.4, it is also crucial to measure the CMB and contaminating foregrounds at multiple

frequencies. Thus, it is advantageous for detectors to be sensitive to both linear polarised components on chip. For example, horn-coupled ACTPol achieves this through the combination of an orthomode transducer (OMT), to separate the two polarised components, and hybrid-T structure to ensure only the desired component of the separated polarised signal reaches its destined detector [38].

Ground-based experiments have successfully implemented arrays of multi-chroic, polarisation-sensitive detectors, however, many have comparatively low numbers of detectors which restrict mapping speeds and thus impact the instruments ability to make the highly resolved and incredibly sensitive maps of the CMB required to measure B-modes. CMB-S4 is targeting 500,000 TES bolometers, which is a huge increase in detector numbers compared to stage-3 experiments like SPT-3G which has 15,234 detectors [32, 4].

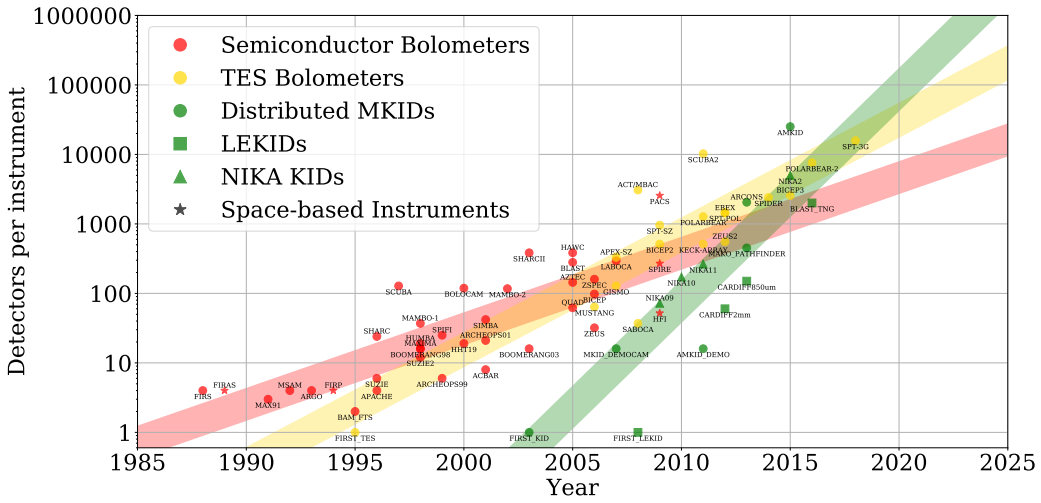

Figure 1.5: A history of millimetre/sub-millimetre experiments. Here, the detector counts per instrument count as a function of time are shown for bolometers (*red*), TES bolometers (*yellow*) and KIDs (*green*). Space-based instruments are indicated by star markers. *Image credit: Dr Sam Rowe, Cardiff University* [42]

It is this requirement of large arrays of detectors where KIDs can be most advantageous over TESs, as historical instruments trends in figure 1.5 suggest detector numbers are increasing more rapidly in KIDs than TESs. One explanation is TESs have a more complicated detector readout system due to the separated nature of their detector and detector-readout planes - both of which require cryogenic cooling. In

fact, more recent deployments of TES-based CMB instruments have implemented a detector readout systems based on coupling superconducting quantum interference devices (SQUIDs) to LC resonators to reduce the amount of cryogenic wiring required [43, 44, 45]. Thus, if large arrays of detectors are required to improve CMB measurements, the next step is to simplify the detector and readout system further by realising a instrument based on KIDs.

1.2 Kinetic Inductance Detectors

Since their initial realisation in the early 2000s, Kinetic Inductance Detectors (KIDs) have become a promising candidate detector for the next generation of astronomical imaging systems which require large-format arrays [6].

Principally, KIDs are superconducting pair-breaking detectors whose resonant frequency and quality factor are modified upon absorption of a photon with an energy $h\nu > 2\Delta$, comprising of a resistor-inductor-capacitor (RLC) circuit with a resonance frequency of $\omega_0 = 1/\sqrt{LC}$. Within the superconducting film, there are two main populations of charge carriers: paired and unpaired electrons known as Cooper pairs and quasi-particles respectively.

The fixed inductance of the circuit is determined by the shape of the inductor, known as the geometric inductance, but the inertia of the Cooper pairs results in an additional, variable inductance - the kinetic inductance, L_k, which depends on the population density of Cooper pairs in the film. Thus, the resonant frequency f_0 has a dependence on L_k which is affected by the dynamics of the charge carriers in the superconducting film i.e pair-breaking due to photon absorption. A change in inductance also results in a change in quality factor, Q. Overall, this is the fundamental principle behind photon detection in KIDs. Both of these effects, the shift to a lower resonant frequency and broadening of the resonator response, can be seen in figure 1.6.

KIDs are patterned into superconducting films composed of metals like aluminium (Al) and titanium nitride (TiN). Due to the binding energies of Cooper pairs of 2Δ, only photons with an energy greater than 2Δ are able to break apart the Cooper pairs and be detected by KIDs, which sets a minimum detectable fre-

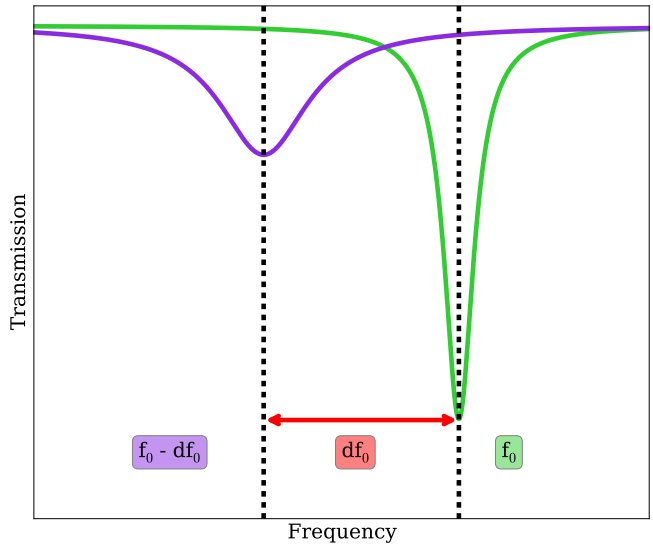

Figure 1.6: An example of a detector with a resonant frequency of f_0 (*green*) responding to photon absorption (*purple*. This results in Cooper pairs breaking, an increase in kinetic inductance and a reduction in f_0 by df_0 and a lower Q, visible as broadening of the resonance dip and reduction in dip depth.

quency for incident radiation. In aluminium, with a typical critical temperature of 1.2 K, the minimum detectable frequency is approximately 90 GHz [46]. There is no upper limit on the detectable frequencies, meaning KIDs are suitable for observations of many parts of the electromagnetic spectrum, from the infrared to X-ray frequencies and beyond.

To monitor detector response, the transmission of a microwave probe signal is measured near the resonant frequency of the resonator, where the detector appears as a simple notch filter - a resonant dip. As the total inductance changes with photon absorption, the resonance dip shifts to a lower frequency and lower Q, which is observed as a broadening resonant dip. To create an array of detectors, many resonators with a slightly different resonant frequency can be patterned on to the same superconducting film which are, in turn, read out by a comb of microwave probe frequencies set to measure the resonant dip of each detector. Because KIDs are multiplexed in frequency space this way, it is possible to read out a large number of detectors using a single set of coaxial cables, as depicted in figure 1.7. This is

advantageous over current TES-based CMB experiments as there is no need for a separate detector and detector-readout array.

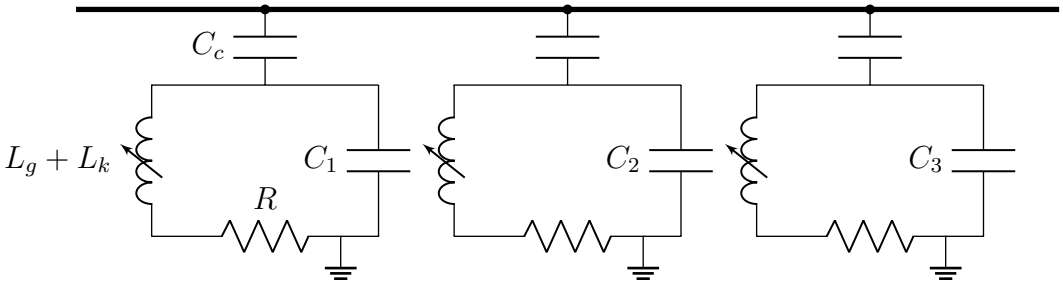

Figure 1.7: The circuit diagram for multiplexed, capacitively coupled LEKIDs, where each LEKID includes a coupling capacitor C_c, geometric inductance L_g, and resistor R. Here, if all other variables are kept the same, the resonant frequencies of each resonator can be tuned by varying the capacitance, C.

In general, there are two main categories of KID determined by the RF architecture of the detector - the distributed KID and the lumped-element KID (LEKID). A distributed KID, the original detector architecture, is a length of transmission line which is analogous to a planar microwave cavity [6]. An antenna is usually required to direct the signal to the region where the current density is highest, as this is where the detector is the most responsive. In contrast, a LEKID consists of spatially-separated inductive and capacitive elements, with a constant current density, where the meandered inductor typically doubles as an efficient free-space absorber. LEKIDs were initially realised in 2008 [7].

Once the detectors have been designed, fabricating a full array of KIDs can be relatively easy, with the most simple device formed by etching a thin-metal film grown onto a standard silicon wafer. One example of single-layer KID devices, which were realised with a single lithographic cycle and operated close to background-limited sensitivities in a passive terahertz video camera, was presented by Rowe in 2015 [42]. In this thesis, arrays of detectors range from a two-layer device composed of metal and dielectric to a more complex set of multi-layer devices requiring more challenging fabrication steps such as etching into silicon.

Moreover, it is possible to realise the multi-chroic and polarisation-sensitive elements of overall pixel design presented in figure 1.1 without the need for additional fabrication steps. This is because the filters, limiting the frequencies travelling to-

wards the detector, and the hybrid, required to ensure only one orientation of the separated polarised signal reaches the detector, are all composed of microstrip transmission line which is necessary for coupling the antenna to the absorbing meander of the LEKID. Thus, this microstrip transmission line is a key component for realising multi-chroic, polarisation-sensitive pixels - but also a concern due to its dielectric requirements.

In the design presented in this thesis, the microstrip consists of an amorphous material, silicon nitride sandwiched by a niobium transmission line and niobium groundplane. Dielectric materials are known to degrade the quality factor and low-frequency noise performance of resonators through the introduction of TLSs. TLSs may interact with an applied electric fields which drive the excited TLSs out of an equilibrium. Generally, this results in phonons being irreversibly emitted and, consequently, loss of energy in the system [9, 10, 47, 48, 49, 50].

The dielectric requirement of the microstrip, compatibility with the overall pixel architecture presented in figure 1.1, and expertise available at Cardiff University motivates the design decision to pursue a lumped-element design over a distributed resonator. Due to the spatially separated nature of the inductor and capacitor in a LEKID, it is possible to ensure the capacitor, a region where electric fields are high, is kept free of dielectric. Instead, the dielectric can be placed over the absorbing meander of the LEKID only, which reduces the susceptibility of the resonators to TLS effects.

1.3 Summary

In this chapter, a concise discussion of the astronomical motivation underpinning this research project, the CMB and desirable but undetected B-modes, is presented. Typical CMB experiments employ arrays of multi-chroic, polarisation-sensitive TESs with detector counts of around 15,000. The next generation of CMB instruments are targeting 500,000 detectors, which will require substantial technology development. Thus, focal planes require the ability to observe at multiple frequencies to remove contaminating galactic foregrounds and polarisation capabilities to uncover the B-modes.

Due to increasing detector numbers, arrays of multi-chroic, polarisation-sensitive of LEKIDs are desirable, instead of TESs, due to their ease of fabrication and built-in multiplexing capabilities, removing the need for a separate detector and detector-readout wafer within the cryogenic system. KIDs are superconducting LC resonators with a resonant frequency and quality factor modified upon absorption of a photon. LEKIDs have a spatially separated inductor and capacitor which enable the lossy dielectrics, required for the microstrip between the antenna and detector, to be incorporated in the overall pixel design. Realising an mc-LEKID is an important step towards implementing the large arrays of multi-chroic, polarisation sensitive pixels required for future CMB experiments.

1.4 Thesis outline

The thesis presents the design, fabrication and testing of microstrip-coupled-LEKIDs for future CMB experiments which require large arrays of multi-chroic, polarisation-sensitive detectors. Although well-established as a detector, both on-sky and in a controlled laboratory environment, successfully coupling a microstrip to a LEKID has yet to be realised. This thesis tackles the dielectric requirement of the microstrip to enable the addition on simple, in-line filtering structures and progress towards an optical, antenna-coupled array of devices. The contents of the subsequent chapters are as follows:

Chapter 2 : Physics of Kinetic Inductance Detectors

From superconductivity to microwave theory, chapter 2 contains a comprehensive overview of the fundamental physics required to understand how LEKIDs detect photons.

Chapter 3 : Response of LEKIDs

With the basic principles of superconductivity understood alongside the microwave perspective of resonators, it is now possible to model a LEKID. Chapter 3 is dedicated to the model and to discussions of sources of noise.

Chapter 4 : Overview of Devices

Chapter 4 focuses on the details on the different devices presented in this thesis, including physical dimensions, resonant frequencies and the process required for

device fabrication and testing.

Chapter 5 : The Dielectric Requirement

Dielectrics are known for the creation of two-levels systems noise in KIDs, but are required for microstrip coupling of an antenna to the detector. Chapter 5 presents a study into reducing the susceptibility of LEKIDs to the two-level systems noise and the impact of the dielectric requirement on detector performance.

Chapter 6 : On-chip filtering structures

With the microstrip coupling met, the addition of filtering structures to the overall device architecture can be realised, limiting the frequencies transmitted to the detector. Chapter 6 outlines the theory and design process required to create on-chip filtering structures and preliminary spectral results.

Chapter 7 : Optical Results

In Chapter 7, the response of detectors to optical power is measured for the single-colour, single-polarisation prototype device. Here, the stray-light problem is introduced and discussed.

Chapter 8 : Future work and Conclusion

For the concluding chapter, the steps required to realise a multi-chroic pixel also sensitive to polarisation are identified, guided by the lessons learned throughout this research project.

1.5 Literature Contributions

Research presented in a number of original contributions to literature are discussed throughout this thesis, including:

[11] A. L. Hornsby, P. S. Barry, S. M. Doyle, Q. Y. Tang & E. Shirokoff (2020) *"Reducing the Susceptibility of Lumped-Element KIDs to Two-Level System Effects"*. Journal of Low Temperature Physics. DOI: 10.1007/s10909-020-02501-7

– and –

[8] P. S. Barry, S. Doyle, A. L. Hornsby, A. Kofman, E. Mayer, A. Nadolski, Q. Y. Tang, J. Vieira & E. Shirokoff (2018) *"Design and performance*

of the antenna coupled lumped-element kinetic inductance detector" Journal of Low Temperature Physics. DOI: 10.1007/s10909-018-1943-y

2

Physics of Kinetic Inductance Detectors

Since its discovery in 1911, the properties of superconductors have been utilised for a variety of purposes extending from magnets for Magnetic Resonance Imaging (MRI) to the more ambitious levitating Maglev trains [51, 52, 53]. The DC electrical resistance of superconducting materials disappears when they are cooled to below their characteristic critical temperature T_c, therefore superconductors are perfect DC conductors. Another key property is summarised by the Meissner effect, meaning that bulk superconductors also expel magnetic fields when cooled below T_c, was discovered by Meissner and Ochesenfeld [54].

Kinetic inductance detectors work on the basic principle that incoming photons being absorbed break apart the Cooper pairs responsible for the phenomenon of superconductivity, this causes the resonant frequency of the inductor-capacitor circuit, that forms the basis of the KID to change, and the power absorbed from a stream of photons can be determined. Therefore to understand their operation, it is

important to understand the basics of superconductivity including: the definitions of key terms such as Cooper pairs and quasi-particles, how a resonator responds to a change in quasi-particle number, generation-recombination noise, conductivity in a superconductor and consideration of readout frequencies.

This chapter provides an overview of the LEKID, and makes use of the fundamental theory developed by the doctoral theses of S.M. Doyle, J. Gao and B. Mazin, the comprehensive review article by Zmuidzinas [7, 55, 56, 57]. Moreover, the more recent theses of colleagues, P.S. Barry, S. Rowe and J. Parrianen have also been used for guidance [58, 42, 59].

2.1 Normal State Conductivity

For current to flow in an inductor, electrons are accelerated by an electric field, causing them to gain kinetic energy and velocity, but scattering causes them to lose most of this kinetic energy, which manifests as a resistance. The resulting conductivity σ of a metal is the inverse of its resistivity ρ and can be determined using the Drude model [60].

$$\sigma_n = \frac{\sigma_0}{(1 - j\omega\tau)} = \frac{1}{\rho} \tag{2.1}$$

where $\sigma_0 = n_n e^2 \tau / m_e$, n_n is the number density of electrons per unit volume, e is the charge of an electron, τ is the average time between scattering events and m_e is the effective electron mass. Equation 2.1 can be separated into its real and imaginary components.

$$\sigma_n = \frac{n_n e^2 \tau}{m_e(1 + \omega^2\tau^2)} - j\frac{n_n e^2 \tau^2 \omega}{m_e(1 + \omega^2\tau^2)} = \sigma_1 - j\sigma_2 \tag{2.2}$$

The imaginary component arises due to electrons not being able to instantaneously change direction with the applied field. During time τ electrons will gain momentum which they must lose before changing direction, however if the time period of the field is much longer than τ then the imaginary component becomes negligible. This is true for normal metals at microwave frequencies, when the period of the applied field is $\sim$ 20 ns and is therefore much longer than τ.

Metals are formed of crystalline, periodic structures which allow plane waves to pass through without being scattered. For an electron wave, this translates to a

current flowing through a perfect crystal experiencing no resistance [61]. Therefore, when there are no thermal vibrations to disrupt the perfect lattice at absolute zero, the anticipated resistance of a metal is 0 Ω. In experiments measuring the resistance at low temperatures, however, this is not the case as most metals have a finite resistance close to 0 K [51]. But, this is not true for a superconductor which has zero DC resistance when cooled below its critical temperature T_c due to the formation of Cooper pairs.

Cooper presented the idea that weak attraction can cause pairs of electrons to exist in a bound state mediated by electron-phonon interaction [62]. It is this attraction that allows the Cooper pairs to travel through metals without scattering and without loss of kinetic energy. However due to their mass, Cooper pairs have a finite inertia which causes a delay in response to an alternating electric field. This delay manifests as an inductance, known as kinetic inductance, which is the basis of operation for a KID. To understand kinetic inductance and its dependencies, the conductivity of a superconducting metal must be considered, starting with the London model of conductivity.

2.2 London Model

The properties of a superconductor were first described mathematically by London and London in 1935 [63]. The London model assumes electron population responsible for superconductivity, denoted n_s, does not scatter. To understand the observations of experiments with superconductors, the relationship between magnetic flux $\boldsymbol{B}$ and the current density $\boldsymbol{J}$, given by Ampéres circuital law, must be considered.

$$\nabla \times \boldsymbol{B} = \mu_0 \boldsymbol{J} \tag{2.3}$$

where μ_0 is the permeability of a vacuum. If $\mathbf{B}$ is zero inside of the metal, the curl of $\mathbf{B}$ must also be zero, therefore $\mathbf{B}$ must also be zero inside of the superconductor suggesting currents exist purely on its surface [61]. However, this does not make physical sense as this sheet of current would have no thickness, suggesting an infinite current density. The solution here is for currents to flow in a thin layer of the superconductor, an expression for which was developed by the London brothers [63].

$$\boldsymbol{J} = \frac{-n_s e^2}{m_e}\boldsymbol{A} \tag{2.4}$$

where n_s is the superconducting electron density and $\boldsymbol{A}$ is the magnetic vector potential.

In an applied magnetic field, screening currents which cancel the magnetic flux inside a superconductor must flow within the surface layer. Thus, the flux density will not suddenly become zero and instead will fall slowly within the region of this current flow. The depth at which this happens at is known as the penetration depth, as it is the depth at which an external magnetic field can penetrate the superconductor [63].

$$\lambda_L = \sqrt{\frac{m_e}{\mu_0 n_s e^2}} \tag{2.5}$$

where λ_L is the London penetration depth. In normal metals, the current density and electric field ($\boldsymbol{E} = E_0 exp(j\omega t)$) are related via Ohm's law ($\boldsymbol{J} = \sigma\boldsymbol{E}$), representing a finite resistance due to the scattering of electrons. For a superconductor, where electrons do not scatter, the London equations yield a current which continuously accelerate the electrons.

$$\frac{d\boldsymbol{J}}{dt} = \frac{n_s e^2}{m_e}\boldsymbol{E} \tag{2.6}$$

Relating equation 2.6 to Ohm's law allows us to calculate the conductivity of the Cooper pairs, σ_s.

$$\sigma_s = -j\frac{n_s e^2}{\omega m} \tag{2.7}$$

To understand how a current travels through a superconducting metal, it is important to consider the two-fluid model of superconductivity.

2.3 Two-Fluid Model

Due to the formation of Cooper pairs, below T_c, two distinct populations of electrons exist in a superconductor: quasi-particles (i.e unbound electrons) and superconducting electrons (Cooper pairs), where both values are densities [64]. The ratio of the two populations is as follows:

$$n_s/n = 1 - (T/T_c)^4 \tag{2.8}$$

where n is the total electron density ($n = n_{qp} + n_s$). The variation in these two populations, as described by equation 2.8, is shown in figure 2.1.

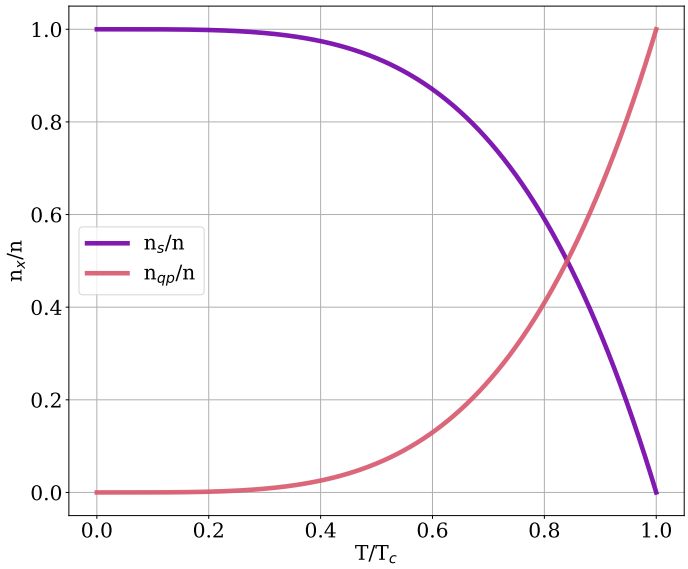

Figure 2.1: Ratio of population densities of superconducting electrons n_s and quasi-particles n_{qp} to the total population density, n, as a function of T/T_c

Having two populations of electrons allow the total current flowing in the system $\boldsymbol{J_{tot}}$ to travel down two different paths, through the quasi-particles or via Cooper pairs, where the conductivity due to n_{qp} is σ_n and σ_s is the conductivity associated with n_s. This behaviour is described by the two fluid model depicted in figure 2.2 and was developed by Bardeen in 1958 [64].

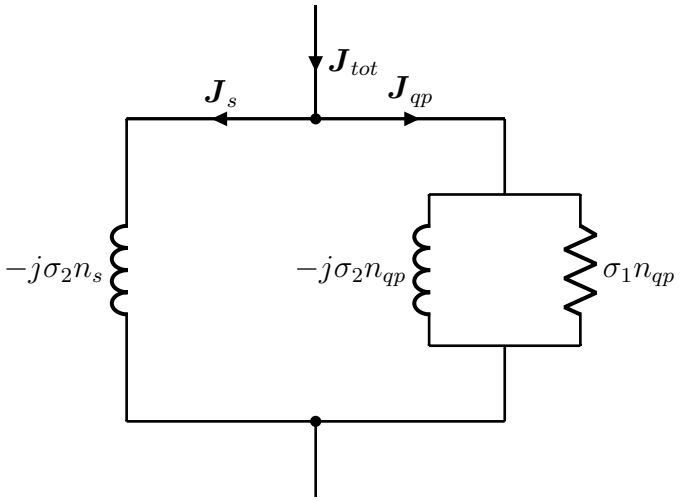

Figure 2.2: A circuit diagram describing the two fluid model for a superconductor.

For the DC case, where the frequency of the signal is 0 Hz, the reactance of the inductor is zero, the inductor will behave as a short circuit which mean the

electron population will flow via the two inductive paths, opposed to the path of non-zero resistance via of the resistor. Thus, the two-fluid model describes the superconducting phenomenon of no DC resistance below T_c.

In the case of AC, at low frequencies and temperatures, the impedance of the inductor is low and the current will flow predominantly through the path of least impedance via the inductor. This translates to the current carried primarily by the non-scattering, superconducting electron density, n_s. As the temperature and frequency increases, there are fewer Cooper pairs available and more quasi-particles, which increases the proportion of the current which travels down the quasi-particle path through the parallel resistor. This equates to more current being carried by the quasi-particle population, n_{qp} and is described by equation 2.7 because σ_s is inversely proportional to frequency ω. Applying the two-fluid model through considerations of Ohm's law, J_{tot} is given by:

$$\boldsymbol{J_{tot}} = \boldsymbol{J_s} + \boldsymbol{J_{qp}} = (\sigma_1 - j\sigma_2)\boldsymbol{E} \tag{2.9}$$

Therefore, the conductivity of a superconductor can be written as:

$$\sigma_{tot} = \frac{n_n e^2 \tau}{m_e(1 + j\omega^2\tau^2)} - j\left(\frac{n_s e^2}{m_e \omega} + \frac{n_n e^2 \tau^2 \omega}{m_e(1 + j\omega^2\tau^2)}\right) \tag{2.10}$$

This is an important outcome of the two-fluid model, because it describes how the real part of the conductivity is purely due to the normal fluid, whereas the imaginary part of the conductivity is a combination of both the normal and superconducting fluids. By setting $\tau = \inf$ in equation 2.10, which is representative of the non-scattering Cooper pairs, the equation is dominated by the second, imaginary term where $\omega^2\tau^2 >> 1$. The result is the same conductivity, σ_s presented in equation 2.7 which can be used to rewrite the penetration depth.

$$\lambda_L = \sqrt{\frac{1}{\mu_0 \omega \sigma_s}} \tag{2.11}$$

Moreover, the London penetration depth varies with n_s (equation 2.5), where n_s also depends on temperature (equation 2.8). The two equations are combined to determine the relationship between temperature and the London penetration depth.

$$\lambda_L(T) = \lambda_L(0)\left[1 - \left(\frac{T}{T_c}\right)^4\right]^{-\frac{1}{2}} \tag{2.12}$$

with $\lambda_L(0)$ as the London penetration depth at 0 K.

A major assumption of the London model is superconducting electrons do not scatter, but this is not the case as a Cooper pair has finite size. The London equations describe observations, yet do not describe the phenomenon of superconductivity and consequently Cooper pairs and complex conductivity. In order to accurately describe the conductivity of superconductors, the conductivity of the superconducting electron density must be accounted for via the introduction of Mattis-Bardeen equations [65].

2.4 Mattis-Bardeen Superconductivity

Bardeen, Cooper and Schrieffer set the foundations for the microscopic theory of superconductors, BCS theory, paving the way for Mattis and Bardeen to quantify complex conductivity [66]. These expressions account for the formation of Cooper pairs and quasi-particles excitation [65]. The Mattis-Bardeen expression for complex conductivity is shown below where σ_1 and σ_2 are in the same meaning as equation 2.2. The normal state conductivity, σ_n, is defined as the conductivity just above T_c.

$$\frac{\sigma_1}{\sigma_n} = \frac{2}{\hbar\omega}\int_{\Delta}^{\infty}[f(E)-f(E+\hbar\omega)]g(E)dE + \frac{1}{\hbar\omega}\int_{\Delta-\hbar\omega}^{\Delta}[1-2f(E+\hbar\omega)]g(E)dE \quad (2.13)$$

$$\frac{\sigma_2}{\sigma_n} = \frac{1}{\hbar\omega}\int_{\Delta-\hbar\omega,-\Delta}^{\Delta}\frac{[1-2f(E+\hbar\omega)](E^2+\Delta^2+\hbar\omega E)}{(\Delta^2-E^2)^{\frac{1}{2}}[(E+\hbar\omega)^2-\Delta^2]^{\frac{1}{2}}} \quad (2.14)$$

where

$$f(E) = \frac{1}{1+exp(E/k_bT)} \quad (2.15)$$

and

$$g(E) = \frac{E^2+\Delta^2+\hbar\omega E}{(E^2-\Delta^2)^{\frac{1}{2}}[(E+\hbar\omega)^2-\Delta^2]^{\frac{1}{2}}} \quad (2.16)$$

Another key term introduced in the Mattis-Bardeen expressions is the binding energy of Cooper pairs, Δ. BCS theory states that Cooper pairs, pairs of electrons, are bound together with an energy characterised by 2Δ, the energy to break apart a Cooper pair. The binding energy of electrons in a Cooper pair changes as a function of temperature with the energy gap at absolute zero, Δ_0, depending on the critical temperature T_c [67].

$$\Delta(T) = \Delta_0 tanh\left(1.74\sqrt{\frac{T_c}{T}-1}\right) \quad (2.17)$$

where

$$2\Delta_0 = 3.5 k_b T_c \tag{2.18}$$

and k_b has its usual meaning of the Boltzmann constant. Figure 2.3 shows the variation of the energy gap Δ as a function of temperature as predicted by BCS theory and well confirmed by experiment.

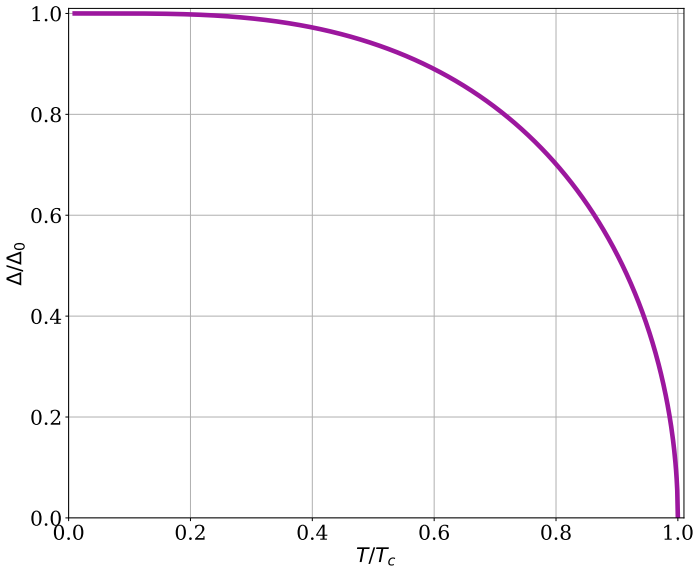

Figure 2.3: Energy gap Δ as a function of temperature T, presented as a ratio of the energy gap at 0 K and the critical temperature.

For the Mattis-Bardeen expressions presented in equations 2.13 and 2.14 it is 2Δ which sets the boundary at which the integral limits switch. As the second integral in equation 2.13 represents pair-breaking, it is only important when photon energies ($E = \hbar\omega$) exceed 2Δ. This distinct boundary (when the x-axis = 1) is visible in figure 2.4, where the ratio σ_1/σ_n is plotted as a function of photon energy divided by 2Δ.

For σ_2 the lower limit of the integral changes from $\Delta - \hbar\omega$ to -Δ for energies above 2Δ. The ratio of σ_2 to σ_n are shown in figure 2.5, as a function of photon energy divided by 2Δ. It is not plotted in figure 2.5, but it should be noted that σ_2 is ~ 400 times greater than σ_1 at low frequencies. With respect to the proposed system shown in figure 1.1, the 2Δ limit is an important property of the material that is exploited to make the device work. For the transmission line to be low

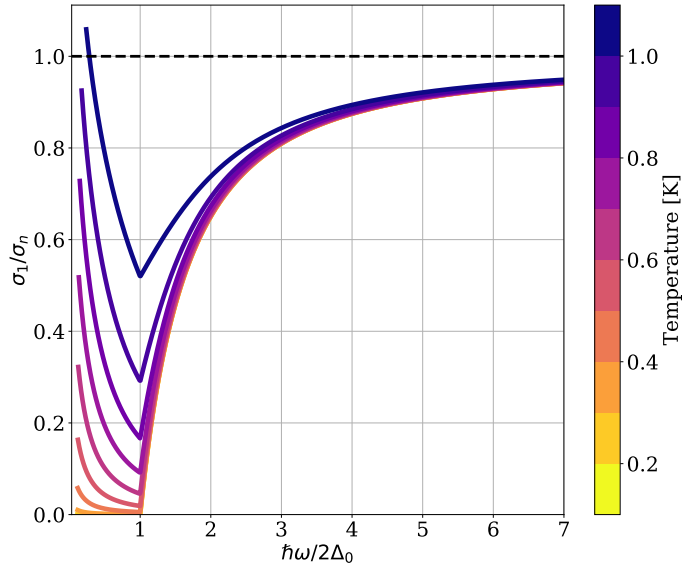

Figure 2.4: The Mattis-Bardeen expression for the real component of conductivity, evaluated as a function of frequency and temperature where σ_1 is evaluated using equation 2.13 for aluminium with a T_c of 1.2 K at 1 GHz.

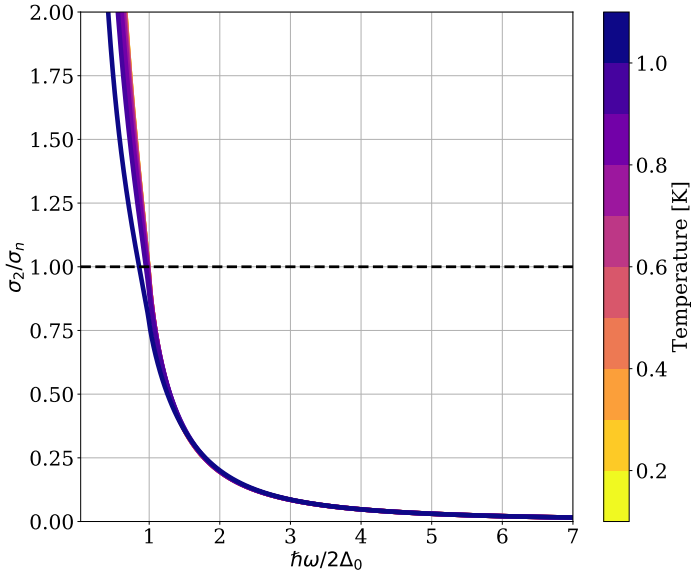

Figure 2.5: The Mattis-Bardeen expression for the imaginary component of conductivity, evaluated as a function of frequency and temperature where σ_2 is evaluated using equation 2.14 for aluminium with a T_c of 1.2 K at 1 GHz.

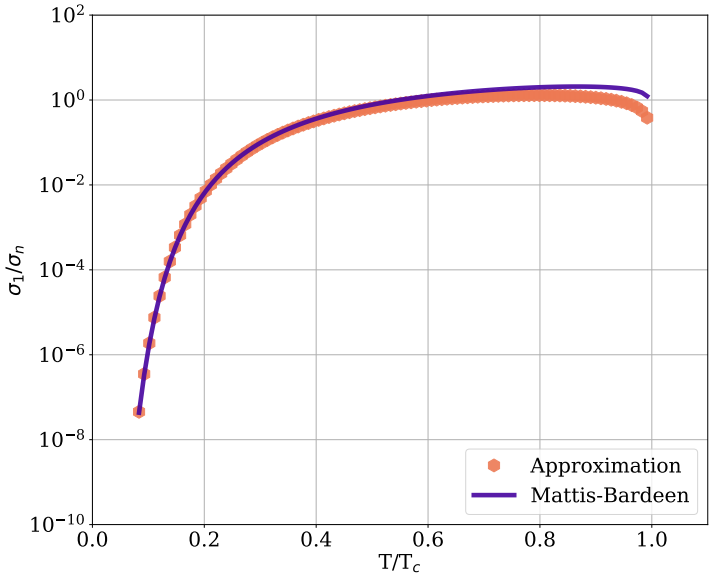

Figure 2.6: The Mattis-Bardeen expressions and approximations, for the conductivity due to quasi-particles, evaluated as a function of temperature for aluminium with a T_c of 1.2 K at 1 GHz.

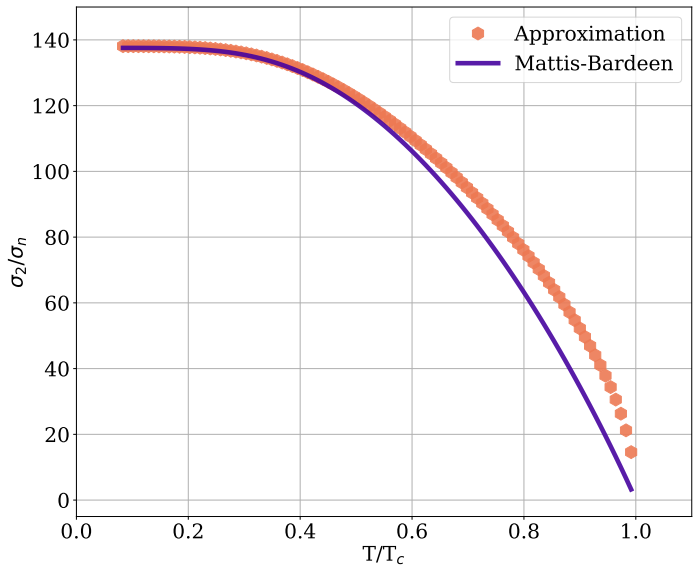

Figure 2.7: The Mattis-Bardeen expressions and approximations, for the conductivity due to Cooper pairs, evaluated as a function of temperature for aluminium with a T_c of 1.2 K at 1 GHz.

loss the energy of the photon must be less than 2Δ. However, for the detection of microwave photons, it is important to break apart Cooper pairs. The consequences of quasi-particle generation will become clearer later.

If both k_bT and $\hbar\omega$ are much less than 2Δ, a useful property for transmission lines, the Mattis-Bardeen expressions can be simplified [68].

$$\frac{\sigma_1}{\sigma_n} = \frac{4\Delta}{\hbar\omega} exp(-\Delta/k_bT) sinh\Big(\frac{\hbar\omega}{2k_bT}\Big) K_0\Big(\frac{\hbar\omega}{2k_bT}\Big) \tag{2.19}$$

$$\frac{\sigma_2}{\sigma_n} = \frac{\pi\Delta}{\hbar\omega}\Big[1 - exp(-\Delta/k_bT) exp\Big(\frac{-\hbar\omega}{2k_bT}\Big) I_0\Big(\frac{\hbar\omega}{2k_bT}\Big)\Big] \tag{2.20}$$

where I_0 and K_0 are the modified Bessel functions of the first and second kind. A comparison of the Mattis-Bardeen approximation to the full expression is shown in figures 2.6 and 2.7 for both σ_1 and σ_2. The approximation agrees well up to ~ 0.4 T_c.

2.5 Internal Inductance of a Superconductor

The internal inductance of a superconducting strip is the sum of its kinetic inductance, L_k, and magnetic inductance, L_m; where kinetic inductance is the manifestation of the delay in electrons changing direction in an alternating electric field due to their inertia. To calculate the kinetic inductance of a superconducting strip, the kinetic energy density of the electrons contributing to a current density J_s must be considered.

$$KE = \frac{1}{2} n_s m_e v_s^2 \tag{2.21}$$

$$KE = \frac{1}{2}\frac{m_e}{n_s e^2} J_s^2 = \frac{1}{2}\mu_0\lambda_L^2 J_s^2 \tag{2.22}$$

The kinetic energy in equation 2.22 must be equated to the total energy stored in an inductor,$(\frac{1}{2}L_kI^2)$, to determine the kinetic inductance.

$$U_k = \frac{1}{2}L_kI^2 = \frac{1}{2}\mu_0\lambda_L^2 \int_s J_s^2 ds \tag{2.23}$$

with U_k representing the total kinetic inductance per unit length and I as the total current. The current density is limited to the surface of the superconductor, with a thickness defined by the penetration depth λ_L, therefore once the surface integral is evaluated, the kinetic inductance can be calculated.

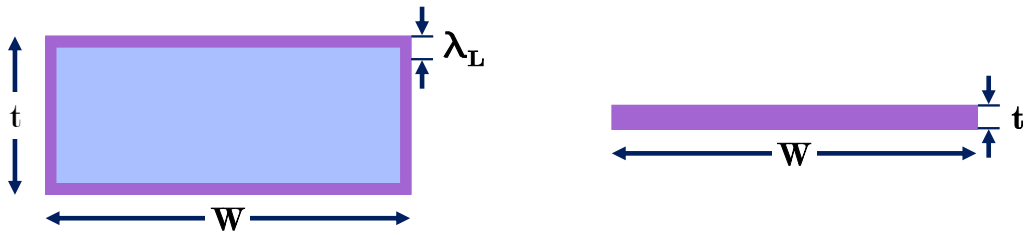

(a) (b)

Figure 2.8: The current density in a (a) thick and (b) thin superconducting film, where the current is restricted to a depth of λ_L. In a thin film, t > λ_L so the current flows throughout the full film volume.

Consider two superconducting films of thickness t: a thick superconducting film where $\lambda_L \ll t \ll W$ and a thin superconducting film where $t \ll \lambda_L \ll W$. The two scenarios are depicted in figure 2.8, with the thick film in (a) and the thin film in (b). In the case of the thick film, the effective cross-sectional area is $2W\lambda_L$ whilst neglecting the small current density of $2t\lambda_L$ which flows around the edges. Thus, $J_s = I/2W\lambda_L$ and the kinetic inductance of the thick film, measured in units of H/m, is as follows:

$$\frac{1}{2}L_k I^2 = \frac{\mu_0 \lambda_L^2 I^2}{8W^2\lambda_L^2} 2W\lambda_L \tag{2.24}$$

$$L_k = \frac{\mu_0 \lambda_L}{2W} \tag{2.25}$$

For a thin film, the effective cross-sectional area is Wt, therefore the kinetic inductance is given by

$$\frac{1}{2}L_k I^2 = \frac{\mu_0 \lambda_L^2 I^2}{2W^2t^2} Wt \tag{2.26}$$

$$L_k = \frac{\mu_0 \lambda_L}{Wt} \tag{2.27}$$

Typically KIDs are fabricated with a film thickness that lies in between the above two cases, therefore the current density across the entire cross-sectional area of the film must be integrated over. The full derivation is presented in Doyle [69]. This results in

$$L_k = \frac{\mu_0 \lambda_L}{4W}\left[coth\left(\frac{t}{2\lambda_L}\right) + csch^2\left(\frac{t}{2\lambda_L}\right)\right] \tag{2.28}$$

and

$$L_m = \frac{\mu_0 \lambda_L}{4W}\left[coth\left(\frac{t}{2\lambda_L}\right) - csch^2\left(\frac{t}{2\lambda_L}\right)\right] \tag{2.29}$$

where L_m is the magnetic inductance, which is the inductance due to the energy stored in the magnetic field within the varying penetration depth.

Both equations 2.28 and 2.29 are in units of H/m. To calculate the total internal inductance, the two inductances are added together and by multiplying by the width of the superconducting strip, the resulting units are in H/square.

$$L_{int} = L_k + L_m = \frac{\mu_0 \lambda_L}{2} coth\Big(\frac{t}{2\lambda_L}\Big) \tag{2.30}$$

In figure 2.9, the kinetic inductance is shown as a function of film thickness and temperature for a fixed λ_L of 168 nm, calculated using equation 2.11, with λ calculated using equation 2.12. Here, the kinetic inductance only starts to noticeably change once T > 0.5 T_c, and sharply increases as T approaches T_c. However, as the Mattis Bardeen approximation has been used to determine λ_L, these results are only valid to $\sim$ 0.4 T_c. As a ratio of the total internal inductance, determined by equation 2.30, the magnetic (equation 2.29) and kinetic inductance (equation 2.28) is evaluated as a function of film thickness for a λ_L of 168 nm, and is shown in figure 2.10. As the film thickness increases, the kinetic inductance accounts for a decreasing fraction of the total internal inductance and by $\sim$ 1200 nm, which is 7λ, the kinetic and magnetic inductance are equal.

2.6 Surface impedance of a Superconducting Film

The surface impedance of a superconducting film, Z_s consists of two components: a real element, which is resistive, and an imaginary element which contains the magnetic and kinetic inductance, L_k and L_m.

$$Z_s = R_s + jX_s = R_s + j\omega L_{tot} \tag{2.31}$$

where R_s is the surface resistance, X_s is the surface reactance and L_{tot} is defined as the total internal inductance in equation 2.30. The surface resistance of a superconducting strip can be determined by following the example in Doyle [69].

$$R_s I^2 = Re\left\{\oint \frac{\boldsymbol{J}^2}{\sigma_1 - j\sigma_2} d\boldsymbol{s}\right\} = \frac{\sigma_1}{\sigma_1^2 + \sigma_2^2} \oint \boldsymbol{J}^2 d\boldsymbol{s} \tag{2.32}$$

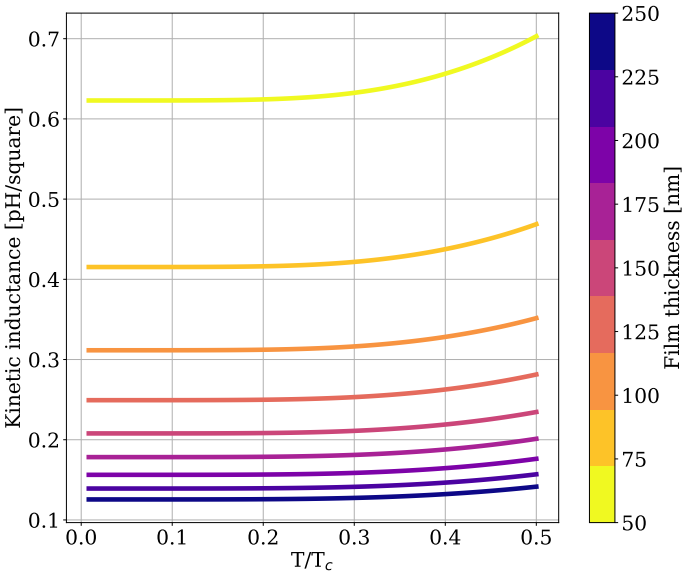

Figure 2.9: For a fixed λ_L of 168 nm, calculating using equation 2.11, the kinetic inductance as a function of the ratio T/T_c for different superconducting film thicknesses. Equation 2.12 is used to calculate λ_L as a function of temperature. Here, σ_n is 3.7x10^7 Ω/m for aluminium and the Mattis Bardeen approximations have been utilised.

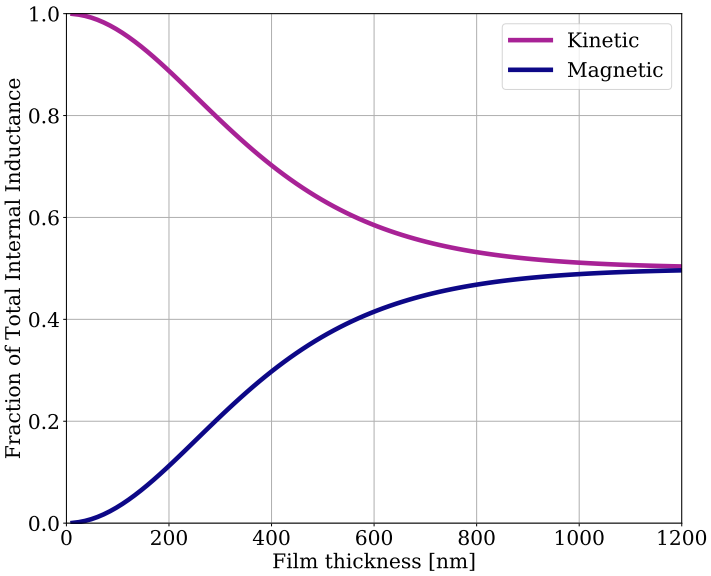

Figure 2.10: For a λ_L of 168 nm, calculating using equation 2.11, the ratio of the kinetic inductance and magnetic inductance to total inductance is presented as a function of film thickness. σ_n is 3.7x10^7 Ω/m for aluminium and the Mattis Bardeen approximations have been utilised.

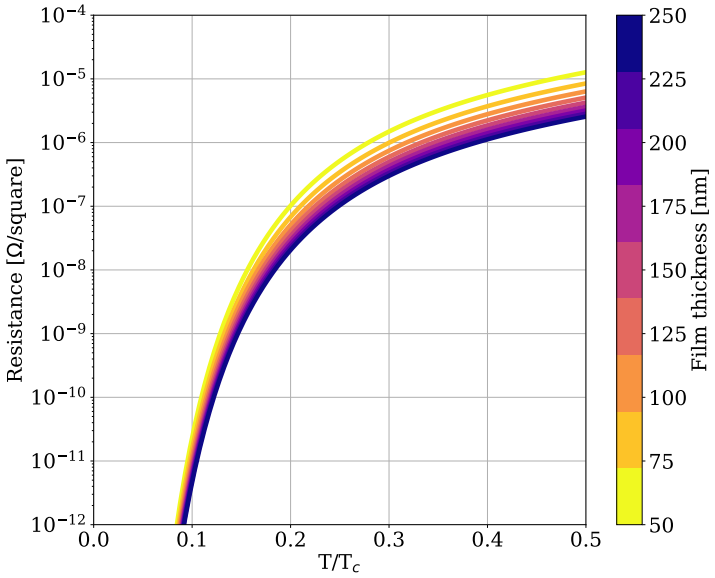

Figure 2.11: Resistance versus T/T_c, as determined by equation 2.34, as a function of film thickness at a frequency of 1 GHz. σ_n is 3.7x10^7 Ω/m for aluminium and the Mattis Bardeen approximations have been utilised.

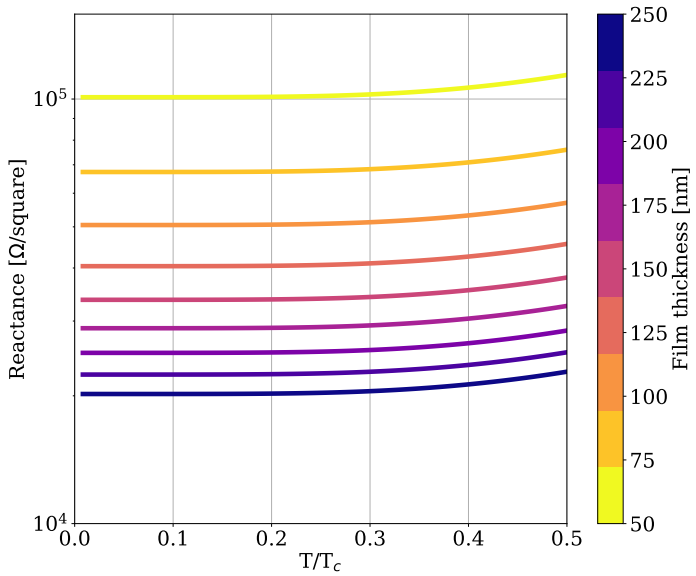

Figure 2.12: Reactance versus T/T_c, calculated from the imaginary component of equation 2.36, as a function of film thickness at a frequency of 1 GHz. As before, σ_n is 3.7x10^7 Ω/m for aluminium and the Mattis Bardeen approximations have been utilised.

Using equation 2.23, the surface integral can be rewritten in terms of the kinetic inductance to give

$$R_s = \frac{\sigma_1}{\sigma_1^2 + \sigma_2^2} \frac{L_k}{\mu_0 \lambda_L^2} \tag{2.33}$$

which can be simplified further using the penetration depth defined in equation 2.11.

$$R_s = \omega L_k \frac{\sigma_1 \sigma_2}{\sigma_1^2 + \sigma_2^2} \tag{2.34}$$

In the limit of $\sigma_1 << \sigma_2$, R becomes:

$$R_s = \omega L_k \frac{\sigma_1}{\sigma_2} \tag{2.35}$$

The resistance as a function of temperature and film thickness is shown in figure 2.11. In general, the resistance increases as a function of temperature, but decreases as the film thickness increases. For a microstrip transmission line, the lower loss a film is the better, thus it is beneficial to have a thick film and operate at a lower temperature. By writing both the resistive and reactive components of the impedance in terms of conductivity, it is possible to determine a final expression for the strip impedance, Z_s,

$$Z_s = R_s + jX_s = L_k \omega \frac{\sigma_1 \sigma_2}{\sigma_1^2 + \sigma_2^2} + j\sqrt{\frac{\mu_0 \omega}{4\sigma_2}} \coth\left(\frac{t}{2}\sqrt{\sigma_2 \omega \mu_0}\right) \tag{2.36}$$

In figure 2.12 the reactance, calculated using equation 2.36, is shown as a function of temperature and film thickness. There are two ways to increase the reactance, through an increase in temperature or a reduction in film thickness. Although the reactance appears to be constant at lower temperatures, it is changing, meaning even a small increase in temperature will change the reactance of a superconducting thin film.

2.7 Quasi-particle Dynamics

As described by the two-fluid model of conductivity and the Mattis-Bardeen integrals, below T_c, there are two populations of electrons - Cooper pairs and quasi-particles. Moreover, the detectors described in this chapter respond to changes in quasi-particle number. In order to understand the dynamics of quasi-particles, it is necessary to explore their response to changes in temperature and incident radiation.

2.7.1 Thermal Excitations

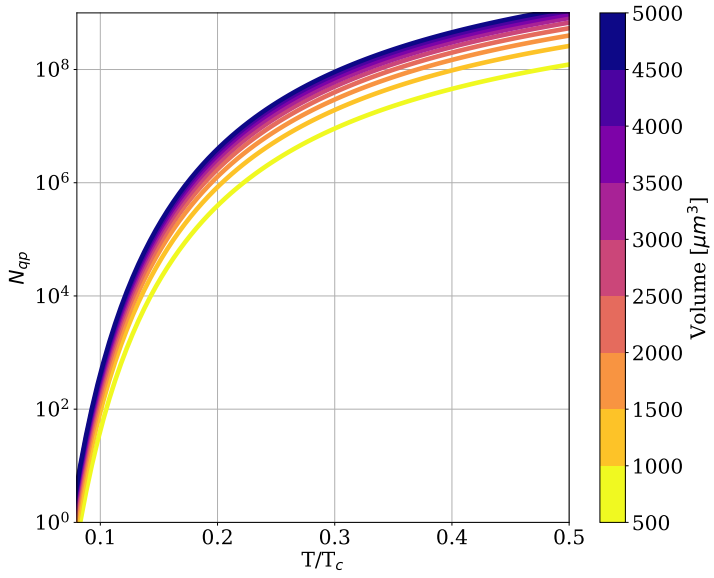

Figure 2.13: The effective temperature of a superconducting volume from the number of quasi-particles created for different volumes

The quasi-particle density is the statistical mean number of quasi-particles at a given temperature. At T > 0 K, vibrations from the lattice break apart Cooper pairs, causing the quasi-particle density to continuously fluctuate about the mean value. For recombination, a quasi-particle must find another quasi-particle with the opposite spin and equal (but opposite) momenta [62]. As the density of quasi-particles decreases, the potential for recombination within a given timescale decreases. This timescale is characterised by the quasi-particle lifetime, τ_{qp}. To calculate the number of thermally generated quasi-particles we need to determine τ_{qp} as described by Kaplan theory [70].

$$\frac{1}{\tau_{qp}} = \frac{\tau_0}{\sqrt{\pi}} \left(\frac{k_b T_c}{2\Delta} \right)^{5/2} \sqrt{\frac{T_c}{T}} e^{-\Delta/k_b T} \tag{2.37}$$

where τ_0 is material dependant. At T = 0 K, all available electrons will be paired up in Cooper pairs, such that $n = n_s$. However, as Cooper pairs are broken apart as the temperature increases, the quasi-particle population will fluctuate about a mean value, given by De Visser [71].

$$n_{qp} = 4N_0 \int_0^\infty N_s(E) f(E) dE \approx 2N_0 \sqrt{2\pi k_b T \Delta} e^{-\Delta/k_b T} \tag{2.38}$$

where $N_s(E) = Re\left\{E/\sqrt{E^2+\Delta^2}\right\}$ is the normalised quasi-particle density of states. The approximation is only valid for a thermal quasi-particle distribution where $k_bT \ll \Delta$. As the number of quasi-particles thermally generated per unit volume N_{qp} is equal to $n_{qp}V_T$, then

$$N_{qp} = 2N_0\sqrt{2\pi k_bT\Delta}e^{-\Delta/k_bT}V_T \tag{2.39}$$

where N_0 is material dependant and is 1.7x10^{10} μm^{-3}eV for aluminium. [42]. N_{qp} as a function of temperature and volume, V_T is shown in figure 2.13. Here, the number of quasi-particles generated decreases rapidly as the temperature decreases. When quasi-particles are generated at low temperatures, there is a greater change in effective temperature. By calculating the product of equations 2.37 and 2.39, it is possible to remove the dependency on temperature.

$$N_{qp}\tau_{qp} = N_0\tau_0\frac{k_b^3T_c^3}{2\Delta^2}V_T \tag{2.40}$$

2.7.2 Photon Absorption

The basic principle behind the operation of KIDs is absorbed photons, with an energy above 2Δ break apart Cooper pairs causing an increase in the number of quasi-particles in the detector. The 2Δ requirement sets a minimum detectable frequency for incident radiation - this is shown in figure 2.14. The minimum frequency of aluminium, with a T_c of 1.2 K, is 89 GHz whereas for niobium with a T_c of 9.3 K, this is around 688 GHz.

During photon absorption, the number of quasi-particles rises until an equilibrium is reached between the number of quasi-particles being created to those recombining. It is possible to estimate the loaded equilibrium number of quasi-particles generated under a continuous flux of photons of energy $E > 2\Delta$, using:

$$N_{xs} = \frac{\eta P_{opt}\tau_{qp}}{\Delta} \tag{2.41}$$

where N_{xs} is equal to the excess number of quasi-particles in the system, P_{opt} is the optical power and η is the quasi-particle creation efficiency factor, with an accepted value of 0.57 [56].

To fully model the response of a KID to incoming signals, the relationship between the geometry of a KID and key characteristics such as resonant frequency must be considered.

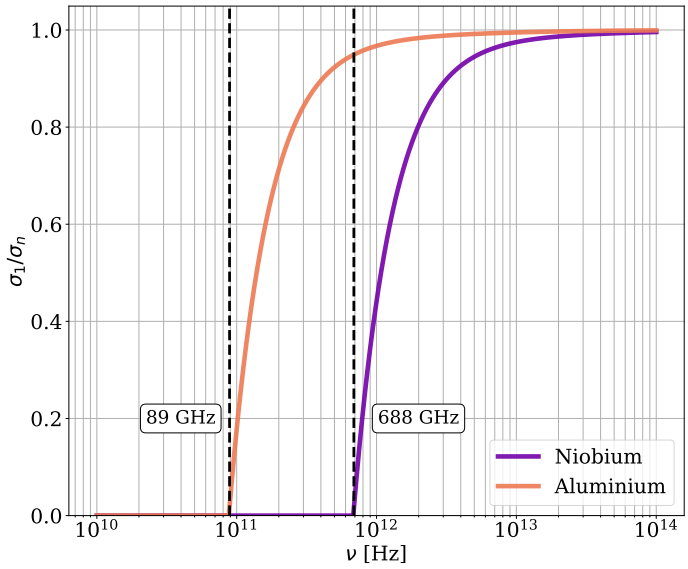

Figure 2.14: The ratio σ_1/σ_n as a function of frequency for aluminium with a typical T_c of 1.2 K and niobium where T_c is equal to 9.3 K. This converts to a minimum frequency of 89 and 688 GHz.

2.8 Geometry of a KID

Kinetic inductance detectors are superconducting microwave resonators consisting on inductive, capacitive and resistive elements. The resistance is due to the quasi-particles generated in the inductor of the KID. For a LEKID, the type of KID presented in this thesis, the inductor and capacitor are spatially separated [69]. An equivalent circuit diagram of the LEKID, a series RLC resonator, is shown in figure 2.15.

The average energy stored in the inductor and capacitor, W_m and W_e, are defined as [72]

$$W_m = \frac{1}{4} |I|^2 L \tag{2.42}$$

and

$$W_e = \frac{1}{4} |V_c|^2 C = \frac{1}{4} |I|^2 \frac{1}{\omega^2 C} \tag{2.43}$$

At resonance, $W_m = W_e$, the resonant frequency ω_0 of the system is given by [72]

$$\omega_0 = \frac{1}{\sqrt{(L_g + L_{int})C}} \tag{2.44}$$

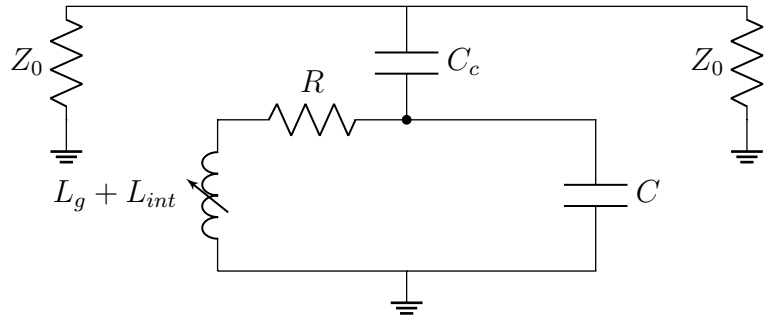

Figure 2.15: The circuit diagram for a capacitively coupled LEKID, including a coupling capacitor C_c, geometric capacitor C, geometric inductance L_g, and resistor R.

where, as a reminder, L_g is the geometric inductance, L_{int} is the total internal inductance where $L_{int} = L_k + L_m$ and C is the capacitance.

2.9 Quality Factors

A key parameter for microwave resonators is the quality factor, Q. In general, the quality factor is the ratio of the energy stored, E_{stored}, to the energy lost per cycle, P_{loss}.

$$Q = \frac{\omega E_{stored}}{P_{loss}} \tag{2.45}$$

But for a KID, this is generally characterised by three different loss mechanisms: (i) through the resistive properties of the material and detector geometry, (ii) by coupling the detector to readout feedline and (iii) via the detector radiating like an antenna. However, due to lumped-element nature of the components in a LEKID, meaning the components are much smaller than the wavelength, there is a negligibly small dipole moment in the detector. Thus, the power radiating from a LEKID can be neglected as a loss mechanism.

At resonance, the total energy in the capacitor is equal to that stored within the inductor. Therefore $E_{stored} = W_e + W_m = 2W_e$ and can be combined with $P_{loss} = |I|\, R/2 = |V_c|\, /2R$ results in

$$Q_i = \frac{\omega L}{R} = \omega C_{res} R \tag{2.46}$$

where Q_i, the intrinsic quality factor, is dependant on properties of each resonator component and losses in the material. [69] A LEKID capacitively coupled to a

feedline is shown in figure 2.15, which has an associated loss for the system and therefore can also be characterised by a quality factor. Q_c. Here, Q_c is the energy that radiates out of the KID, via the coupling capacitor, to the transmission line.

$$P_{loss} = \frac{1}{2} |I_{loss}|^2 R = \frac{1}{4} |V_c|^2 \omega_0^2 Z_0 \tag{2.47}$$

where $I_{loss} = |V_c| Z_{Cc}$, $Z_{Cc} = 1/j\omega C_c$ and $R = Z_0/2$ thanks to the two feedline ports shown in figure 2.15. At resonance, $E_s = 2W_e$ and therefore Q_c is given by [69]

$$Q_c = \frac{2C}{\omega_r Z_0 C_c^2} \tag{2.48}$$

where Z_0 is the characteristic impedance of the transmission line, and is described by

$$Z_0 = \frac{1}{\sqrt{L/C}} \tag{2.49}$$

Generally C and Z_0 are treated as constant, therefore it is possible to tune Q_c by just changing C_c. Overall, the total quality factor, Q_{tot}, to describe the resonator system can be determined using the following equation:

$$\frac{1}{Q_{tot}} = \frac{1}{Q_c} + \frac{1}{Q_i} \tag{2.50}$$

Recall, the power radiation from the device has been neglected because it is negligible as the KID components are lumped elements.

2.10 Impedance of the Resonator

For a lossless capacitor and inductor, with resistance as the only source of loss in the system, the impedance due to the path down the inductive side of the circuit, Z_L is given by [72]

$$Z_L = j\omega L + R \tag{2.51}$$

and the capacitive side of the circuit, Z_C, is equal to

$$Z_C = \frac{1}{j\omega R} \tag{2.52}$$

where ω is the frequency of the probing microwave signal. The total impedance of the resonator, Z_{res}, is given by the algebraic sum of the inverses of the two impedances, Z_C and Z_L.

$$\frac{1}{Z_{res}} = j\omega C_{res} + \frac{1}{j\omega L + R} = j\omega C_{res} + \frac{R - j\omega L}{R^2 + \omega^2 L^2} \tag{2.53}$$

It is possible to simplify this equation further because $\omega^2 L^2 \ll R^2$, therefore

$$\frac{1}{Z_{res}} = j\omega C_{res} + \frac{R}{\omega^2 L^2} + \frac{1}{j\omega L} \tag{2.54}$$

When measuring a LEKID, the resonator is probed with a signal close to its resonant frequency, where $\omega = \omega_0 + \Delta\omega$ and $\Delta\omega \ll \omega_0$. Thus, it is possible to simplify equation 2.54 through the Taylor expansion $1/(1+x) \simeq 1 - x$ if $x \ll 1$. Here, $x = \Delta\omega/\omega_0$ and therefore equation 2.54 becomes

$$\frac{1}{Z_{res}} = j\Delta\omega C_{res} + \frac{R}{(\omega_0 + \Delta\omega)^2 L^2} \tag{2.55}$$

As previously defined, where the inductance is $L = L_g + L_{int}$ in $\omega_0 = 1/\sqrt{LC}$ and since $\Delta\omega \simeq \omega_0$, the resonator impedance can be simplified further still, such that

$$Z_{res} = \frac{\omega_0^2 L^2}{2j\Delta\omega L + R} \tag{2.56}$$

Finally, to calculate the impedance of the resonator, the impedance of the coupling capacitor must also be taken into account, such that $Z_{tot} = Z_{Cc} + Z_{res}$.

$$Z_{tot} = \frac{\omega_0^2 L^2}{2j\Delta\omega L + R} - \frac{-j}{\omega C_c} \tag{2.57}$$

2.11 Transmission of Resonator

It is common practice within microwave engineering to characterise the output of a device using scattering parameters, which are simply the ratio of voltages measured on one port relative to another. For example S_{21}, shown in figure 2.16, is the ratio of the voltage at port 2 to port 1 [72].

Typically S_{21} is the main parameter measured, using a Vector Network Analyser (VNA) as this characterised the transmission of the input signal. However, S_{11} is also a useful parameter as it characterises the reflection of the input signal. Further details about measuring a LEKID are presented in the next chapter. It is possible to calculate S_{21} by considering an applied voltage to the input port of the main network [72].

$$S_{21}(\omega) = \frac{2}{2 + Z_0/Z_{in}} \tag{2.58}$$

with the impedance of the feedline, Z_0, typically set to 50 Ω. The expression for Z_0/Z_{in} given by [58] is

$$\frac{Z_0}{Z_{in}} \approx \frac{2Q_i}{Q_c} \frac{1}{1 + 2Q_i x_r} \tag{2.59}$$

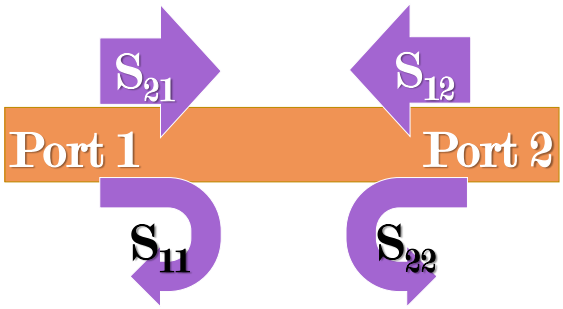

Figure 2.16: Definition of scattering parameters. In the case of measuring a cryogenic detector, S_{21} is of interest because it characterises the transmission of a two port system alongside the reflection parameter S_{11}.

where x_r is the fractional frequency shift of the resonator and is given by:

$$x_r = (\omega - \omega_{res})/\omega_{res} \tag{2.60}$$

and ω_{res} is the resonant frequency of the resonator coupled to the feedline. By combining equations 2.58,2.59 and 2.50, a final equation for $S_{21}(\omega)$ can be determined and is given by

$$S_{21} = 1 - \frac{Q_{tot}}{Q_c}\frac{1}{1 + 2jQx_r} \tag{2.61}$$

The result of equation 2.61 is a Lorentzian lineshape centred around ω_{res} with a bandwidth (defined by the full width half maxima, FWHM) of ω_{res}/Q_{tot}. An example of a simulated resonance is shown in figure 2.17, where the dip depth of the resonator is given by the ratio of Q_{tot}/Q_c.

Thus, by measuring S_{21} of a resonator, it is possible to extract the quality factors to help quantify one aspect of resonator performance. A resonator with high quality factors will have a smaller (and therefore narrower) full width half maxima and a large resonator dip depth, whereas low-Q resonators are broader. Moreover, resonators with high quality factors are beneficial for creating large arrays of detectors because they enable more resonators to fit into a fixed detector readout bandwidth without overlap.

2.12 Summary

Fundamentally, a LEKID is a superconducting resonating detector where, upon absorption of a photon, the modified surface impedance of the film results in change

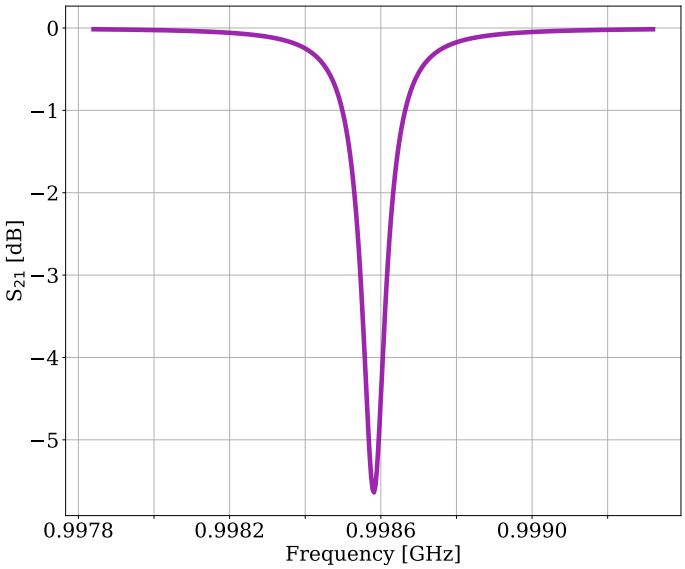

Figure 2.17: The S_{21} transmission of a resonator described by equation 2.61. This is a Lorentzian lineshape centred around ω_{res} with a bandwidth (defined by the FWHM) of ω_{res}/Q_{tot}. Moreover, the the dip depth of the resonator is given by the ratio of Q_{tot}/Q_c.

in resonant frequency. To understand this process, this chapter has utilised BCS theory, the two-fluid model and Mattis-Bardeen integral.

Cooper pairs, which consist of two bound electrons, are responsible for properties observed in superconductors. Breaking apart these Cooper pairs into quasi-particles, with a photon of energy greater than the 2Δ, increases the kinetic inductance of the superconducting film. If the film is patterned with a resistor-inductor-capacitor resonating circuit, at a resonant frequency of $\omega_0 = 1/\sqrt{LC}$, then this change in kinetic inductance causes the resonant frequency to decrease.

With a better understanding of resonator theory and how the geometry of a LEKID determines its resonant theory, it is now possible to explain how losses in the system are characterised by the quality factor. Therefore, at this point in the thesis, it is possible to model a kinetic inductance detector and its response to an optical load.

3

Response of a LEKID

After an introduction to the key principles of superconductivity and microwave resonator theory which describe the principle of detection in LEKIDs, it is now possible to fully model a kinetic inductance detector. In this chapter, a LEKID will be modelled in the commercial electromagnetic simulation software, Sonnet, and the response of the detector to optical power will be calculated. The resonator simulated in this chapter was designed by P. S. Barry. Moreover, sources of noise in a KID are presented here.

3.1 Modelling a KID

To simulate a LEKID detector and its resonant frequency, once the geometry is known, the detector is drawn into the commercial electromagnetic simulation software, Sonnet [1]. Here, the thickness of layers and key properties, such as kinetic

[1]Sonnet Software provides commercial solutions for high-frequency radio frequency and microwave electromagnetic analysis which solves Maxwell's equations in 2-dimensional space [73].

inductance and the dielectric constant, can be defined.

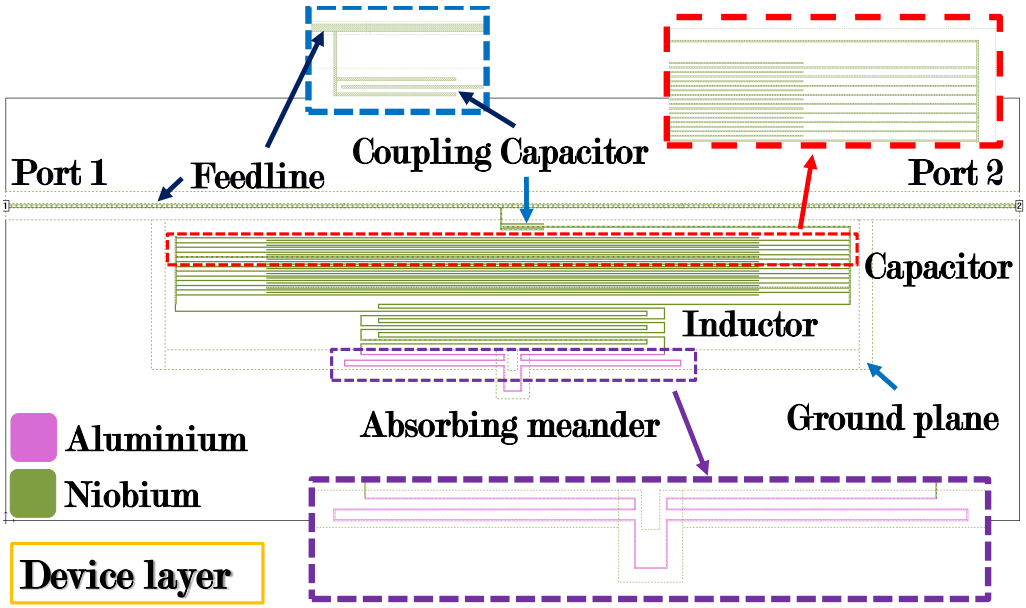

Figure 3.1: Sonnet simulation layout of an example detector, with the different detector elements labelled. Here, the niobium elements are in green and the aluminium elements are pink. This is the device layer which sits on a Silicon substrate.

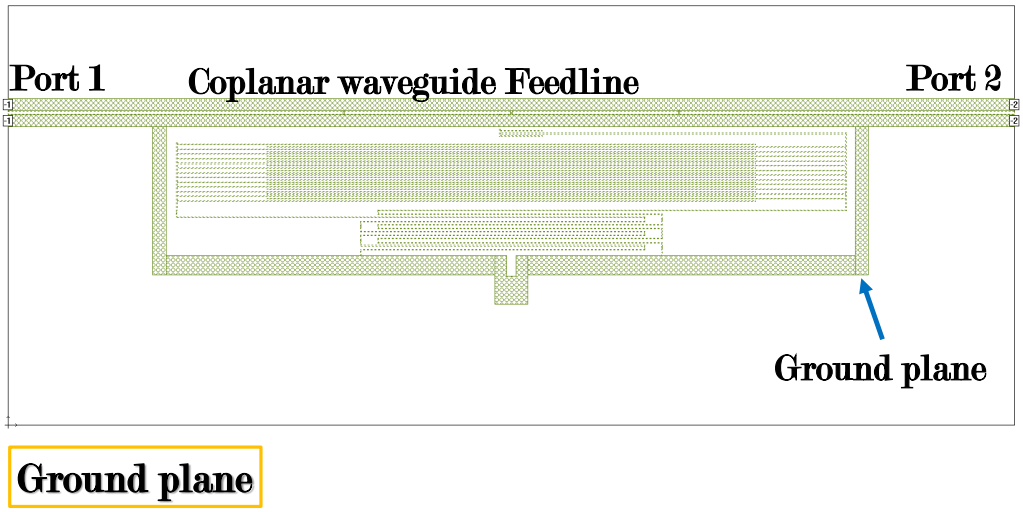

Figure 3.2: Sonnet simulation layout of example detector, with the different detector elements labelled. Here, the niobium elements are in green and the aluminium elements are pink. This is the groundplane layer, which is separated by a dielectric layer above the device layer

An example detector is shown and labelled in figures 3.1 and 3.2, where figure

3.1 details the device layer, sitting on the silicon substrate, and figure 3.2 shows the groundplane layer. These two layers sandwich a layer of dielectric. In both figures, the green regions represent niobium and pink represents aluminium. To run the simulation, the following device properties are needed and are defined in 3.1

Parameter	**Value**
Aluminium L_k	0.2 pH/□
Aluminium thickness	50 nm
Niobium L_k	0.1 pH/□
Niobium thickness	250 nm
Dielectric thickness	0.5 μm
Line width	4 μm
Relative dielectric constant for air	1 [dimensionless]
Silicon thickness	500 μm
Relative dielectric constant for silicon	11.6 [dimensionless]
Absorbing meander volume (Al)	1214 μm^3
Total meander volume	18984 μm^3
Capacitive finger length	3450 μm
Number of capacitive fingers	35
Coupling capacitor length	250 μm

Table 3.1: The known material and geometric parameters for the LEKID resonator shown in figures 3.1 and 3.2

The first step is to determine the fixed, geometric inductance of the resonator. Although the inductive meander is composed of a aluminium and niobium component, the kinetic inductance of the niobium can be treated as a constant, and therefore can be combined into the geometric inductance calculation. Thus, two sonnet simula-

tions are created where the kinetic inductance of absorbing meander, the aluminium inductor, is either zero or a fixed value, L_k. The varying kinetic inductance method to determine the geometric inductance of a LEKID is described by Doyle, and results in the following equation [69].

$$L_g = \frac{L_k}{\left(\frac{\omega_0}{\omega_1}\right)^2 - 1} \tag{3.1}$$

where ω_0 is the resonant frequency of the lossless resonator, and ω_1 is the resonant frequency of the resonator with kinetic inductance added to the meander. The resulting transmission of the resonators, S_{21}, is shown in figure 3.3.

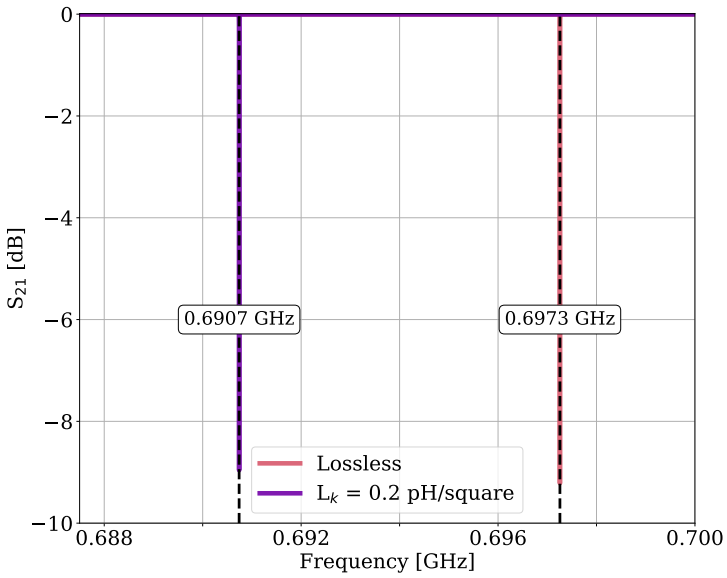

Figure 3.3: S_{21} as a function of microwave probe frequency for the resonator, shown in figures 3.1 and 3.2, when L_k = 0 and 0.2 pH per square within the aluminium meander.

Applying equation 3.1 to the resonant frequencies shown in figure 3.3, results in a geometric inductance of 10.41 pH/□. To determine the number of squares in a meander, the length must be divided by its width, which translates to 1517.5 squares of aluminium. Thus, L_g for the aluminium absorbing meander is 15.80 nH. Substituting L_g and ω_0 into equation 2.44 yields a capacitance value of is 3.30 pF.

3.1.1 Temperature Response

The next part of the model is analytical and is created using Python and a number of built in packages [74, 75, 76]. Further parameters are required for the model, including the critical temperature of the superconductor and the quasi-particle lifetime. These are detailed in table 3.2.

Parameter	**Value**
Aluminium Critical temperature, T_c	1.2 K
Total Geometric inductance, L_g	15.8 nH
Length of aluminium meander, L_l	6.07 cm
Aluminium quasi-particle lifetime, τ_0	80 ns
Aluminium quasi-particle density, N_0	1.7x10^{10} μm^{-3} eV
Aluminium normal state conductivity, σ_n	3.7x10^{7} Ωm^{-1}
Resonant frequency, f_0	0.6973 GHz

Table 3.2: Further known and calculated parameters for the LEKID resonator simulated in figure 3.3.

The first goal of the model is to determine how the resonant frequency will change as a function of temperature.

1. Calculate σ_2 from the Mattis Bardeen integrals in equation 2.14 as a function of temperature at the resonant frequency. Recall, if working at low temperatures and below the 2Δ frequency limit, the Mattis Bardeen approximations are suitable.

2. Calculate the London penetration depth from equation 2.5 and kinetic inductance from equation 2.23

3. Use equation 2.44 to calculate the new resonant frequency as a function of temperature

The next steps are to calculate the conductivity and value of resistance, at the new resonant frequencies and determine the internal quality factor, Q_i.

4. Calculate both components of complex conductivity for the new resonant frequencies using equations 2.14 and 2.13.

5. Use the conductivity, kinetic and geometric inductance and new resonant frequencies to calculate the resistance given by equation 2.46

At this stage, with the internal quality factor and the total quality factor extracted from the sonnet simulation, the coupling Q factor and value of coupling capacitance C_c.

6. Rearrange equation 2.50 to calculate Q_c

7. Calculate the characteristic impedance Z_0 using equation 2.49

8. Rearrange equation 2.48 to determine C_c

It is possible to calculate the total quality factor, as a function of temperature, for the new resonant frequencies and, finally, the scattering parameter S_{21} as a function of temperature.

9. Use equation 2.48 to calculate Q_c as a function of new resonant frequency

10. Calculate the new total quality factor Q as a function of new resonant frequency

11. Use equation 2.61 to calculate S_{21} as a function of temperature.

The transmission of the resonator, S_{21}, as a function of temperature is shown in figure 3.4. As the temperature of the resonator increases, the total Q factor decreases which means the resonance curve gets wider and shallower. The resonant frequency of the KID decreases as the temperature increases and, therefore, the kinetic inductance increases because ω_0 is inversely proportional to kinetic inductance.

To measure the relative change in resonant frequency as a function of temperature, it is common to calculate the fractional frequency shift of the resonator using equation 2.60. The fractional frequency shift of the resonator in 3.4 is shown in figure 3.5, and is calculated with respect to the 80 mK resonant frequency value. As

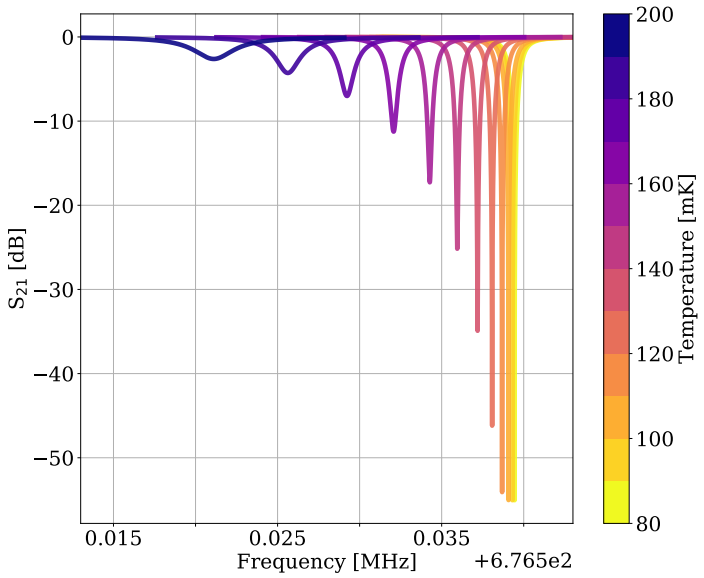

Figure 3.4: The transmission parameter, S_{21}, as a function of temperature for the detector shown in figure 3.3, as described by equation 2.61.

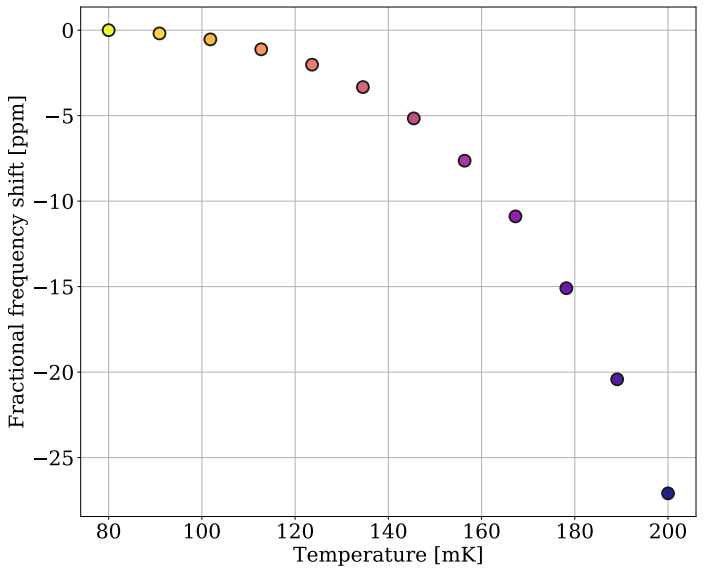

Figure 3.5: The fractional frequency response of the resonator with respect to the lowest temperature point simulated, 80 mK.

the fractional response is typically of magnitude $\sim 10^{-6}$, it is expressed in parts per million, *ppm*. With the temperature response of the detector calculated, the next goal with the model is to determine the detector response to an optical load.

3.1.2 Optical Load

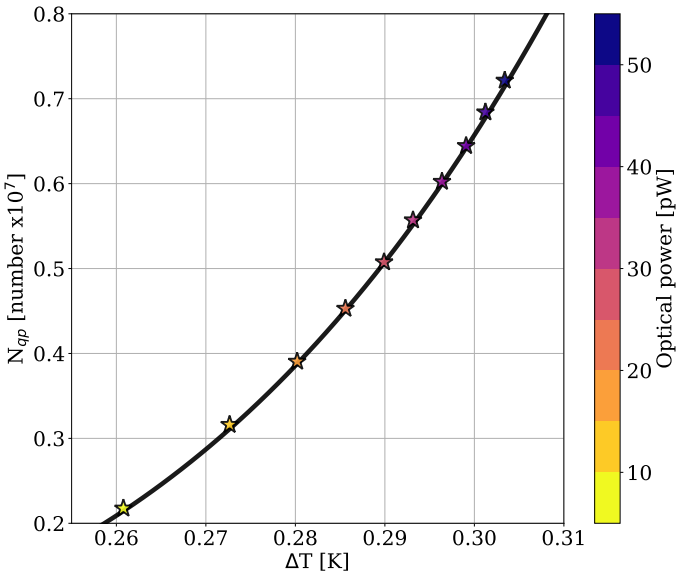

Figure 3.6: The black line is how the number of quasi-particles changes as a function of temperature as described by equation 2.39, whereas the data points (stars) represent the equivalent change in temperature as a function of optical load from equation 3.4.

The number of quasi-particles generated by an optical load of P_{opt} is given by

$$N_{qp} = \frac{P_{opt}\tau_{qp}}{\Delta} \tag{3.2}$$

Equation 2.40, which describes the temperature independent $N_{qp}\tau_{qp}$, can be combined with equation 3.2 to calculate the quasi-particle lifetime as a function of optical power for a detector of volume, V_T.

$$\tau_{qp} = \sqrt{\frac{N_0\tau_0}{P_{opt}2\Delta}}(k_b T_c)^{3/2}\sqrt{V_T} \tag{3.3}$$

Moreover, the same equations can be combined to calculate the number of quasi-

particles in the detector as a function of optical power.

$$N_{qp} = \sqrt{\frac{P_{opt} N_0 \tau_0}{2}} \left(\frac{k_b T_c}{\Delta} \right)^{3/2} \sqrt{V_T} \tag{3.4}$$

Now the number of quasi-particles generated in a detector volume is known, as a function of optical power, Kaplan theory (see section 2.7) can be used to determine how the temperature of the detector is impacted by equating this N_{qp} to the N_{qp} calculated using equation 2.39. This is the equivalent electron temperature required to increase the temperature to reflect how N_{qp} changes under load. Once this equivalent temperature has been calculated, it can be fed into the temperature model described previously in section 3.1.1.

The first step is to work out when N_{qp} from equation 2.39 is equal to N_{qp} calculated using equation 3.4, allowing a change in effective temperature, ΔT, to be extracted.

1. Calculate the number of quasi-particles generated as a function of P_{opt} with equation 3.4

2. Calculate the number of quasi-particles generated as a function of temperature with equation 2.39

3. See where the two values for N_{qp} are equal - this converts the power being absorbed into a change in electron temperature

Figure 3.6 highlights how N_{qp} changes as a function of temperature. Here, the black line is N_{qp} calculated using equation 2.39, whereas the star markers represent the equivalent change in effective temperature, as determined using equation 3.4. Next, this temperature change can be entered into the KID model to see how the resonator responds to optical power. To do this, ΔT must be added to a base temperature and steps 1-5 are repeated, the quality factors (Q, Q_c,Q_i) are calculated before step 11 is used to determine S_{21}.

Overall, increasing the optical power causes the temperature to increase and, as previously discussed and shown in figure 3.7, this causes the resonance curve to broaden and the dip to become more shallow. The associated fractional frequency shift is shown in figure 3.8. This result concludes the KID modelling aspect of this chapter.

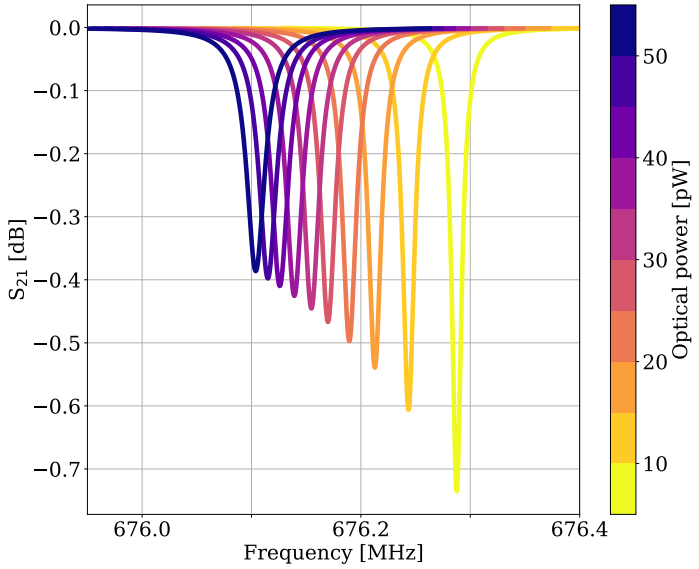

Figure 3.7: The transmission parameter, S_{21}, as a function of optical load for the detector shown in figure 3.3, as described by equation 2.61.

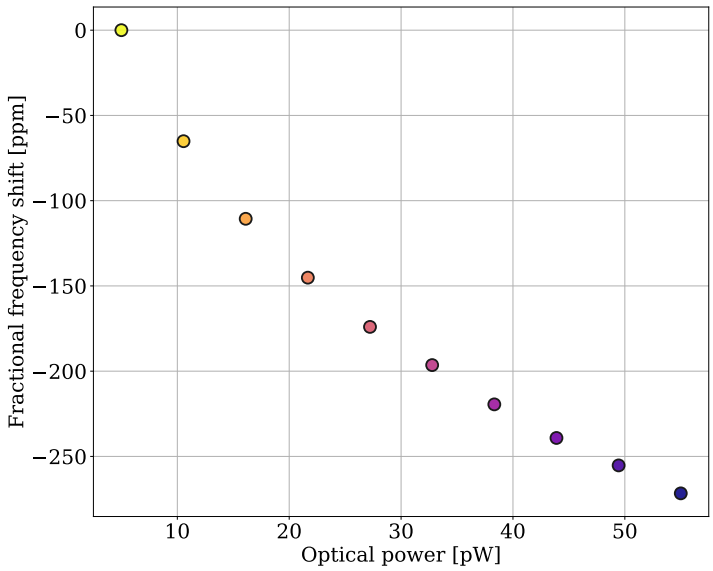

Figure 3.8: The fractional frequency response of the resonator with respect to the lowest optical power.

Clearly if the properties of the resonator are monitored, through measurements of S_{21}, the energy absorbed from incoming photons can be determined. However, aside from key considerations like the efficiency of the test system and optical filtering, one major impact on the effectiveness of KIDs will be noise. Thus to fully characterise a detector's performance, it is important to consider the sources of noise for a KID.

3.2 Noise of a KID

For the detectors presented in this thesis, there are a number of mechanisms which result in a noisy detector. Generally, noise is characterised through measurements of a fluctuating value of resonant frequency. Using a single-pixel homodyne measurement scheme, which will be described more thoroughly in section 4.1, monitors time-streams of $I(t)$ and $Q(t)$ - the real and imaginary components of S_{21}. For small shifts in the resonant frequency, f_0, the time-streams can be converted to determine df_0 using the following equation [77].

$$df_0(t) = \frac{I(t)\frac{dI}{df} = Q(t)\frac{dQ}{df}}{\left(\frac{dI}{df}\right)^2 + \left(\frac{dQ}{df}\right)^2} \tag{3.5}$$

where dI/df and dQ/df are the maximum response of the real and imaginary components of S_{21}, I and Q. In this thesis, only noise from a dark detector is present and therefore discussions of photon-noise, the desired noise limit of an optical detector, are omitted.

3.2.1 Detector Bandwidth

The fundamental limit on how fast a detector can respond to fluctuations in resonance is set by the bandwidth of a detector which, in turn, is governed by two time constants - the quasi-particle lifetime and the resonator ring-down time. Introduced in section 2.7, the quasi-particle lifetime, τ_{qp}, is defined as the time is takes for two quasi-particles to recombine after a Cooper pair is broken. The resonator ring-down time is the time is takes for a resonator to relax back to its unperturbed state and is described by [69]

$$\tau_{res} = \frac{Q_{tot}}{\pi f_0} \tag{3.6}$$

To ensure the time constant of the detector is governed by the material parameters, a resonator is generally designed so that $\tau_{qp} > \tau_{res}$. A quasi-particle lifetime of $\sim 10^2$ - $10^3 \mu$s is typical of an aluminium LEKID, with a resonator ring-down time of order 10μs.

3.2.2 Generation-Recombination Noise

A superconducting film in thermal equilibrium at a given temperature will undergo quasi-particle generation and recombination, creating an error in the anticipated number of quasi-particles at any given point in time, resulting in fluctuating kinetic inductance. This fluctuation is characterised by generation-recombination (G-R) noise, which is well modelled as a Poisson process and will lead to an overall shot noise. G-R noise represents the fundamental sensitivity limit for a dark LEKID.

For a superconducting film, thermal equilibrium means the number of quasi-particles N_G generated must equal the number recombining N_R per second, $N_G = N_R$. The total number of quasi-particles in a system is given by the product of the quasi-particle lifetime and number of quasi-particles recombining per second. The quasi-particle lifetime here is defined as the time taken for a Cooper pair to meet another quasi-particle and to recombine recombine once split. The factor of two in equation 3.7 accounts for the fact that in the time τ_{qp}, two quasi-particles recombine.

$$N_{qp} = \frac{N_G \tau_{qp}}{2} = \frac{N_R \tau_{qp}}{2} \tag{3.7}$$

Re-arranging equation 3.7 results in $N_G = 2N_{qp}/\tau_{qp}$. The number of quasi-particles being generated and recombining are noisy and are dictated by Poisson statistics, where the error in a quantity is given by the square root of the quantity.

$$\Delta N_G = \sqrt{N_G} = \sqrt{\frac{2N_{qp}}{\tau_{qp}}} \tag{3.8}$$

To determine the total G-R noise contribution, the errors in generation and recom-

bination need to be added together in quadrature.

$$\begin{aligned}\Delta N_{qp} &= \sqrt{(\Delta N_G)^2 + (\Delta N_R)^2} \\ &= \sqrt{\left(\sqrt{\frac{2N_{qp}}{\tau_{qp}}}\right)^2 + \sqrt{\left(\sqrt{\frac{2N_{qp}}{\tau_{qp}}}\right)^2} \\ &= 2\sqrt{\frac{N_{qp}}{\tau_{qp}}}\end{aligned} \tag{3.9}$$

The power spectral density S_N quantifies the G-R noise in a system. It is the power present in a signal as function of frequency, per unit frequency, and has a roll-off term associated with quasi-particle lifetime [78].

$$S_N = \frac{4N_{qp}\tau_{qp}}{(1+\omega^2{\tau_{qp}}^2)} \tag{3.10}$$

S_N has units of N^2/Hz. As N_{qp} depends on temperature and detector volume, G-R contributions to the noise can be reduced through operating at low temperatures and designing a resonator which has a smaller device volume. However, there is a non-zero constant level of quasi-particles at low temperatures which have been measured experimentally. This divergence from theory observed at $\sim$ 170 mK places a limit on detector sensitivity [79].

3.2.3 Amplifier Noise

Amplifier noise is an unavoidable consequence of the electronic readout set-up, presented in section 4.1, which is described by Johnson noise.

$$\sigma_{amp} = \sqrt{4k_B T_{amp} R_{line}} \tag{3.11}$$

where R_{line} is the impedance of the feedline, which set to 50Ω and T_{amp} is the temperature of the amplifier. A clear way to reduce the amplifier contribution to the overall noise is to reduce its temperature. This is typically implemented through low-noise amplifiers (LNAs) installed within the cryostat at temperatures below 6 K. Amplifier noise is flat and can therefore be treated as background noise.

3.2.4 Two-Level Systems

Amorphous dielectrics have a tendency to degrade the performance of detectors through the introduction of TLSs noise. At boundaries between the various layers

of a detector, non-uniformities in the electric field around the KID, TLS interactions occur where electrons tunnel between the various minima of the potential. This results in localised variations in the quasi-particle density and the dielectric constant of the superconductor which, in turn, results in a fluctuation in resonant frequency. Noise originating from TLSs is described by the semi-empirical model in Gao et al [48].

Generally, the noise created by TLSs has a slope, where f^{-x} where x is ~ 0.5 and is most noticeable in the low-frequency regime of the noise power spectral density, below $\sim$ 10 Hz. The noise level due to TLSs has been observed to decrease with increasing readout power due to the TLSs becoming saturated [55]. Other techniques used to reduce TLS contributions include careful preparation of the silicon substrate, removing any existing oxides before metal deposition.

Moreover, it is also possible to remove the amorphous material from regions of high electric fields to reduce the TLSs - a technique utilised in this thesis. [47, 49] Further discussion of TLSs and how to measure and characterise their impact on resonator performance is explored in chapter 5.

3.3 Summary

This chapter has focused on modelling the response of a LEKID to both temperature and optical load, which relies on the equations presented in chapter 2. Using the model, the relationship between the number of quasi-particles generating in a film is equivalent to a change in temperature, which can be equated to an incident optical load. Clearly if the properties of the curve are monitored, it is possible to determine the power absorbed from a stream photons.

In the second part of this chapter, the impact of various noise sources on the performance of a LEKID. In a dark detector, the sensitivity limit is governed by generation-recombination noise, however there will also be contributions from any amplifier within the readout electronics chain. Moreover, through the additional of amorphous materials to a detector, the introduction of noise due to TLSs have also been presented. TLSs generally impact the low-frequency regime of the noise, below $\sim$ 10 Hz, and are characterised by a $1/f^x$ slope.

4

Overview of Detector Arrays

Overall, there are two different varieties of prototype devices tested during this research project - the dielectric device and antenna-coupled device. The dielectric device focused on exploring the impact of adding a dielectric material to resonators, whereas the antenna-coupled device consisted of resonators coupled to an antenna via a transmission line, paired with dark detectors to aid evaluation of stray light.

In this chapter, the readout electronics utilised to measure the performance of detectors are presented. Moreover, the main differences between the device types and detailed properties of each array of detectors are presented in this thesis, including number of resonators, thickness of the device layer and other relevant properties. Moreover, the fabrication steps required to realise each device type are reviewed. Each device was carefully fabricated at the Pritzker Nanofabrication Facility (PNF) at the University of Chicago by collaborators P.S. Barry, E. Shirokoff and Q.Y. Tang.

4.1 Experimental Techniques

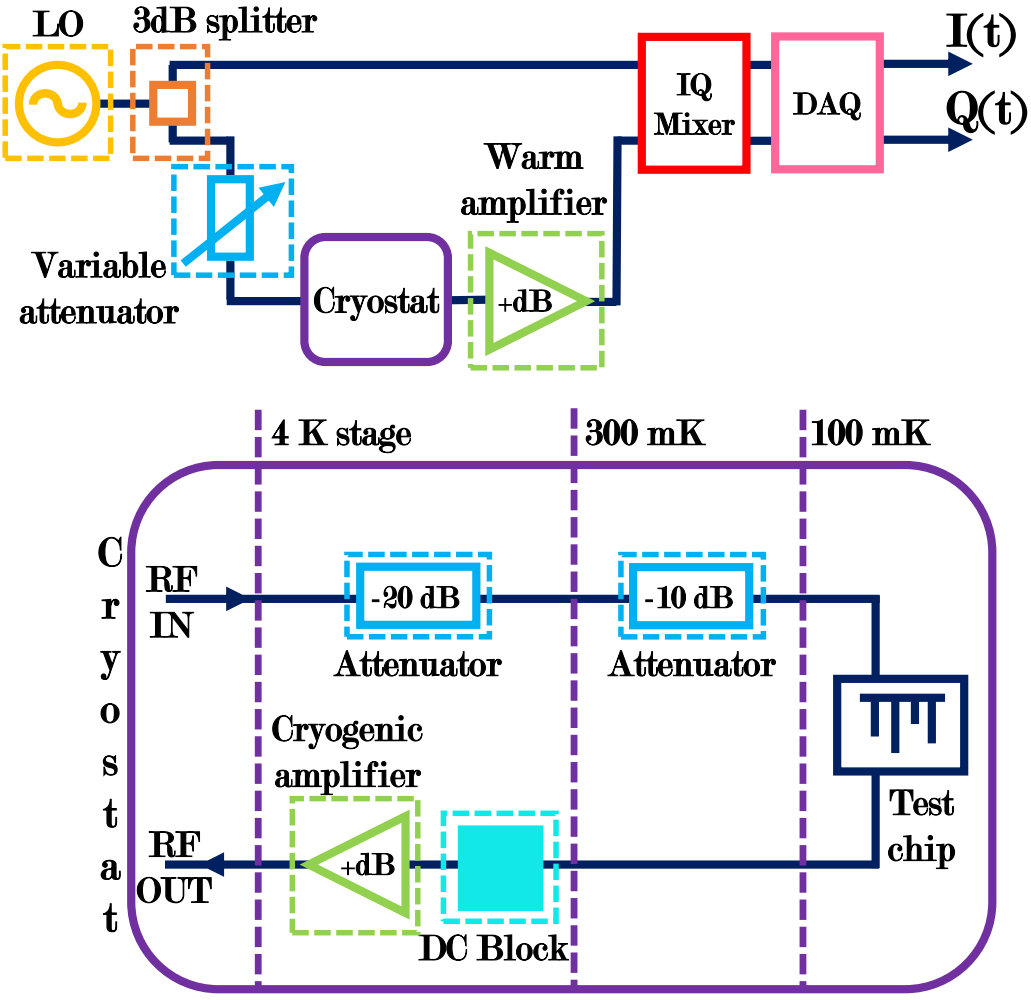

Figure 4.1: The electronics readout chain for a homodyne readout. The local oscillator (LO) outputs a signal, which is split into two components by the 3dB splitter. One signal travels towards the IQ mixer, whilst the other travels through the detector array. The two signals are recombined with the mixer and the output signal is proportional to S_{21} of the detector array.

To measure the performance of the devices presented in this thesis, there are three types of experimental set ups used, which include (i) dark measurements, where the temperature of the detectors is changed, (ii) optical measurements, where an optical source is varied in power and (iii) spectral measurements, where the spectral

response of detectors is measured in response to an external radiation source. All of these measurements require a VNA for simple measurements of S_{21}, a single pixel, homodyne readout scheme to determine noise or a combination of the two for spectral measurements [6].

By monitoring the forward transmission, S_{21}, of a microwave probe signal coupled to KID resonators, it is possible to readout each detector, measuring key properties such as the resonant frequency and quality factor. As presented in chapter 2, for a KID resonator, S_{21} as a function of angular frequency is given by $S_{21}(\omega) = (Q_{tot}/Q_i)[(1 + 2jQ_{tot}x_r)/(1 + 2Q_{tot}x_r)]$ [7].

A homodyne readout mixing system is often utilised to measure the S_{21} transmission of a detector array and resonant frequency noise. The electronics readout chain for a homodyne system is shown in figure 4.1. Using a local oscillator (LO), a variable frequency signal generator, outputs a signal at the readout frequency which splits at the 3dB splitter to travel down two different paths - one towards the detector array and one through an IQ mixer. The IQ mixer is utilised to combine the two signals after the detector chip, and results in a digitised signal. Because the IQ signal receives signals of the same frequency from the detector path and LO, the I and Q outputs will be mixed down to DC levels with an $I + jQ$ proportional to the S_{21} of the cryogenic system - i.e the S_{21} transmission of the detectors. Recall I and Q are the real and imaginary components of S_{21} respectively.

To control the power used to readout the device, the input signal to the cryostat must be attenuated down to a lower power level. This is achieved using variable attenuators at room temperature and fixed attenuators within the cryostat, located between the 100 mK and 4 K stages to reduce the attenuators contribution to the Johnson noise component. After passing through the detector array, a thermal break in the cable is created using a DC block, which reduces thermal power propagation before the signal is then amplified to its original power level through a LNA (cryogenic amplifier) and warm, room temperature amplifier. Most of the amplification occurs within the cryostat, at cryogenic temperatures, to minimise the noise added to the system.

This is a brief introduction to the electronic set up required to measure the S_{21} transmission of a detector and monitor the noise in resonant frequency. In

subsequent chapters 5, 6 and 7, details on dark, spectral and optical measurements are presented in the necessary detail.

4.2 The Dielectric Detectors

To investigate the impact of adding a dielectric material to our resonators, a simple aluminium device was created, where different resonators have different levels of dielectric coverage. The detectors on this chip were designed by Q.Y. Tang. The dielectric device consists of an aluminium device layer, on a silicon wafer, with the dielectric SiN_x grown over the resonator. Each device consisted of 18 resonators organised into 3 banks of dielectric coverage, including: bare, dielectric-free resonators, partially covered resonators with dielectric over the inductive element only and fully-covered resonators with dielectric over all of the resonator. This scenario is described in Figure 4.2.

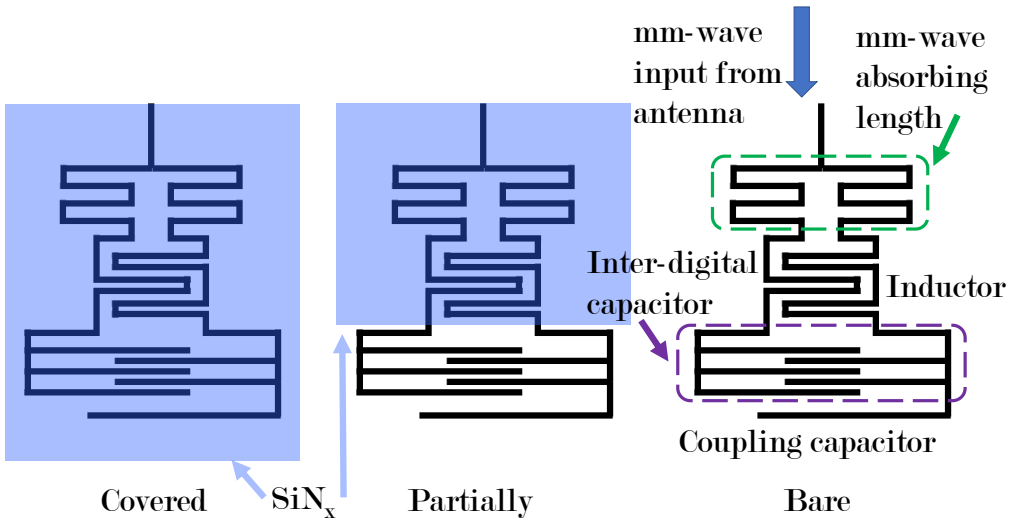

Figure 4.2: Schematic describing the three different dielectric scenarios presented in this thesis. Left: SiN_x covers the entire resonator. Centre: SiN_x is over the inductor only. Right: Resonator free of dielectric. This addition of dielectric is necessary for transmission line coupling in antenna-coupled devices.

The physical layout of the chip is shown in figure 4.3 and was created using the software Klayout, which is used to edit GDSII mask files [80]. Blue is the metal,

aluminium layer whereas pink highlights where the dielectric SiN_x is placed. Overall, the chip is 2.70 by 2.67 mm in size. The devices are organised into groups on the mask also, in accordance to their dielectric coverage. Starting from the bottom of the mask, the covered resonators are numbered 0 - 5, the partially-covered are detectors 6 - 11 and the bare resonators, located towards the top half of the mask, are numbered 12 - 17.

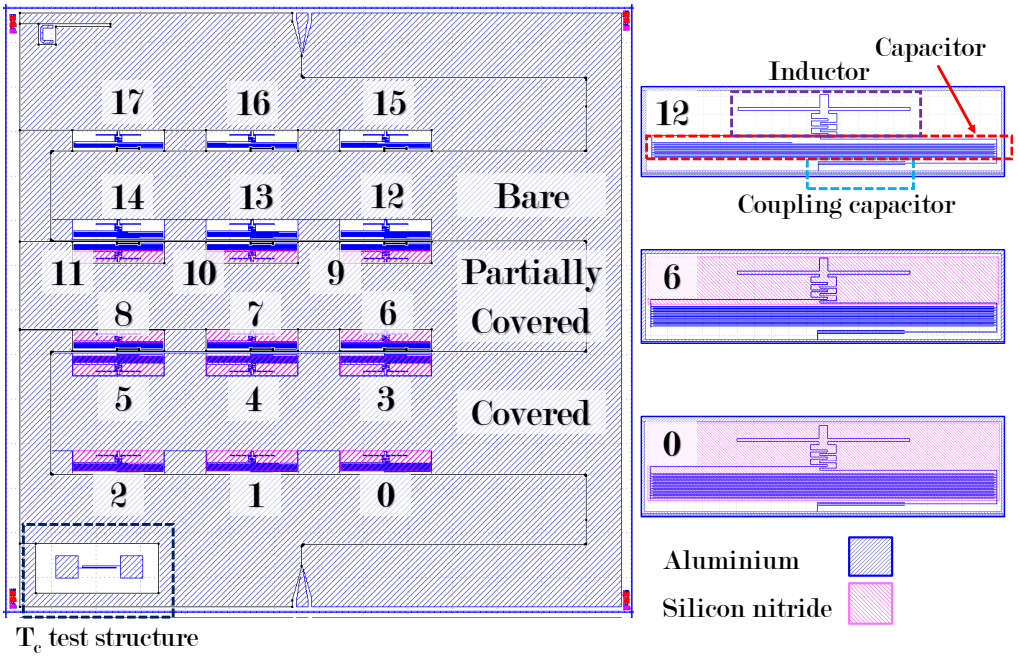

Figure 4.3: The overall detector layout of the chip, as viewed in the mask-editing software, Klayout. [80] Here, blue represent sections of the device which are aluminium, whereas pink indicates where SiN_x has been added. Detectors 0 - 5 are covered with dielectric, 6 - 11 are partially-covered detectors and 12 - 17 are the bare resonators. A T_c test structure is visible in the bottom-left corner of the array.

On this array of detectors, each resonator has a inductor volume of 1968 μm^3 and therefore the resonant frequency of each detector is set by adjusting the capacitance. In this design, the coupling capacitor is kept constant for each detector.

4.2.1 Device 1

Device 1 is a single-layer, dark array of 18 thin-film aluminium LEKIDs, with various SiN_x coverage designed to investigate the impact of adding the dielectric material

to the performance of the detectors. Here, dark means the devices are not coupled to an antenna and data from device 1 forms the basis of chapter 5. A diagram depicting the different device layers and thicknesses is shown in figure 4.4, with the dielectric coverage of a partially-covered detector shown. The aluminium detector layer is 50 nm thick with 500 nm of the dielectric silicon nitride over the detector.

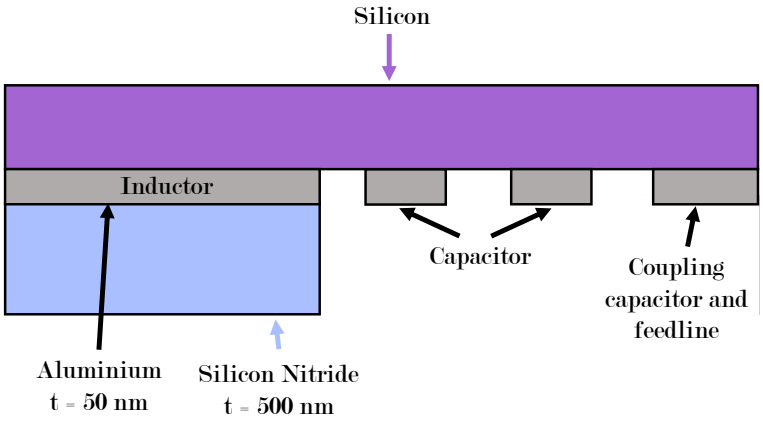

Figure 4.4: Depiction of different device layers for device 1. It is a two-layer device with a 50-nm layer of aluminium and a 500-nm layer of silicon nitride. This is an example of a partially-covered device with silicon nitride on the inductive meander only.

In device 1, the resonators are grouped into three frequency banks, which span (i) 786-801 MHz, (ii) 1029 - 1058 MHz and (iii) 1100 - 1166 MHz, each containing 6 resonators. The three banks enable resonators to be identified when measured. The lowest frequency resonators, bank (i), are completely covered by SiN_x, except for the coupling capacitor, and are expected to have the highest loss (figure 4.2, left). The partially-covered resonators (figure 4.2, centre), bank (ii), have SiN_x over the inductor only – this is the desired dielectric coverage for optical devices [8]. The highest frequency bank of resonators, bank (iii), are completely free of dielectric (figure 4.2, centre). While this does not allow for optical coupling via a microstrip, this structure serves as a reference device for the optical devices.

The expected S_{21} frequency response, as simulated using the EM software Sonnet, is shown in the upper panel of figure 4.5. It is difficult to accurately simulate partially covering a detector with a dielectric because Sonnet does not allow for layers to be partially filled. Therefore, to estimate the impact of adding SiN_x to

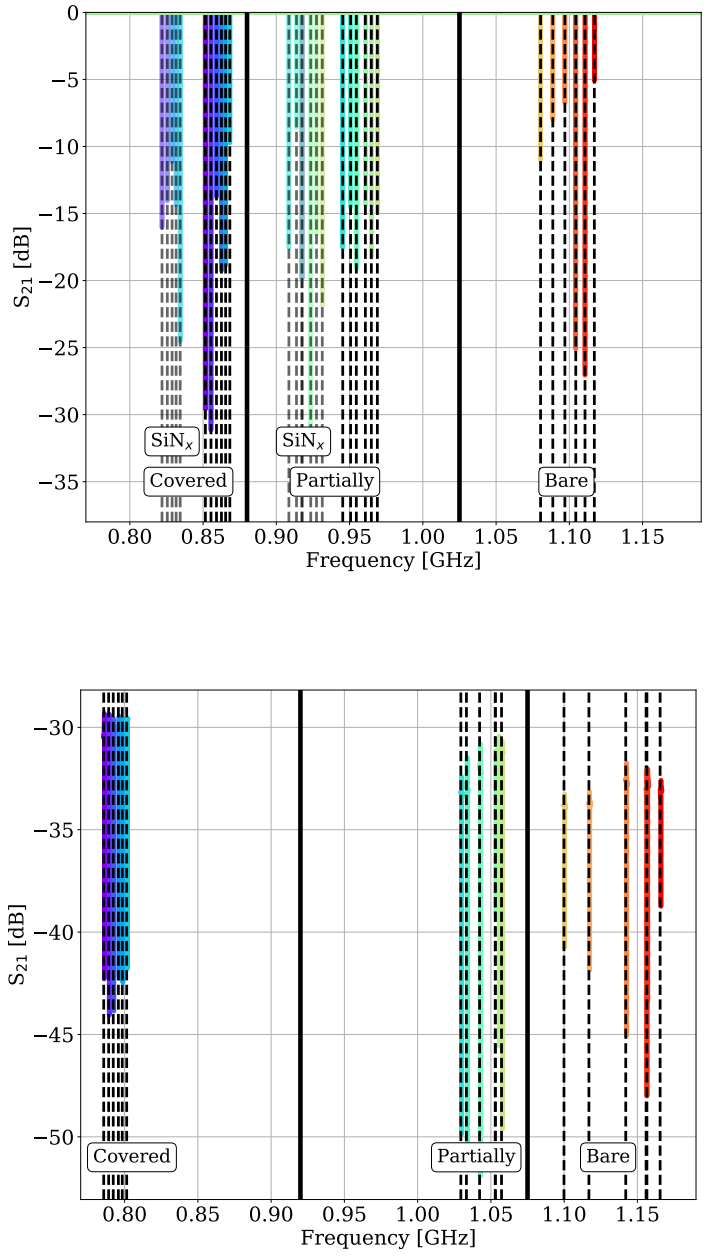

Figure 4.5: S_{21} for each detector of device 1 from Sonnet simulations in the upper panel. There are three banks of resonators: covered, partially-covered and bare, grouped according to the dielectric coverage shown in figure 4.2. There are two sets of simulations for the covered and partially-covered detectors, one with and one without SiN_x, which are labelled accordingly. The lower panel shows S_{21} measured for each resonator of device 1 using a VNA.

detectors, the detectors are simulated before and after adding a layer of SiN_x to the entire simulation. The resonant frequency of the detector is expected to be between these two values. For the lowest frequency bank of detectors, however, the measured resonant frequencies of the covered resonators should sit close to the SiN_x results, the only difference between a fully-covered simulation and measured device is that the coupling capacitor is free of dielectric on a real device. Adding dielectric to the middle bank of resonators, the partially-covered resonators, results in a simulated resonant frequency shift of $\sim$ 40 MHz.

The observed S_{21} frequency response, as measured using a VNA, is shown in the lower panel of figure 4.5. With a full array of 18 resonators, the yield of the array is 100 %. Moreover, the detectors are still grouped into three different banks according to dielectric coverage, but there is a significant amount of scatter in resonant frequency for the highest frequency bank of detectors, the bare resonators. Although the band has only moved by 1 MHz, it is now spread over $\sim$ 70 MHz instead of the designed 30 MHz. One possible explanation comes from etching the layer of SiN_x from unwanted areas during the fabrication process, however a later investigation into this process suggested etching had no impact. The bare frequency bank is $\sim$ 40 MHz lower than expected, whilst also spanning a fractionally larger band of frequencies, changing from 13 to 16 GHz, as measured from the SiN_x simulations in figure 4.5. The middle bank of partially covered detectors has moved the most, shifting 75 MHz higher than the no-SiN_x Sonnet simulations and spanning 30 MHz instead of 24 MHz.

The detector layout, device layers and a comparison of the predicted and measured resonant frequencies have been presented in this chapter for device 1. For measurements of the frequency response to temperature and the noise in resonant frequency, df0 (introduced in section 3.2), see the next chapter – chapter 5. In the next section of this thesis, the devices which are optically-coupled to a microstrip and antenna are presented.

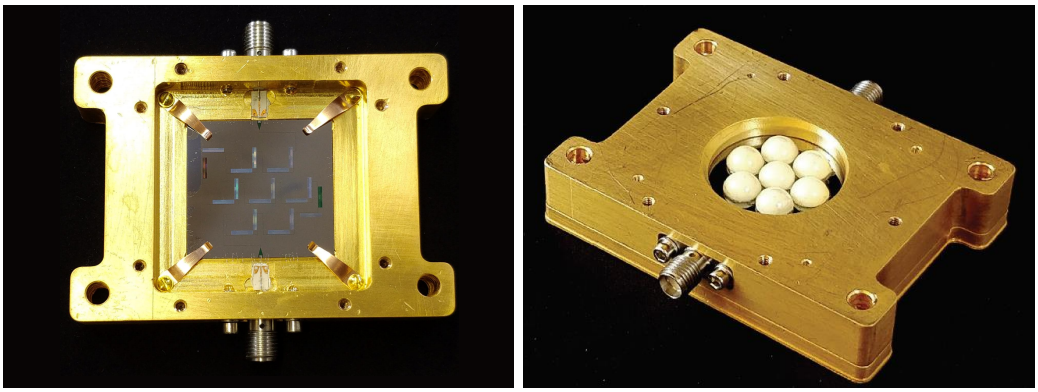

(a) (b)

Figure 4.6: (a) Image of the prototype test array of mc-LEKIDs in a gold-plated OFHC copper sample box.(b) The lenslet array which focuses light on to planar twin-slot antennae, before travelling down a microstrip transmission line and being absorbed by the absorbing meander of a LEKID. *Image credit: P.S. Barry*

4.3 The Antenna-Coupled Detectors

An array of dark detectors, which are not designed to respond to optical light, are of little use as a light detector in a CMB experiment, therefore an array of optical devices are needed. Here, optical means the device is connected to an antenna via a microstrip transmission line. The overall aims for this style of array was to (i) test the more complicated fabrication process to realise optically-coupled device, to (ii) see if light could be coupled into a LEKID using an antenna and microstrip and (iii) add filtering structures to the microstrip to limit the frequencies travelling towards the LEKID.

On detector arrays of this second device style, there are nineteen detectors per chip with light coupled in via an array of seven lenslets. Underneath each lenslet sit a pair of detectors, an optical detector coupled to an antenna and a dark detector (not coupled to an antenna) to help determine if there is stray light within the system. Images of a prototype test array in a sample box and the lenslet array are shown in figure 4.6. The layout of an optical device, Device 2 is shown in figure 4.7. Outside of the footprint of the lenses sit five more dark detectors to further test for stray light. Furthermore, dark detectors X_0 and X_2-X_4 are fully covered

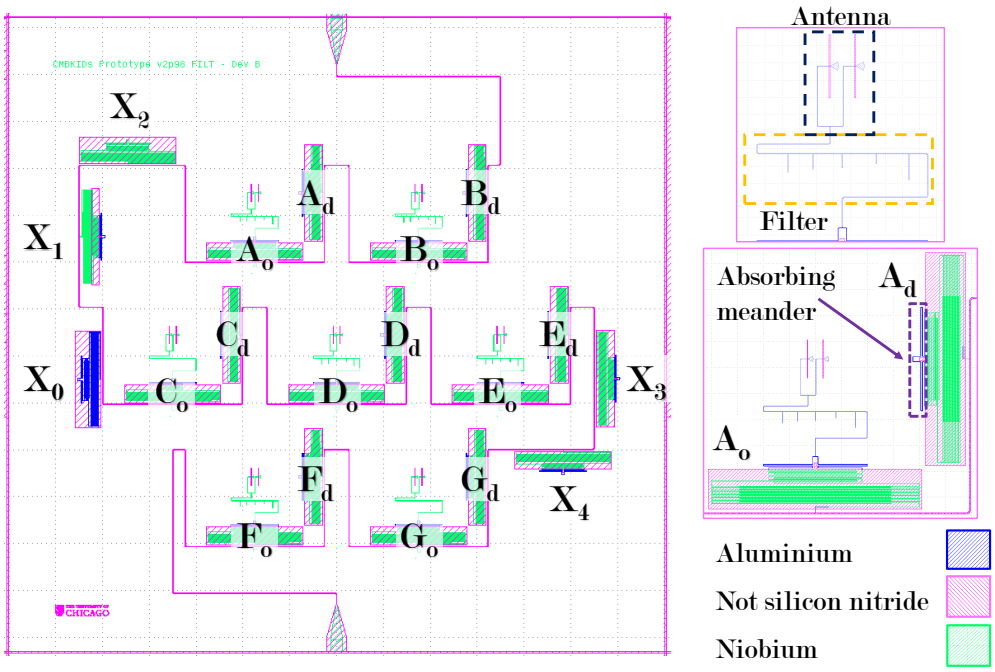

Figure 4.7: The overall detector layout of the optical chip, as viewed in the mask-editing software, Klayout [80]. Here, blue represent sections of the device which are aluminium, pink is where the dielectric SiN_x has been removed and green is niobium. The seven pairs of detectors, A-G, are composed of an antenna-coupled detector (KID_o) and a dark detector (KID_d). The detectors X_0-X_4 sit outside of the footprint of the lens. X_0 is a covered Al KID, X_1 is a partially-covered KID and X_2-X_4 are covered Al/Nb KIDs.

KIDs whereas X_1 is partially covered. Moreover, detector X_0 is an aluminium-only device, whilst the rest have aluminium absorbing meanders and niobium capacitors. Both the inductor volume and capacitor values are varied here to set the resonant frequency of each resonator. Details about individual detectors are discussed below.

4.3.1 Device 2

Device 2 is an array of dark (not connected to the antenna structure) and optically-coupled detectors composed of aluminium and niobium. A diagram depicting the different device layers and thicknesses is shown in figure 4.8, the aluminium layer is 50 nm, the niobium layer is 250 nm and the silicon nitride layer is 500 nm in thickness. To form the microstrip and the twin-slot antenna structures, a 250 nm

groundplane of niobium is grown on top of the silicon nitride layer. To enable coupling to an antenna, a silicon lenslet seating wafer, is needed with pockets for the lenslets to sit within. Details about the fabrication of devices is presented later in the chapter.

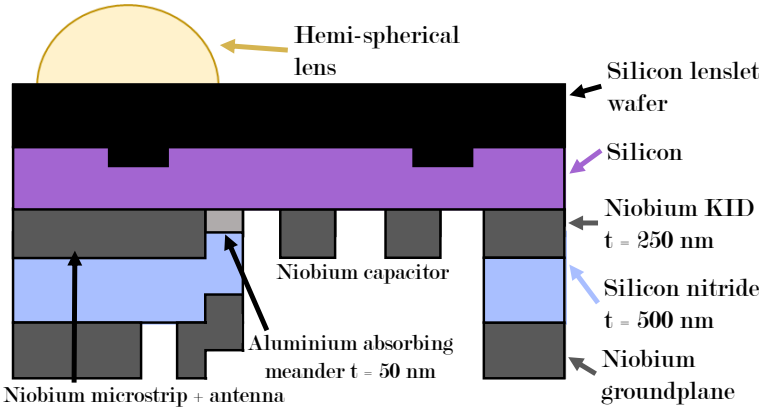

Figure 4.8: Different device layers for device 2. It is a three-layer device with a 50-nm layer of aluminium for the inductor, 250 nm of niobium above and below a 500-nm layer of silicon nitride.

The array yield is defined as the number of detectors measured divided by the number of detectors fabricated and here it is 73.7 % or 14/19 detectors. Resonators X_0, X_1, B_o, B_d and X_4 did not yield, which makes identifying resonators more challenging. Overall, the resonators are located between 800 - 1100 MHz. To identify resonators, their resonant frequency and relative frequency response was taken into account. Accurate identification of resonators requires an array of beam maps to be produced by illuminating each resonator in turn and monitoring the each detector's response at different angles. Unfortunately this was not possible at the time this data was obtained.

The geometry of the LEKIDs is complex on this device, with varying inductor volumes, capacitors and coupling capacitor values. Primarily, the most interesting difference between detectors for the studies completed in this thesis is the inductor volume as it is a parameter of device responsivity (see equation 2.39). The volume of the absorbing meander of each detector is presented in table 4.1. Here, detectors X, A, D, and G all have the same aluminium volume of 1214 μm^3, F detectors have a larger volume of 1254 μm^3, and detectors C and E have smaller volumes of 1014

and 914 μm^3 respectively.

Detector	**Aluminium Volume [μm^3]**	**Total Volume [μm^3]**
X_2, X_3	1214	18984
F_o, F_d	1254	28569
A_o, A_d	1214	18984
D_o, D_d	1214	18984
G_o, G_d	1214	18984
C_o, C_d	1014	12784
E_o, E_d	914	6264

Table 4.1: The aluminium inductor volume and total inductor volume for each resonator of device 2

The simulated S_{21} frequency response from Sonnet is shown in the upper plot of figure 4.9. The X resonators represent the upper and lower frequency boundaries for the device, with a total readout bandwidth requirement of 479.8 MHz. In between the two extremes, resonators are grouped into approximately six bands of detectors. The first two bands, comprised of the F detectors and the optical A,D and G detectors are located near 700 MHz. The third band consists of the dark A,D and G detectors at $\sim$ 750 MHz. In between 800 and 900 MHz are the fourth, fifth and six group of detectors which are C_o, C_d and the E detectors.

The measured S_{21} frequency response from a VNA is shown in the lower plot of figure 4.9. The detectors are still approximately grouped into six bands between the X detectors, but X_2 has moved up by 86.1 MHz and X_3 by 95.2 MHz, meaning the total readout bandwidth now required is 488.9 MHz – an increase of 9.1 MHz. Resonator spacing appears to be mostly conserved, but the frequency space between X_2 and F_o is noticeably smaller with a decreased spacing of 23.1 MHz.

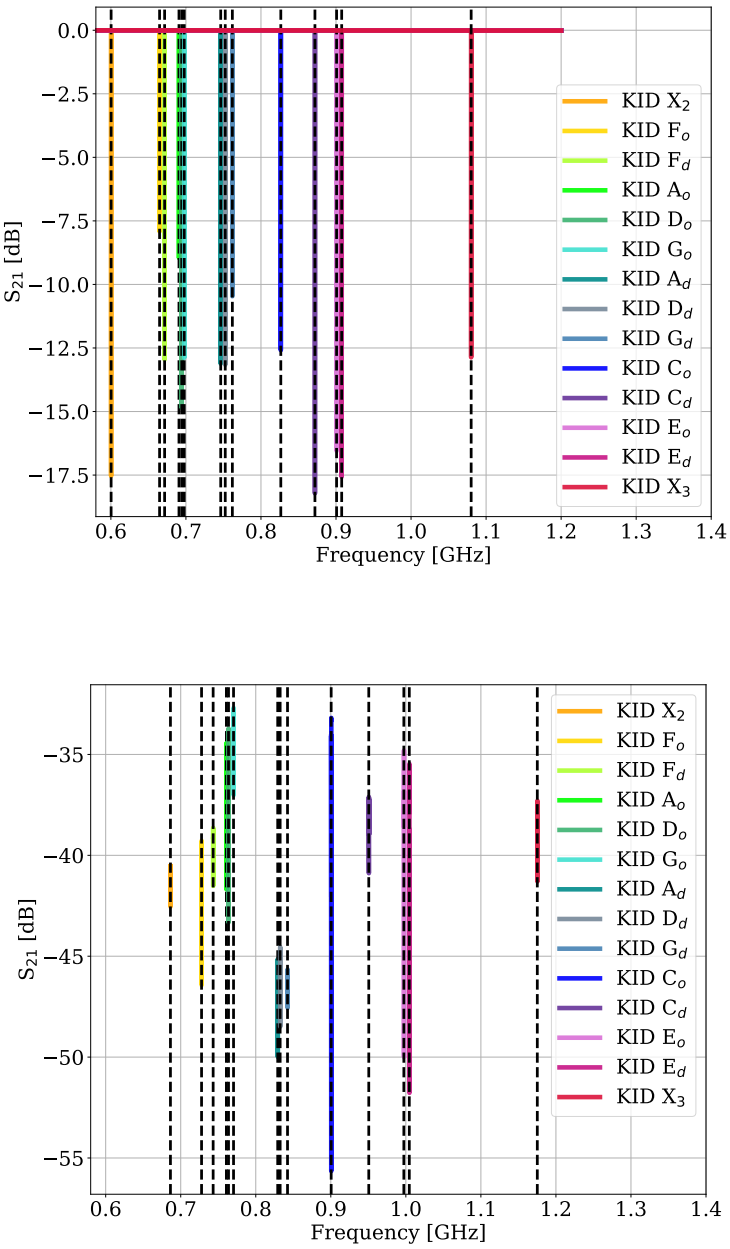

Figure 4.9: S_{21} for each detector of device 2 from Sonnet simulations is shown in the upper panel. The lower panel contains S_{21} measured for each resonator of device 2 using a VNA.

4.4 Fabrication

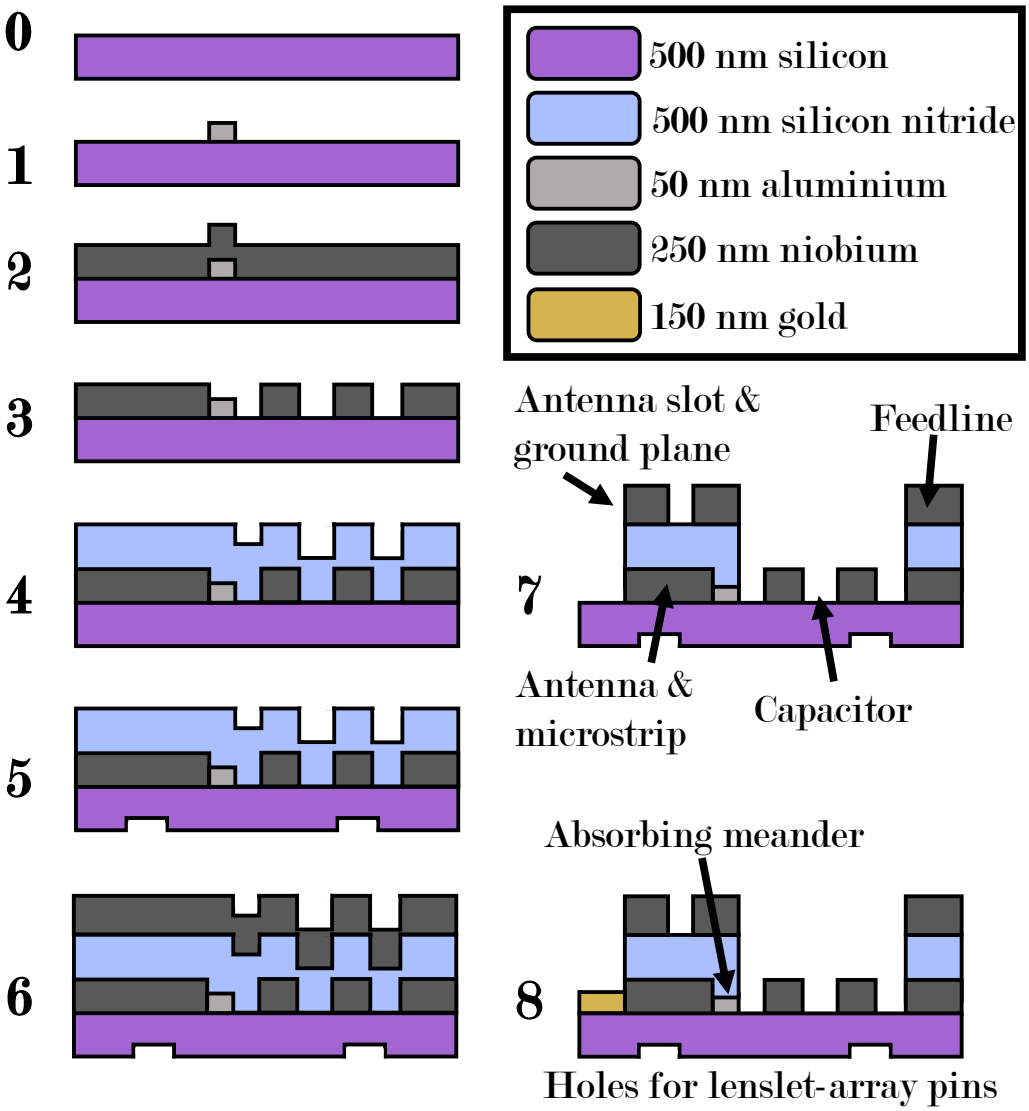

Figure 4.10: The different stages of fabrication of an array of mc-LEKIDs, adapted from the diagram in Tang. [81] The stages are: (1) depositing and etching aluminium, (2+3) depositing and etching niobium, (4) depositing silicon nitride, (5) etching holes for lenslet alignment posts, (6) depositing niobium groundplane, (7) etching niobium and silicon nitride and (8) depositing gold pads. The details of each deposition stage are presented in section 4.4.

To realise both detector variations presented so far in this thesis requires deposition of a superconductor onto a silicon surface, and etching through lithographical

processes. The steps outlined below relies on the paper produced by Tang et al, although aspects of the process have changed since its publication, and a month of shadowing collaborators in the Pritzker Nanofabrication Facility (PNF) based at the University of Chicago [81]. A diagram outlining the device layers throughout the fabrication process is shown in figure 4.10.

Step 0 - Preparing wafer & maintaining cleanliness

The wafer is first cleaned with a sonicated acetone bath, isopropyl alcohol (IPA) and deionised (DI) water bath. Next, the wafer is placed in a hydrofluoric (HF) acid bath dip to remove any native oxide layer, followed by a 150°C vacuum bake for 15 minutes to dehydrate the wafer.

Important To ensure the wafer remains clean throughout all processes, the wafer is cleaned using acetone, IPA, and DI water baths, prior to each lithography step, and is then vacuum baked at 90 °C for 3 minutes to dehydrate the surface.

Step 1 - Adding aluminium device layer

50 nm of aluminium is deposited using an ATC 2200 ultra-high vacuum (UHV) sputtering system[1]. After spinning photoresist (AZ 1512) on to the surface, the aluminium is patterned using a mask-less lithography writer from Heidelberg Instruments[2], followed by a wet etch for patterning to avoid etching the silicon substrate. This is standard wet etchant for aluminium and it contains phosphoric and nitric acid.

Step 2 and 3 - Adding niobium device layer

Before depositing niobium, the wafer is placed in an oxygen plasma asher[3] for $\sim$ 1 minute to remove any remaining photoresist and any aluminium oxide that has now formed on the wafer's surface. This involves being heated to 70°C with a 300 W oxygen plasma being applied for 240 seconds to descum the wafer before using a NMP (1-Methyl-2-pyrrolidon) bath heated at 80°C.

Identical to the aluminium deposition, 250 nm of niobium is deposited via sputtering, photoresist is spun onto the surface before using the maskless Heidelberg for patterning. However, a dry fluorine etch is instead utilised for niobium removal and

[1]https://pnf.uchicago.edu/equipment/detail/aja-atc-2200-uhv-sputtering-system/
[2]https://pnf.uchicago.edu/equipment/detail/heidelberg-mla150-direct-write-lithographer/
[3]https://pnf.uchicago.edu/equipment/detail/ion-wave-10-plasma-asher/

etches $\sim$ 20-30 nm of exposed regions of silicon around the meander and capacitor. The wafer is placed back in an oxygen plasma asher for $\sim$ 1 minute to remove any remaining photoresist.

Step 4 - Adding silicon nitride layer

Next, 500 nm of silicon nitride is deposited onto the surface using a high-density plasma chemical-vapour deposition system (HDP CVD) [4] before spinning a layer of photoresist. At this point, the wafer is least susceptible to scratching and is most sturdy, therefore this is when any backside processing occurs.

Step 5 - Adding alignment posts for lens wafer

Around 3 μm of photoresist is spun onto the backside of the wafer, before patterning the holes for the alignment posts using the Heidelberg. To etch silicon requires a Plasma-Therm Versaline Deep Si RIE system which etches around 100 μm into the silicon[5]. The holes are oversized by 10 μm to ensure the posts of the lenslet array, shown in figure 4.8, will fit. As before, the wafer is placed back in an oxygen plasma asher for $\sim$ 1 minute.

Step 6 - Adding niobium ground plane

The deposition process for 250 nm of niobium groundplane is the same as step 2.

Step 7 - Removal of silicon nitride

With photoresist spun on the surface, and patterned using the Heidelberg, the antennas can be exposed through etching of a gap in the groundplane with a dry fluorine etch. Moreover, this etch can also be used to remove the silicon nitride from the capacitor and pads for wire bonding.

Step 8 - Adding gold pads

At this stage, device fabrication is almost complete aside from one important component – gold pads for heat sinking the array to the chip holder. This is an additional step that is the result of observed wafer heating in previous experiments and is deposited using a lift-off process. Titanium is deposited before the gold processing which helps the gold stick to the silicon wafer.

The fabrication process detailed above is for the mc-LEKIDs, however it utilises

[4] https://pnf.uchicago.edu/equipment/detail/plasma-therm-apex-slr-hdpcvd/

[5] https://pnf.uchicago.edu/equipment/detail/plasma-therm-versaline-deep-si-rie/

steps required to realise the two-layer dielectric detectors. To fabricate the dielectric detectors also presented in this chapter requires step 0, 1, 4 and the silicon nitride etching from step 7.

4.5 Summary

Two different types of detector arrays are presented in this chapter – the dielectric device and antenna-coupled device. The dielectric device is required to explore the impact of adding dielectric to resonators, and results from this device are presented in the next chapter. Chapters 6 and 7 focus on the results of the antenna-coupled device which consist of resonators coupled to an antenna via a transmission line.

This chapter has provided an overview of a single-tone, homodyne readout system utilised to measure the S_{21} of a resonator and monitor the frequency noise, df. Moreover, comparisons between the predicted and measured resonant frequencies of each detector array are presented, to identify detectors and measure array yield, alongside details of the fabrication process required to realise the arrays.

5

The Dielectric Requirement

To realise the mc-LEKID, an amorphous material is deposited over the LEKID to form the microstrip dielectric. This dielectric requirement of the microstrip is problematic for the performance of the detectors because amorphous materials have a tendency to degrade the quality factor and low-frequency noise performance of the KID resonator via the introduction of TLSs [9, 10].

This chapter presents the equations needed to describe the impact of TLSs on KID resonators, and the results of dielectric prototype devices described earlier in section 4.2. Moreover, these results have been published in the Journal of Low Temperature Physics [11]. The devices presented in this chapter were designed and fabricated by Q.Y. Tang and P.S. Barry.

5.1 Resonator response

To quantify the effect of adding lossy dielectrics to the KID resonators, we have to combine two sets of behaviour: (i) the expected frequency response in accordance

with superconducting resonator theory using a BCS superconductor model, and (ii) the additional frequency response created by TLSs in the dielectric and is described by models put forth by Gao [55, 48].

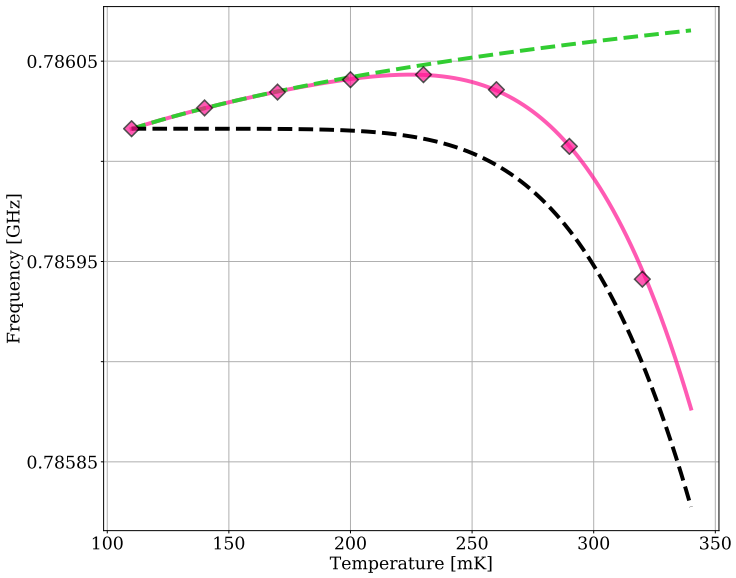

Figure 5.1: Frequency as a function of temperature for an example covered resonator, as described in figure 4.2(a). The dashed lines are the two different components to the fit of the data - the expected fractional frequency shift (dashed *black* line) and the additional shift caused by TLSs, calculated from equations 5.3 and 5.4 (dashed *green* line). The combined fit is a solid line.

An example resonator responding to a change in base temperature is shown in figure 5.1. To characterise the expected response of the resonator to a change in temperature, as determined by Mattis-Bardeen superconductivity, we must calculate the change in complex conductivity due to temperature change and therefore change in the number of quasi-particles – $d\sigma/dn_{qp}$ [66]. The method below follows that which is outlined in chapter 2 of Gao 2008 [55]. The expected Mattis-Bardeen frequency response is given by

$$\begin{aligned} \frac{df}{f} &= \frac{-\alpha}{2}\frac{d\sigma_2}{d\sigma_2(T=0K)} \\ &= \frac{-\alpha}{2}\frac{\sigma_2 - \sigma_2(T=0K)}{\sigma_2(T=0K)} \end{aligned} \tag{5.1}$$

Using equation 2.38 for n_{qp} and σ_2 from the approximate Mattis Bardeen equation (equation 2.20), both equations are re-written so that only T is an independent variable, $\xi = \hbar\omega/2k_bT$ and $\chi = \Delta_0/k_bT$. Thus, once both equations are substitute into equation 5.1, the resulting frequency response is given by

$$\begin{aligned}\frac{\Delta f_r}{f_r(T=0K)} &= -\frac{\alpha}{2}\frac{d\sigma_2}{\sigma_2(T=0K)} \\ &= -\alpha\left[\sqrt{\frac{2\pi}{\chi}}\exp(-\chi) + 2\exp(-\chi)\exp(-\xi)I_0(\xi)\right]\end{aligned} \tag{5.2}$$

where α is the kinetic inductance fraction.

To quantify the effect of adding lossy dielectrics to our resonators, the product of the fill factor and the TLS-induced loss tangent $F\delta_0$ must be considered [48, 47, 49].

$$\frac{\Delta f_r}{f_r(T=0K)} = -\frac{F}{2}\frac{\Delta\epsilon}{\epsilon}, \tag{5.3}$$

where ϵ is the dielectric constant parametrised as,

$$\frac{\Delta\epsilon}{\epsilon} = \frac{2\delta_0}{\pi}\left[\mathrm{Re}\Psi\left(\frac{1}{2}+\frac{\xi}{\pi i}\right) - \log_e\left(\frac{\xi}{2}\right)\right], \tag{5.4}$$

and Ψ is the complex di-gamma function.

The fill factor, F, is defined as the fraction of the resonator's total electrical energy stored in the TLS material. This is described by figure 5.2, where F is the sum of the electric field contained within the SiN_x, where TLSs are, to the sum of fields within the Silicon, where there are no TLSs.

Summing equations 5.2 and 5.4 together describe the total frequency response, allowing $F\delta_0$ to be extracted. A higher $F\delta_0$ is generally indicative of two-level systems, which lead to a reduction in resonator performance.

5.2 Device 1

Device 1 is a single-layer, dark array of 18 thin-film Aluminium (Al) LEKIDs, with varying SiN_x coverage. See section 4.2.1 for full details of the device, including the film thickness and the designed and measured resonant frequencies of each resonator. To investigate the impact of SiN_x on the performance of device 1, the dark response of the resonators presented in figure 4.2 was measured. The prototype device sits in a gold-plated OFHC copper sample box installed on the 80-mK baseplate of a cryostat, cooled via a miniature dilution system [82].

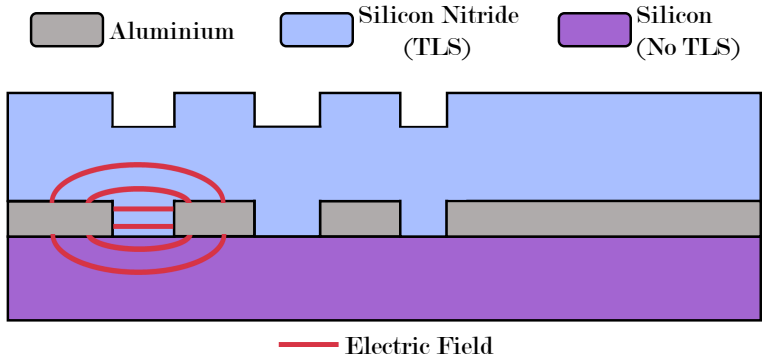

Figure 5.2: The fill factor is the fraction of the resonator's total electrical energy stored in the TLS material. In this diagram, it is the sum of electric fields contained within the TLS-filled silicon nitride to the the sum of the fields within the TLS-free silicon.

5.2.1 Experimental set-up

To investigate the response of resonators to temperature, each KID is driven at its optimal power and S_{21} is measured as the temperature of the base plate, on which the detectors sit, is varied. These are known as dark measurements and require the device holder to be light-tight to ensure detector response is purely due to temperature.

After cooling, the first set of measurements typically acquired is the S_{21} transmission of a detector array, as a function of readout frequency, to determine the resonant frequency of the KIDs. With the resonant frequencies measured for each detector, the next step is to determine the optimal drive power of each resonator. Resonators at several different readout drive powers are shown in figure 5.3. The optimal drive power is set by the bifurcation point of the resonator, which represents the power required to drive a resonator non-linear. Beyond the bifurcation point, the resonance is no longer Lorentzian in shape and is not adequately fitted by equation 2.61. Figure 5.3 shows S_{21} as a function of a variable attentuator which is used to vary to input power to the cryostat. Below 36 dB, close to the bifurcation point, the resonator starts to become distorted and is best fit using the method outlined by Swenson et al. [83]. In general, for device 1, the partially-covered and covered resonators had a higher optimum drive power than bare resonators.

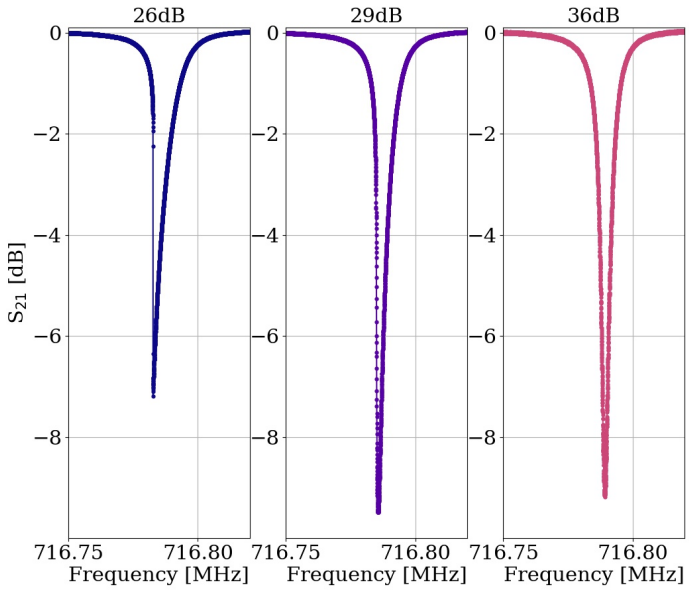

Figure 5.3: A few of examples of S_{21} transmission for a (a) very over-driven resonator beyond the bifurcation point, (b) a resonator just beyond the bifurcation point and (c) a ideally-driven KID before bifurcation.

5.2.2 Dark Response

As a first measure of detector performance, the fractional frequency shift of each resonator was investigated as a function of base temperature between 110 - 320 mK. S $_{21}$ of the resonators was measured using a VNA, and a resonant frequency was extracted following the procedure outlined in Khalil et al [84]. The resulting measurements of the S_{21} transmission converted into a fractional frequency response using equation 2.60 to compare the relative response of each detector.

The so-called back-bending typical of TLS perturbations, where the resonant frequency increases with temperature instead of decreasing, is observed in all detectors (see figures 5.4, 5.5 and 5.6) [48, 47]. Removing SiN_x from the capacitive region of the LEKID reduces back-bending substantially, however there is no discernible difference between the partially covered and bare resonator (figure 5.5 and figure 5.6). Overall this suggests the addition of SiN_x to the absorbing meander of the LEKID, where the electric field is relatively low, does not introduce a significant additional TLSs frequency response relative to the completely bare resonator.

To fully characterise the back-bending of the resonator, the combined model,

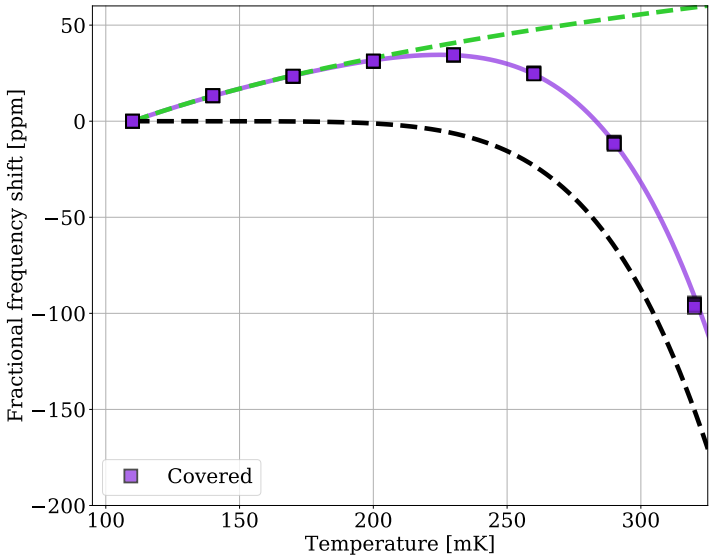

Figure 5.4: The fractional frequency shift as a function of temperature for the covered resonators. In this plot and figures 5.5 and 5.6, the dashed lines are the two different components to the fit of the data - the expected fractional frequency shift (dashed *black* line) and the additional shift caused by TLSs, calculated from equations 5.3 and 5.4 (dashed *green* line). The combined fit is a solid line.

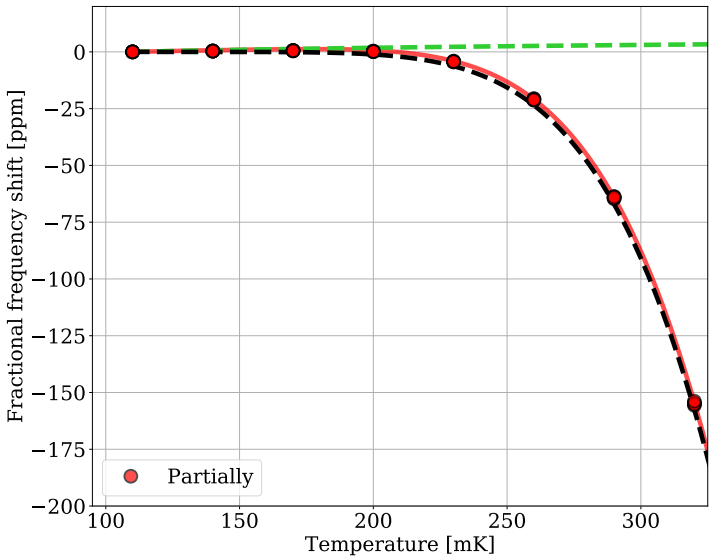

Figure 5.5: The fractional frequency shift as a function of temperature for the partially-covered resonators.

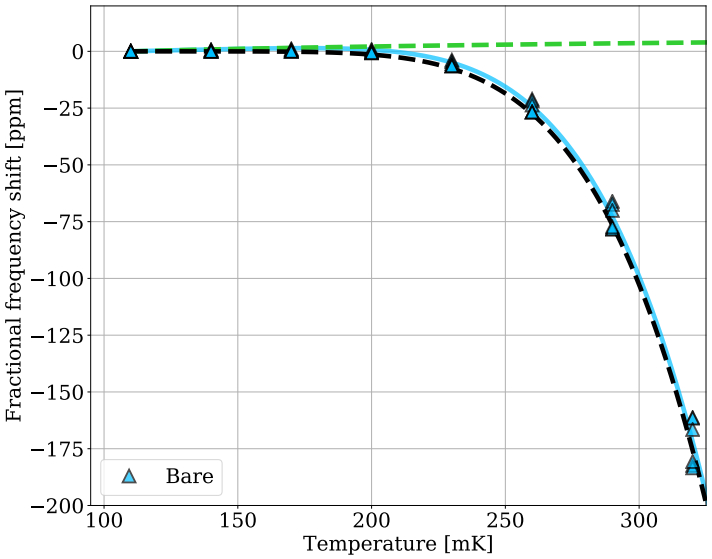

Figure 5.6: The fractional frequency shift as a function of temperature for the dielectric-free, bare resonators.

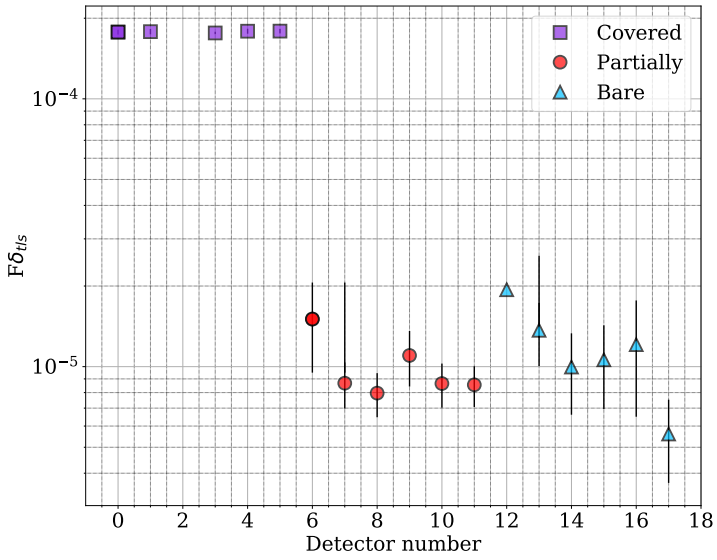

Figure 5.7: The product $F\delta_0$ extracted from fitting the fractional frequency response of each resonator, where the error bars indicate the error in fit. Here, covered resonators (detectors 0, 1, 3-5 as detector 2 did not yield) are purple squares, partially-covered resonators (detectors 6-11) are red circles and bare resonators (detectors 12-17) are blue triangles.

defined in section 5.1, is used to fit the frequency response of KIDs and separate the TLS component from the expected response as determined by Mattis-Bardeen superconductivity. The product $F\delta_0$, was extracted from the fits (solid lines in figures 5.4, 5.5 and 5.6. By removing the dielectric from the capacitive region of the LEKID $F\delta_0$, on average, was reduced from (1.78±0.02) x10^{-4} to (1.03±0.11) x10^{-5}. This equates to a reduction in $F\delta_0$ of $\sim$ 16 across the partially-covered and bare resonators of the prototype array. The average $F\delta_0$ was found to be (1.14±0.18) x10^{-5} for the bare resonators. It should be noted that the capacitor geometry for each LEKID is very similar, thus F should only vary slightly between detectors meaning this experiment provides good insight into the dielectric loss tangent.

The measured $F\delta_0$ is comparable to other experiments which measure the impact of dielectric materials on resonators [85]. For example, $F\delta_0$ has been measured to be: (i) 1.5-2.5x10^{-5} and (ii) 2.0-2.5x10^{-5} for Niobium inductively-coupled LEKIDs on a sapphire substrate, where the IDC is covered in (i) HfO_2 and (ii) Al_2O_3 [86]. Removing the dielectric resulted in a reduction in $F\delta_0$ between 5 - 10 times [86]. The lowest documented dielectric loss is $\sim 10^{-5}$, but has been measured in many different materials [85].

5.2.3 Dark Detector Noise

To characterise the noise of the detectors, and estimate the electrical noise equivalent power (NEP), we utilised the standard single-tone homodyne readout to measure the noise in resonant frequency, df0 from I and Q [6]. Timestreams of I and Q are measured equation 3.5 converts this complex S_{21} transmission of the resonator into df0. In python, the df0 timestream is converted into a power spectral density (PSD) measured in units of Hz^2/Hz [75]. To scale the spectrum, the PSD is divided by the square of the tone frequency (frequency of the LO), and the resulting fractional frequency noise is in units of 1/Hz.

The fractional frequency noise of a covered (purple), partially-covered (red) and bare (blue) resonator is shown in figure 5.8. Each spectrum is relatively flat at low frequencies, but the frequencies most impacted by TLS noise have not been explored here. Moreover, each resonator has the expected feature of a roll off due to the fundamental limit on how fast a detector can respond to fluctuations in resonance

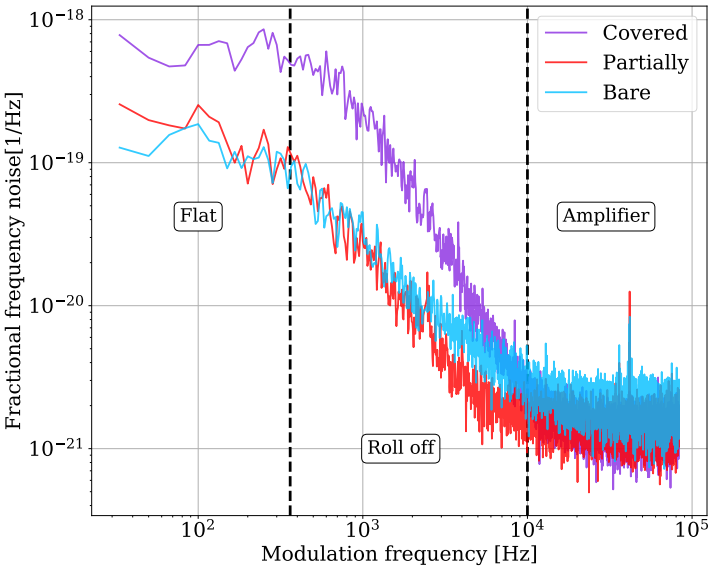

Figure 5.8: The measured noise power spectrum of a covered (purple), partially-covered (red) and bare (blue) resonator at 160 mK. The noise power spectrum is divided into three main components - the flatter part of the spectrum, the roll-off due to the quasi-particle lifetime and the amplifier noise.

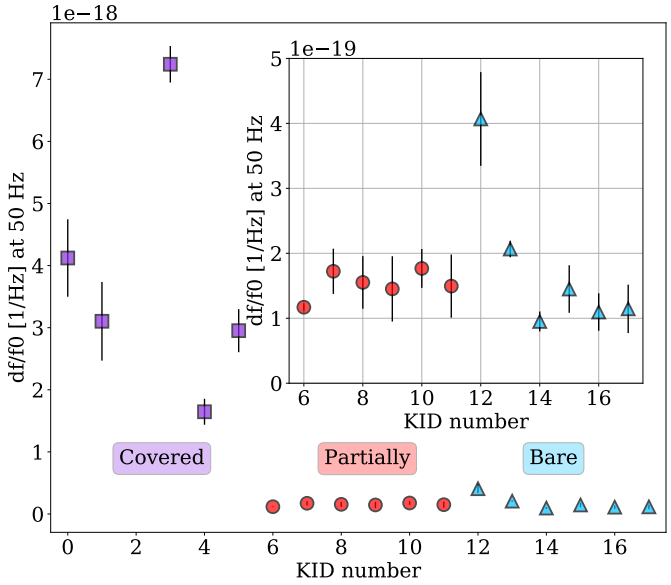

Figure 5.9: Measuring the fractional frequency noise at a modulation frequency of 50 Hz for covered (purple), partially-covered (red) and bare (blue) resonators at 80 mK. One covered resonator did not yield. The inset allows for a closer look at df/f_0 for the bare and partially-covered resonators.

- the quasi-particle lifetime of the resonator (see section 3.2.1). The high frequency part of the spectrum which is relatively flat, after the roll off, is due to the amplifier noise (see section 3.2.3). Due to the high Q-factor values of each resonator, which generally exceed 10^5, the detector noise is almost two orders of magnitude higher than the amplifier noise. This is because the detector is much more responsive to changes in frequency noise when the resonance curve is more narrow (i.e the Q factor is higher), and will therefore be much noisier than the amplifier. In figure 5.8, the covered resonator has the highest noise level, followed by the partially-covered resonator and the bare resonator.

In figure 5.9, the fractional frequency noise (df/f_0) is shown for each detector at a modulation frequency of 50 Hz to compare detector noise in the flat region of the noise power spectral density. Overall, the covered resonators had the highest noise level of all resonators with an average of (3.81±0.20) x10^{-18} Hz^{-1}, compared to the partially-covered at (1.53±0.16) x10^{-19} Hz^{-1} and the bare resonators at (1.80±0.17) x10^{-19} Hz^{-1}. Thus, the average noise power level is $\sim$ 25 times higher compared to the partially-covered resonator and $\sim$ 21 times higher than the bare resonator, which indicates adding the dielectric to the absorbing element of the detector does not result in excess noise being observed. Moreover, this suggests that noisier dielectric materials could be used with this detector architecture, but this requires testing of additional devices in the future.

5.2.4 Dark Noise Equivalent Power

It is possible to estimate the frequency responsivity of the detector, dx/dn_{qp}, from its fractional frequency response, by converting temperature into the quasi-particle density using equation 2.39 [79]. This is an important quantity which can be combined with measurements of the noise power spectral density to determine the dark (or electrical) noise equivalent power (NEP). The NEP is defined as the power required to produce a signal-to-noise ration (SNR) of 1 in 0.5 seconds of integration time (or a 1 Hz bandwidth).

By fitting to the linear response of the resonator to change in the number of quasi-particles as a function of base temperature, the frequency responsivity can be estimated. The frequency responsivity of the example covered, partially-covered

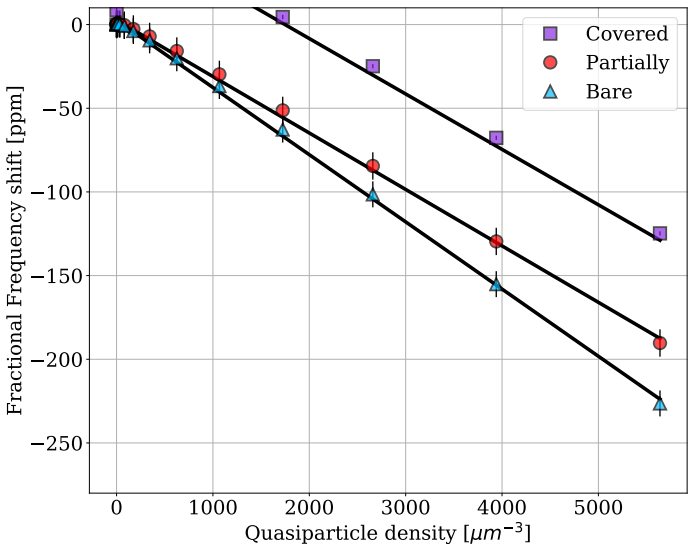

Figure 5.10: Estimating the frequency responsivity of example KIDs from the resonator response to the quasi-particle density as a function of base temperature. Only higher temperature data points are fitted due to the presence of back-bending. The error in extracted fit is shown.

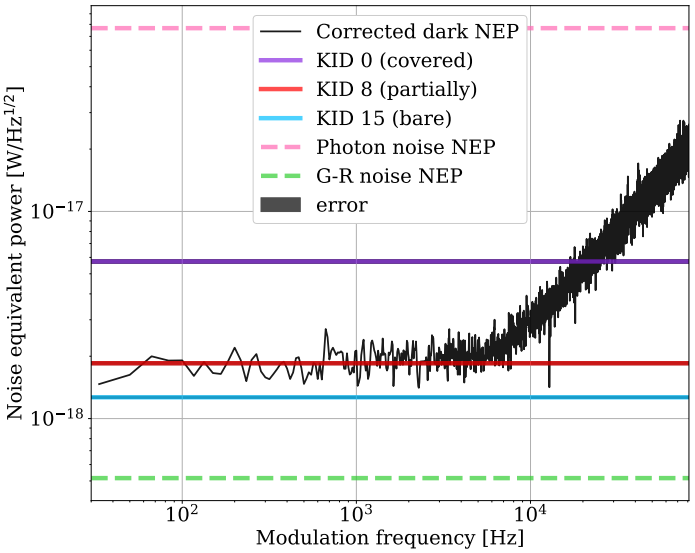

Figure 5.11: Dark noise equivalent power calculated (*black*) after the noise PSD of a partially-covered resonator was corrected for the quasi-particle roll off. The measured dark NEP for each resonator type are also shown here, alongside the predicted G-R (*green*) and photon noise NEP (*pink*).

and bare resonators are in figure 5.10. Here, dx/dn_{qp} is extracted from the gradient of the linear fit and is equal to (-3.31±0.03)x10^{-8} for the covered resonator, (-3.37±0.04)x10^{-8} for the partially-covered resonator and (-4.02±0.04)x10^{-8} for the bare resonator. Low temperature data points are excluded due to back-bending and the error shown here is the error in fit. This is only part of the total detector responsivity, which is given by

$$R_{det} = \frac{\eta \tau_{qp}}{\Delta_0 V_{tot}} \frac{dx}{dn_{qp}} \tag{5.5}$$

recall η is the pair-breaking efficiency, τ_{qp} is the quasi-particle lifetime, Δ_0 is the energy gap at 0 K and dx/dn_{qp} is the frequency responsivity. The NEP of the resonator is given by

$$NEP = \frac{\sqrt{S_N}}{R_{det}} \tag{5.6}$$

where S_N is fractional frequency noise PSD.

Thus, the dark NEP can be derived from fractional frequency noise PSD and detector responsivity calculated from the noise power spectral density (see figure 5.8), alongside known material parameters [87]. At 160 mK, the quasi-particle extracted from fitting the roll-off of the partially covered noise spectrum is 511 μs which is longer than the resonator ring-down time of 52 μs. The resulting NEP, corrected for roll off, is shown in figure 5.11 for the partially-covered resonator 8, alongside the NEP calculated for resonators 0 and 15. The NEP values are (5.73±0.12)x10^{-18} WHz$^{-1/2}$ for the covered resonator (KID 0), (1.85±0.03)x10^{-18} WHz$^{-1/2}$ for the partially-covered resonator (KID 8) and (1.28±0.02)x10^{-18} WHz$^{-1/2}$ for the bare resonator (KID 15). The associated NEP due to generation-recombination noise, the fundamental limit on a dark detector, is given by [87]

$$NEP_{GR} = \frac{2\Delta_0}{\eta} \sqrt{\frac{N_{qp}}{\tau_{qp}}} \tag{5.7}$$

As the detector volumes (V_T) are the same for each detector, 4768 μm^3, so is N_{qp} for each resonator at 160 mK. The expected NEP_{GR} for the partially-covered resonator is equal to 5.16x10^{-19} WHz$^{-1/2}$, and this is 3.6 times lower than the measured detector NEP. For the covered resonator, NEP_{GR} is 7.2 times higher than the measured NEP at 8.00x10^{-19} WHz$^{-1/2}$ and for the bare resonator, NEP_{GR} is 2.19 times higher than the measured NEP at 5.84 x10^{-19} WHz$^{-1/2}$.

For a typical ground-based CMB experiment and for an optical array of detectors, the expected photon noise is the limiting noise contribution to detector NEP, which is given by the quadrature sum of two components - the wave and shot noise. The shot noise component is given by

$$e_{shot} = \sqrt{2hfP_{opt}} \tag{5.8}$$

and the approximate wave noise component is described by

$$e_{wave} = \frac{P_{opt}}{\sqrt{\Delta f}} \tag{5.9}$$

Thus, the total photon noise is equal to

$$NEP_{photon} = \sqrt{e_{wave}^2 + e_{shot}^2} = \sqrt{4hfP_{opt} + \frac{P_{opt}^2}{\Delta f}} \tag{5.10}$$

where P_{opt} is the optical power absorbed by the detector, Δf is the filter bandwidth and f is the frequency of incoming photons. For a single-moded antenna, P_{opt} can be estimated as

$$P_{opt} = k_b T \Delta f \tag{5.11}$$

For a sky temperature of 20 K, the peak CMB frequency of 150 GHZ with a filter bandwidth of 45 GHz, P_{opt} is 12.4 pW. The wave noise component is 5.85x10^{-17} WHz$^{-1/2}$ and the shot noise component is 4.97x10^{-17} WHz$^{-1/2}$, thus the total photon-noise NEP is 7.67x10^{-17} WHz$^{-1/2}$. Currently all of the resonators in figure 5.11 are below the photon-noise-limited NEP required for a typical CMB experiment.

To fully characterise the detector noise properties, it is important to measure the 1/f knee of the noise spectrum as this is indicative of TLSs. However, excessive system 1/f noise is currently prohibiting low-frequency measurements. Moreover, the system noise needs to generally be better calibrated to explore the differences between the expected NEP_{GR} and measured NEP of the detectors. Going forward, the noise of each detector must be measured simultaneously to allow for de-correlated noise analysis and to enable the exploration of low-frequency behaviour.

5.3 Summary

An amorphous material, like silicon nitride, must be deposited over the LEKID to form the microstrip required for optical coupling in a mc-LEKID. The dielectric

requirement of the microstrip is known to be problematic for detectors due to their susceptibility to TLSs which degrade detector performance.

However, it is possible to minimise additional TLS losses by physically separating the inductive and capacitive elements - a defining characteristic of a LEKID. In this chapter, the performance of a dark, single-layer LEKID array demonstrates that the dielectric requirements of the microstrip transmission line coupling can be met, whilst maintaining a minimal additional parasitic dielectric response and without creating additional noise. This is an important step towards the overall goal of an mc-LEKID, however it is not a completely accurate depiction because the groundplane of the microstrip is missing, and its addition will alter the KID performance.

6

On-chip filtering structures

With the dielectric requirements of the microstrip satisfied, without a notable loss in detector performance, the next step is to utilise the length of microstrip, between the antenna and detector, to define the band of frequencies which reach the detector. This is a crucial step towards realising multi-chroic pixels, a desirable property for future CMB detectors, which has already been implemented by some TES-based instruments [3, 4, 5].

The research presented in this chapter details the theory required to understand the fundamental principles of simple on-chip, in-line filtering structures. Preliminary results obtained from measuring the spectral performance of single-colour prototypes are also included and would not have been possible without the help of S. Rowe and P. Moseley. The detectors were designed and fabrication by P.S. Barry, but the on-chip filters were designed by the author of this thesis. The measurements of the microstrip properties were completed by C. Dunscombe and T. Brien.

6.1 Quarter-wave stub filter

In microwave applications, resonant stubs are utilised to modify the impedance of a microstrip transmission line at a given frequency to create a notch filter [**MicrowaveWiley**]. Current CMB experiments, such as ACTPol and POLARBEAR utilised on-chip filters composed of resonant stubs to ensure only the frequencies of interest reach their detectors [3, 4, 5]. For filters of this design the quarter wavelength condition, when the length of the stub $l = \lambda_c/4$, underpins their operation.

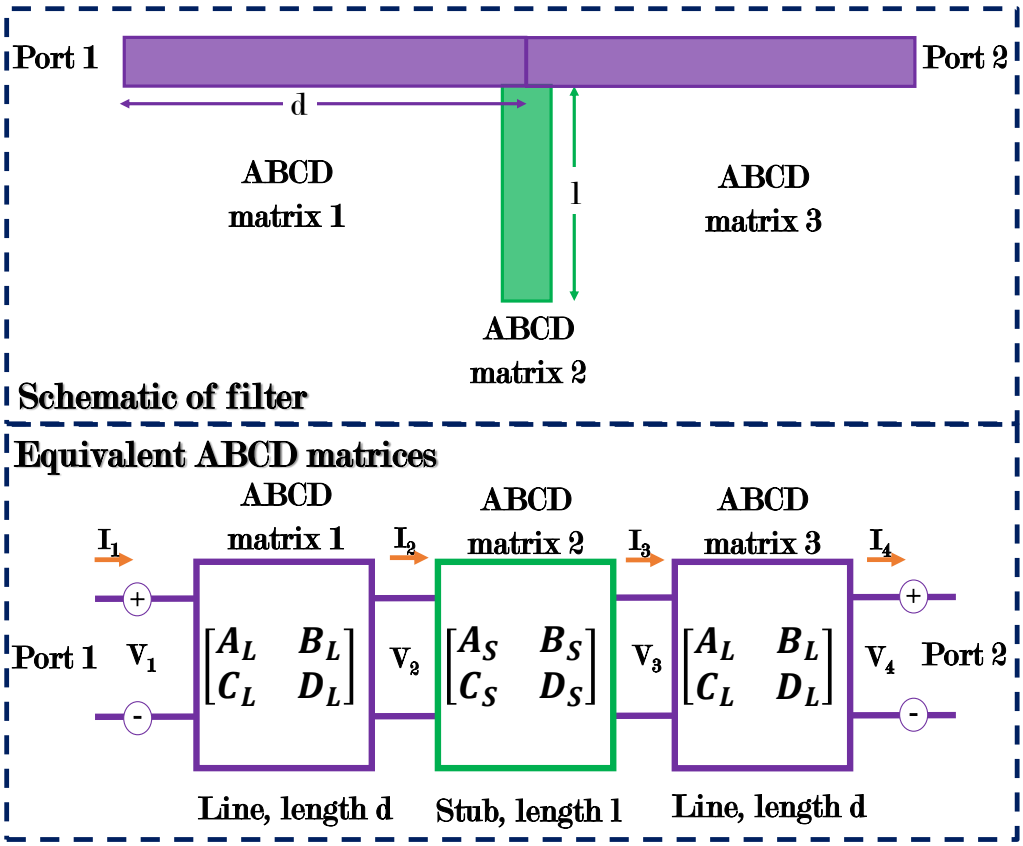

Figure 6.1: Schematic of a single-stub filter (upper) and cascading three ABCD matrices to simulate the equivalent single-stub filter (lower).

The impact of adding a resonant stub on the impedance of the original transmission line is dependent on two key lengths: the length of the stub, l, and the distance to neighbouring stubs, d [41]. Generally both of these lengths should be equal to $\lambda_c/4$ where λ_c is the wavelength at which the impedance of the structure should be equal to Z_0. The exception to this relationship is the case of a one stub, two port system where the impedance is only dependant on the length of the stub that

can be placed anywhere along the transmission line. This is depicted by a purple transmission line and green filtering stub in figure 6.1.

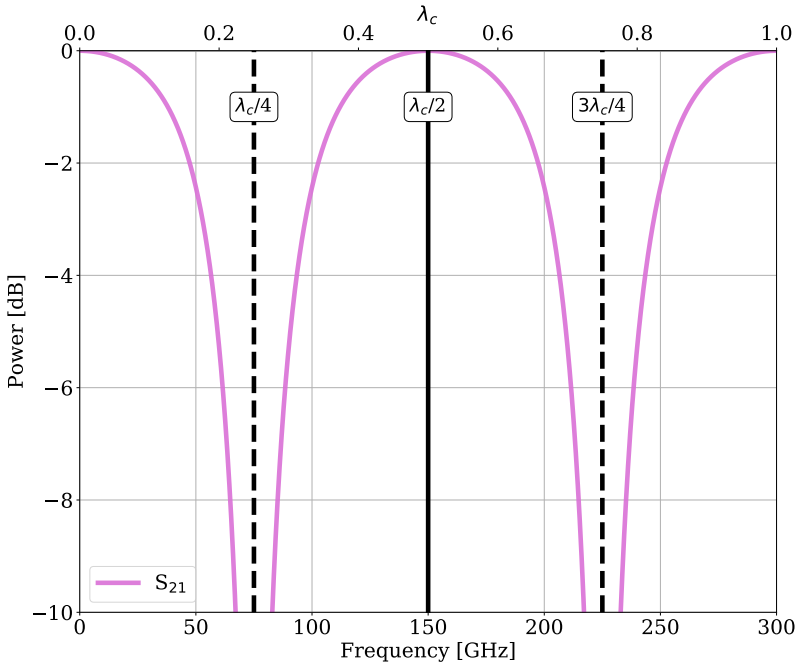

Figure 6.2: The S_{21} transmission of a one-stub filter with a λ_c of 2mm (= 150 GHz). The ABCD matrices presented in the next section (section 6.1.1) have been utilised to simulate S_{21}.

For the case of a one-stub filter, as depicted in figure 6.1, the resonant stub modifies the impedance around the resonance of $\lambda_c/4$, resulting in a resonant feature in the S_{21} transmission of the system. As the wave travels from port 1 to port 2 and down a quarter wavelength stub, it will be reflected at the end of the quarter wavelength stub. Reflection at the open end reflects in phase to the incident wave forcing the voltage to be zero at the point where the stub connects to the line, hence the stub looks like a short on the line at the quarter-wave condition [**MicrowaveWiley**]. Overall, this translates to zero impedance at the stub-microstrip connection which means the signal will not continue to travel towards port 2. Thus, the $\lambda_c/4$ results in a band-stop notch filter in the S_{21} transmission. To create a band-pass filter utilises the $\lambda_c/2$ condition instead, creating an anti-resonance which results in the open stub behaving as an open circuit, allowing the signal to flow from port 1 to port 2. By $3\lambda_c/4$, the open stub behaves once more as a short-circuit resulting in a notch filter in the S_{21}. An example of S_{21} as a function of frequency and λ_c for a single-stub,

band-pass filter tuned to 150 GHz is shown in figure 6.2. Here, S_{21} is a maximum at $\lambda_c/2$, and a minimum at $\lambda_c/4$ and $3\lambda_c/4$. S_{21} in figure 6.2 was calculated using the ABCD matrices presented in the next section.

6.1.1 ABCD Matrices

ABCD matrices are employed to predict the behaviour of microwave networks. Different ABCD matrices representing individual network elements, such as a length of transmission line or a filter stub, can then be cascaded in order to evaluate the scattering parameters of a more complicated microwave network, such as a band-pass filter [**MicrowaveWiley**, 41].

The ABCD parameters for a resonant stub of impedance Z_0, with a stub of length l, are defined as A_S, B_S, C_S and D_S [41]. This is the central matrix, matrix 2, taken from Figure 6.1.

$$\begin{bmatrix} V_1 \\ I_1 \end{bmatrix} = \begin{bmatrix} A_S & B_S \\ C_S & D_S \end{bmatrix} \begin{bmatrix} V_2 \\ -I_2 \end{bmatrix} = \begin{bmatrix} 1 & 0 \\ \frac{j\tan\beta l}{Z_0} & 1 \end{bmatrix} \begin{bmatrix} V_2 \\ -I_2 \end{bmatrix} \tag{6.1}$$

where ϵ_r has its usual definition as the relative permittivity, and

$$\beta = \frac{2\pi}{\lambda}\sqrt{\epsilon_r} \tag{6.2}$$

The ABCD parameters for a microstrip transmission line of length d is also required to determine the scattering parameters of a filter, and are defined as A_L, B_L, C_L and D_L [**MicrowaveWiley**]. This is matrix 1 and 3 of figure 6.1.

$$\begin{bmatrix} V_1 \\ I_1 \end{bmatrix} = \begin{bmatrix} A_L & B_L \\ C_L & D_L \end{bmatrix} \begin{bmatrix} V_2 \\ -I_2 \end{bmatrix} = \begin{bmatrix} \cos\beta d & jZ_o\sin\beta d \\ \frac{j\sin\beta d}{Z_o} & \cos\beta d \end{bmatrix} \begin{bmatrix} V_2 \\ -I_2 \end{bmatrix} \tag{6.3}$$

The resulting ABCD matrix for a one-stub filter is the product of the ABCD matrices from equations 6.3 and equation 6.1, where the ABCD parameters are defined as A_f, B_f, C_f and D_f. This matrix characterises the full one-stub filter system.

$$\begin{bmatrix} V_1 \\ I_1 \end{bmatrix} = \begin{bmatrix} A_f & B_f \\ C_f & D_f \end{bmatrix} \begin{bmatrix} V_2 \\ -I_2 \end{bmatrix} \tag{6.4}$$

where A_f, B_f, C_f and D_f are defined below:

$$A_f = (A_L A_S + B_L C_S)\, A_L + (A_L B_S + B_L D_S)\, C_L \tag{6.5}$$

$$B_f = (A_L A_S + B_L C_S)\, B_L + (A_L B_S + B_L D_S)\, D_L \tag{6.6}$$

$$C_f = (C_L A_S + D_L C_S)\, A_L + (C_L B_S + D_L D_S)\, C_L \tag{6.7}$$

$$D_f = (C_L A_S + D_L C_S)\, B_L + (C_L B_S + D_L D_S)\, D_L \tag{6.8}$$

It is clear from equation 6.4 that using ABCD matrices to calculate the impact of adding resonant stubs to transmission lines soon results in very large matrices. To determine the transmission and reflection of the overall filter network, S_{21} and S_{11} must be calculated. In general, they are given by **[MicrowaveWiley]**

$$S_{21} = \frac{2}{A + (B/Z_0) + CZ_0 + D} \tag{6.9}$$

and

$$S_{11} = \frac{A + (B/Z_0) - CZ_0 - D}{A + (B/Z_0) + CZ_0 + D} \tag{6.10}$$

where Z_0 is the characteristic impedance of the ports. To determine the transmission and reflection of the single-stub filter, the ABCD parameters calculated in equation 6.4 are substituted into the ABCD parameters in equations 6.9 and 6.10, such that: $A_f = A$, $B_f = B$, $C_f = C$, $D_f = D$.

6.1.2 Designing a quarter-wave stub

To design the in-line filter for the detectors, the software Advanced Design System (ADS) is utilised to define the filtering system comprised of ideal transmission lines. An ADS simulation is shown in figure 6.3. ADS is a key piece of analytical design and simulation software used for RF, microwave, and high speed digital applications, which relies on cascading ABCD matrices to determine the impact of each element on the overall transmission of the RF system.

ADS has built in optimisation features which will be implemented in order to specify how the system being simulated performs, with inputs to the optimisation routine including continuous variable, goals, maximum number of iterations and optimisation routine. For each property of a component, a range over which the value can be adjusted can be specified and ADS will adjust these to reach the

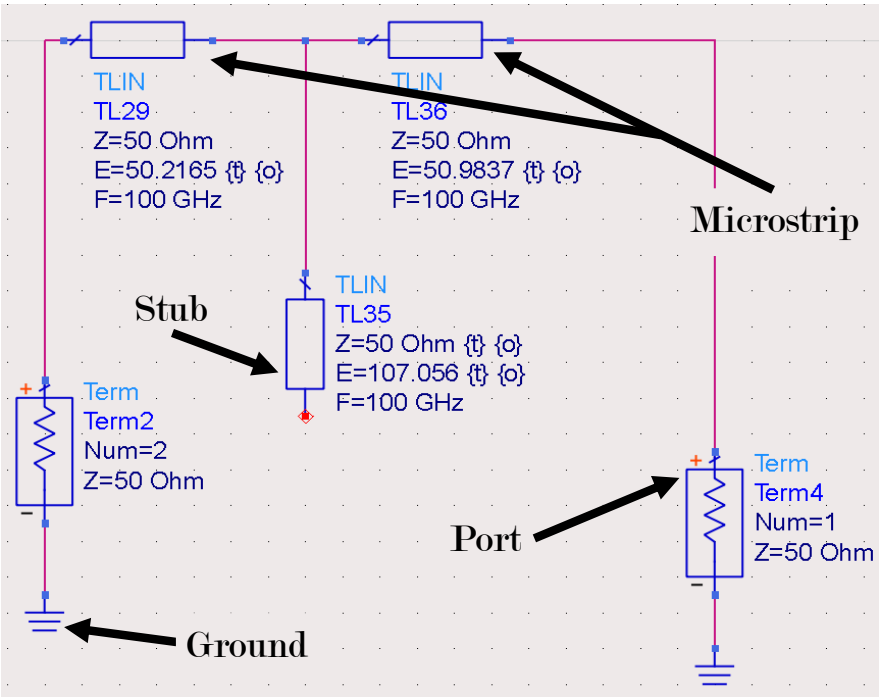

Figure 6.3: Advanced Design System screenshot of a one-stub filter system, complete with two ports and three sections of idealised transmission line, where the central piece of line represents the quarter-wave stub.

Example microstrip parameters	
Microstrip width [μm]	9
SiN_x thickness [nm]	500
Niobium thickness [nm]	250
Kinetic inductance [pH/$\square$]	0.10
Microstrip length [μm]	150

Table 6.1: Physical and material parameters for an example microstrip

specified goals quantified by a set of inequalities. Each goal can also be weighted to help ADS to prioritise certain goals over others. An example of a goal is that the magnitude of the scattering parameter S_{21} must be greater than 0.95 whilst in the frequency range of 130 - 160 GHz.

For a fixed impedance, which fixes the width of the transmission line, and a variety of goals for the value of S_{21} as a function of frequency, ADS will determine the two parameters required for filter design - the optimal electrical length, in degrees (where 360° of electrical length = 1λ in metres), of each resonating stub and the separation between neighbouring stubs. This is equivalent to lengths l and d defined in figure 6.1, but requires a conversion factor to switch from degrees to metres to make a physical device.

A notable benefit of optimising a system in ADS is that no information about the material is required for the optimisation features or the simulation. Meaning that once designed, it could theoretically be made using a wide variety of materials, as long as a new conversion factor is calculated. Overall, this method of filter design produces very flexible designs which is why it is implemented over defining the properties of the microstrip line in ADS.

To realise the filter design in Sonnet, the optimal electrical lengths from ADS needs to be converted into physical dimensions. Sonnet is used to create a microstrip transmission line based on the intended design parameters, including the thickness of our dielectric SiN_x and the width of the niobium transmission line; and determine the phase of a 150 GHz signal along it. An example of this is shown in figure 6.4. In general, Sonnet approximates each metallic layer as a zero-thickness, two-dimensional sheet where its properties are defined in terms of kinetic inductance. Thus, the real device profile which may include properties which arises during the fabrication process, such as sloping sides, are not taken into account. However for the devices measured here, the superconducting line widths are much greater than the thickness and the dielectric layer is modelled and fabricated as a continuous sheet. Hence any edge effects are considered negligible.

The electrical length of a circuit element calculated in ADS is converted to a physical length of microstrip in Sonnet. A microstrip and filter drawn into Sonnet are shown in figure 6.5. Here, we design the width of our microstrip line with a given

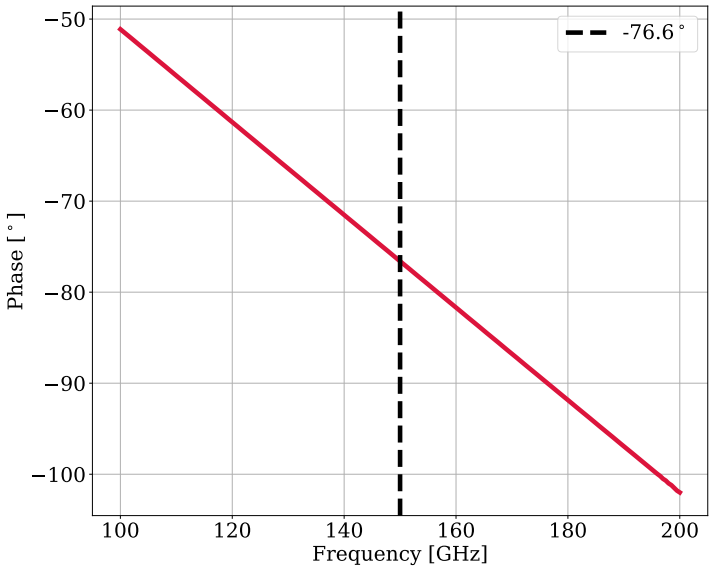

Figure 6.4: Simulating the phase of a 150-μm length of microstrip transmission designed with the parameters in table 6.1 to determine the conversion between physical and electrical length required to translate ADS designs to Sonnet.

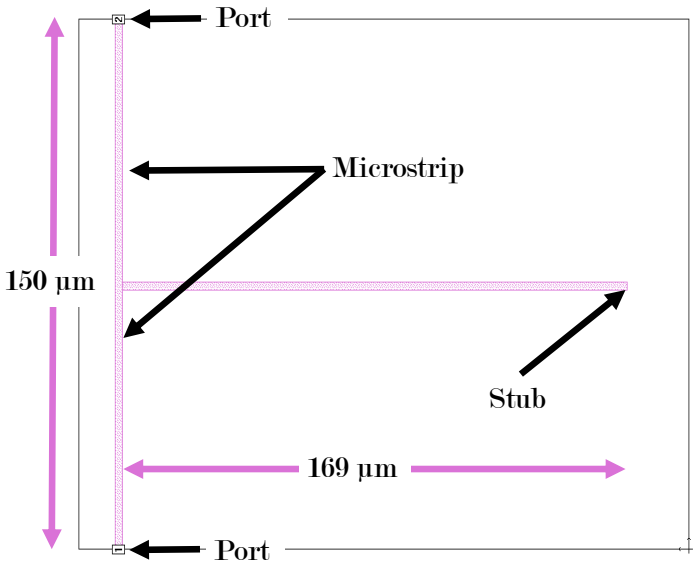

Figure 6.5: Sonnet screenshot of a one-stub filter system, complete with two ports and three sections of idealised transmission line, where the central piece of line represents the quarter-wave stub. This is converted filter designed originally in ADS, as shown in Figure 6.3.

dielectric thickness and relative permittivity as well as a kinetic inductance to match the impedance used in ADS. Once this is completed, the relationship between the physical and electrical length can be calculated from the phase simulated shift in S_{21} for a given line length. This phase shift now accounts for both the effects of kinetic inductance as well as fringe fields in the microstrip. For an example transmission line, where the parameters are highlighted in table 6.1 this translates to 1.95 μm per degree.

6.1.3 Comparison of simulations

In section 6.1.1, the ABCD matrix was introduced to enable simulation of a resonant stub connected to two pieces of transmission line to form a single-stub, band-pass filter. The reflection and transmission of the filter, S_{11} and S_{21}, can be calculated using equations 6.10 and 6.9 and compared to those determined from both ADS and Sonnet simulations to investigate whether the models are in good agreement.

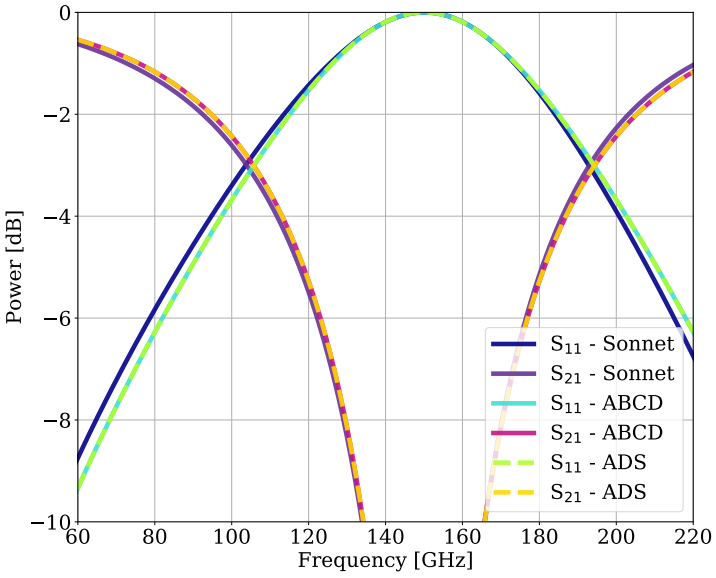

Figure 6.6: Comparing the transmission, S_{21}, and reflection, S_{11} of a single-stub, band-stop filter at 150 GHz simulated using the ABCD matrices defined in equation 6.4, ADS and Sonnet.

There are clear discrepancies between the Sonnet model and idealised ADS and ABCD matrices models in figure 6.6, but they are mostly in good agreement. The

difference comes about due to effects which arise in the calculations by Sonnet, but not the analytical ADS and ABCD matrices models. These could be radiation losses in the resonant stubs and electromagnetic cross coupling between stubs and the line or ground plane in Sonnet. However, figure 6.6 demonstrates it is possible to quickly optimise the filter design in ADS, transfer the design to Sonnet whilst keeping the design to specification.

6.2 Designing multi-pole band-pass filters

With the principles of microwave filter design understood, the next step is to design a filter with future CMB experiments in mind. Typical frequencies to target for making observations of the CMB span a large range, from 10 - 1000 GHz, but are typically more concentrated around the 90 - 350 GHz regime encapsulating the peak frequencies of the CMB [88]. For this research project, a broad-band and narrow-band filter, centred at 140 GHz, close to the mid-frequency at the peak frequency of the CMB, 150 GHz, was designed. This is the central frequency of the optical power source available for filter measurements.

6.2.1 Broad-band filter

With a target frequency of around 140 GHz selected, the next parameters to determine are (i) the number of resonating stubs used to define the filter profile and (ii) the filter bandwidth, as measured by the full width at half maximum of the filter profile. For the broad-band filter, five resonating stubs were selected to ensure good control over the shape of the pass band, without increasing the complexity of the design. This also mimics previous implementations of multi-chroic pixels based upon TESs [38, 5]. Moreover, a target bandwidth of 30 GHz was selected for the broad-band filter.

The system becomes more complicated for multi-pole filter because if there are multiple stubs along a transmission line, the distance between the stubs will affect the impedance and will need to meet the $\lambda_c/2$ condition for a frequency to be transmitted. However the same design process for a single-stub filter, starting with optimisation in ADS before translation to Sonnet, can still be utilised to design a

filter.

Following the methodology outline in section 6.1.2, a filter was designed in ADS with five transmission line segments representing five filtering stubs, with six segments forming the main transmission line connected to two ports. Once optimised, the design is converted from ADS to Sonnet using the a conversion factor between physical and electrical length calculated from the phase along the transmission line.

The resulting frequency characteristics for both ADS and Sonnet simulations are shown in figure 6.7 and they are both in good agreement. The most notable differences between ADS and Sonnet is the small dip in the main pass-band of 3 % in Sonnet for the broad-band filter and the lower frequency edge being marginally higher in Sonnet. Neither of these differences will have a huge impact on the overall design, and originate from Sonnet being a full 2D electromagnetic simulation. The designed band-width, defined by the half-power point, of the broad-band filter is 29.4 GHz centred at 144 GHz.

It should be noted that there was an error in the original Sonnet simulations of filters, therefore the ADS simulation has been corrected to reflect the changes. Unfortunately this means the shape of the broad-band filter has an unwanted dip at 128 GHz, but this is an accurate simulation of the fabricated filters, rather than a poorly designed filter. This is something that could be fixed in future designs.

6.2.2 Narrow-band filter

With a broad-band filter successfully designed, a second filter was also designed with smaller range of frequencies - a narrow-band filter. The motivation behind designing an additional filter is to test how robust the design process is and to emphasise any fabrication issues that become apparent once the filter is realised. In line with the previous filter design, five resonating stubs will be added to a length of transmission line to form the narrow-band filter, with a target bandwidth of 4 GHz.

Following the methodology outline in section 6.1.2 and for the broad-band filter, five transmission line segments representing five filtering stubs, with six segments forming the main transmission line connected to two ports were created in ADS to form a filter. Once optimised, the design is converted from ADS to Sonnet using the degrees to length conversion factor calculated from the phase along the transmission

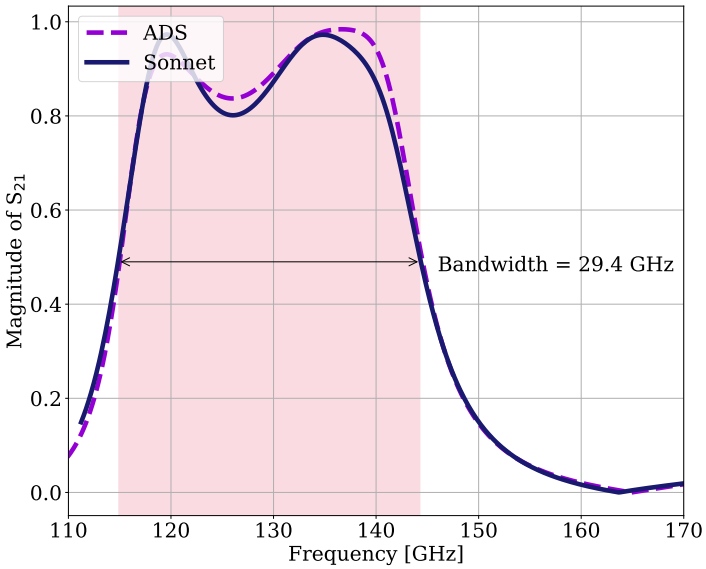

Figure 6.7: Frequency characteristics of the broad-band, band-pass filter from simulations created in ADS (purple dashed line) and Sonnet (solid blue line). The bandwidth defined here is the width of the filter band at half power and is 29.4 GHz for the broad-band filter.

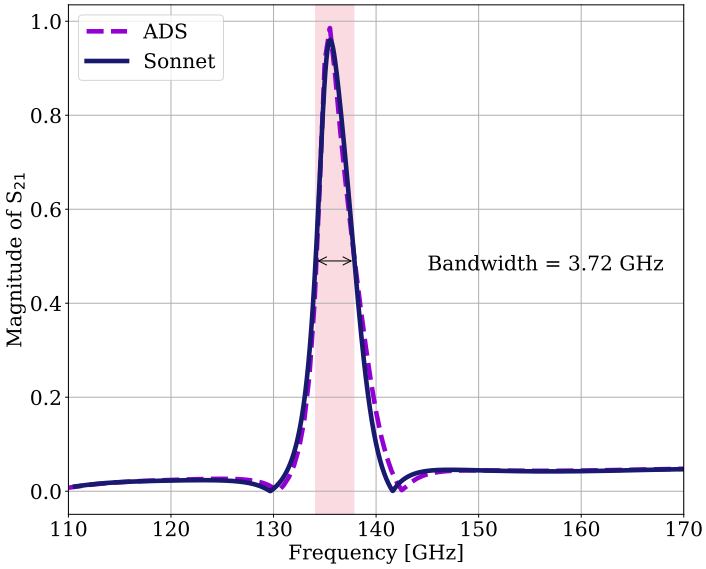

Figure 6.8: Frequency characteristics of the narrow-band, band-pass filter from simulations created in ADS (purple dashed line) and Sonnet (solid blue line). The bandwidth defined here is the width of the filter band at half power and is 3.79 GHz for the narrow-band filter.

line.

The resulting frequency characteristics for both ADS and Sonnet simulations are shown in Fig. 6.8 and they are both in good agreement. The most notable difference between ADS and Sonnet is the peak frequency being marginally lower in Sonnet for the narrow-band filter. By design, the intended bandwidth of the narrow-band filter is 4 GHz.

6.3 Spectral response

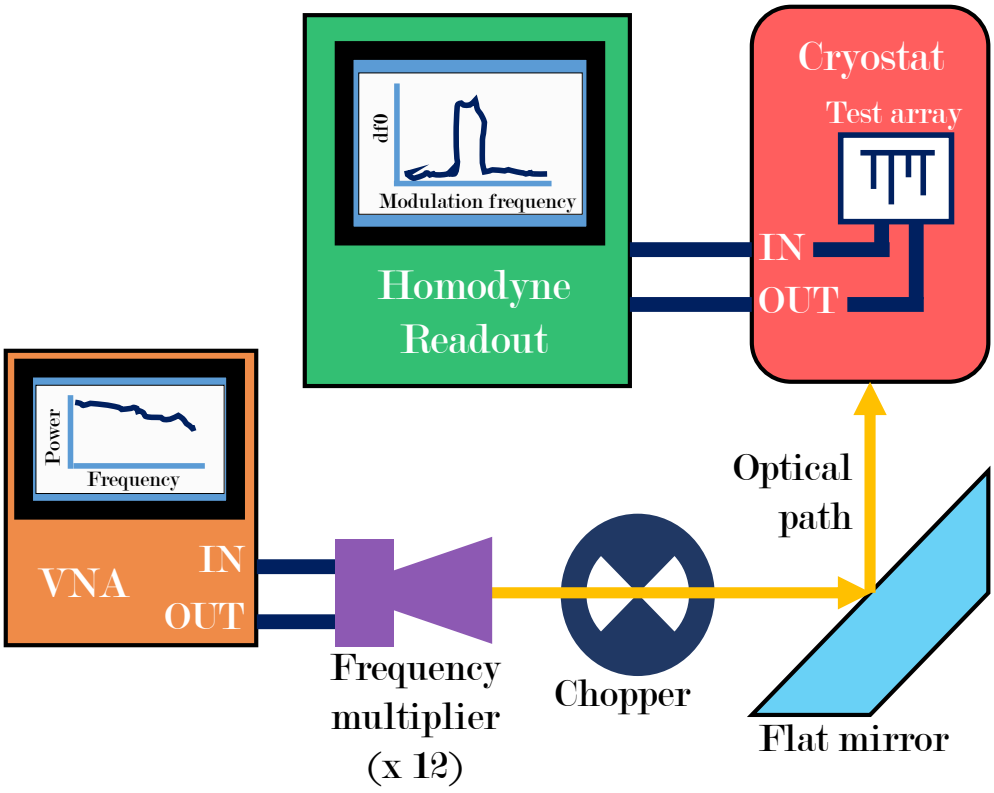

Figure 6.9: The experimental set-up required to measure the transmission profile of the on-chip filters coupled to KIDs. The VNA is used as an optical power source, with the frequency multiplier used to output frequencies between 110 - 170 GHz. The signal is chopped at 20 Hz, thus appears as a signal at 20 Hz in the frequency response of the resonator, df_0, when monitored using the homodyne readout electronics described in figure 4.1.

To determine the optical response of the filters, the on-chip filters were incorporated into an array of detectors known as device 2 and an experiment was designed to measure the filter profiles. It should be noted that this is not an ideal set-up, and instead was designed to quickly establish any sign of filter function. For more details on the detector geometry, device layers, alongside the predicted and measured resonant frequencies, see chapter 4, section 4.3.1. The blackbody and optical response of the detectors from device 2 are presented in the next chapter, chapter 7.

As indicated by the diagram of the experimental set-up in figure 6.9, the sample was placed inside a cryostat with a base temperature of 300 mK when optically open to the room and with a metal-mesh, 5.9 cm^{-1} LPE filter to limit detector loading above 177 GHz. To create a source of radiation, the VNA was combined with a 12x frequency multiplier head resulting in radiating frequencies 110 - 170 GHz.

In order to monitor the on-chip filter response to the frequencies outputted by the VNA frequency multiplier head, the signal was modulated at 20 Hz using an optical chopper and any changes in the resonant frequency noise of the detectors must be monitored about this modulation frequency. Modulating the signal ensures the only signals being detected by the KIDs are the signals being output by the VNA. This helps avoid measuring fluctuations in resonant frequency which occur due to temperature fluctuations within the cryostat or changes in the lab environment.

To monitor changes in the resonant frequency, df_0, timestreams of the complex detector output S_{21} were measured as a function of VNA frequency and converted into changes into resonator f_0. Then, a Fourier transform of df_0 was summed in a narrow window about the 20 Hz modulation frequency to determine the spectrum of each filter, while rejecting noise at frequencies outside of the frequency of the chopper. Moreover, it is possible to gain insight into the pass band of the antenna by monitoring detectors not coupled to filters.

6.3.1 No filter

The measured raw data is shown in grey in figure 6.10, and the smoothed data, in red, is the raw spectrum smoothed by convolution with a low pass cosine filter. This is to help identify spectral features in the noisy, raw data. The raw and filtered

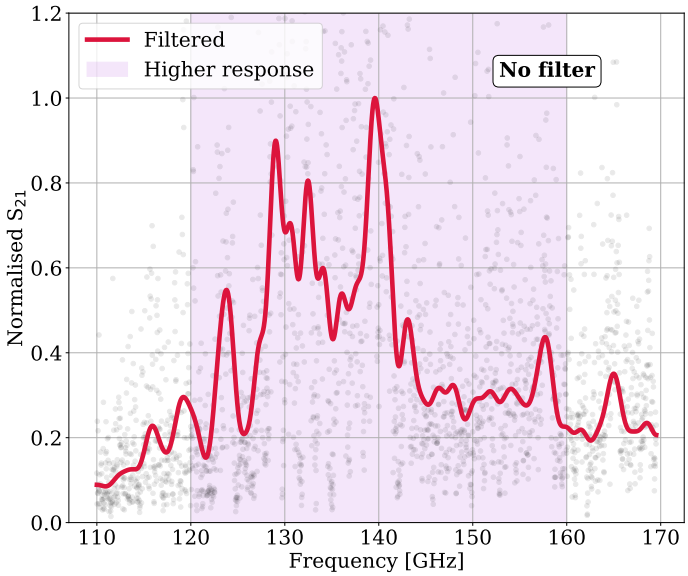

Figure 6.10: The spectral response of the filter-less LEKID, thus this is indicative of the antenna response. The raw data is in grey, and the smoothed, filtered data is the red solid line.

data have been normalised using the maximum of the filtered response. Overall, the smoothed response of the measured profile in figure 6.10 indicates a broad antenna response, with a higher response in the region centred near 130 GHz with an $\sim$ bandwidth of 40 GHz.

6.3.2 Broad-band filter

With an approximate idea of what frequencies were reaching optically-coupled detectors, the next detector to investigate is one connected to a filter. Starting with the broad-band filter with an designed bandwidth of 30 GHz centred at 130 GHz. Utilising the same method as before, the raw data was collecting via using a VNA head as a source of radiation, a chopper and monitoring the resonant frequency of detectors at around 20 Hz.

Comparing the smoothed spectrum of the broad-band filter in figure 6.11 to the antenna profile in figure 6.10 suggests some form of filtering has occurred, but the profile is interesting. Instead of one pass band, a main pass band and two neighbouring, but smaller bands have formed.

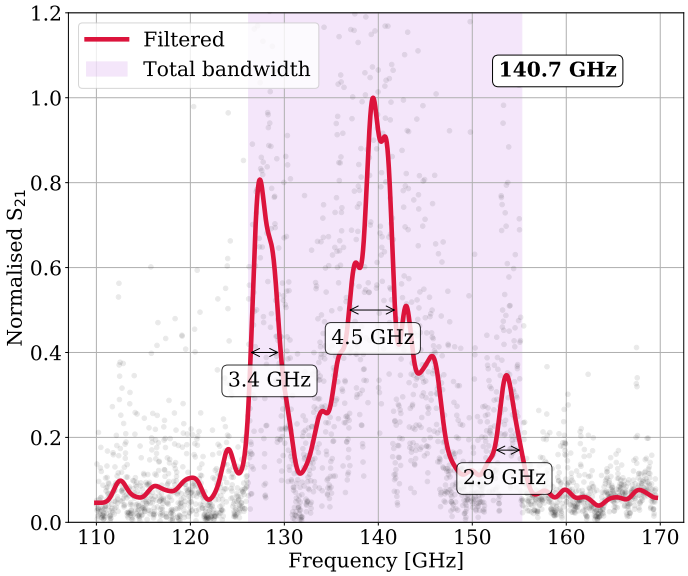

Figure 6.11: Spectral response of the detector with a broad-band filter. The data is plotted grey points which represent the raw data, whereas the red solid line is the filtered response which has been smoothed using a low pass filter.

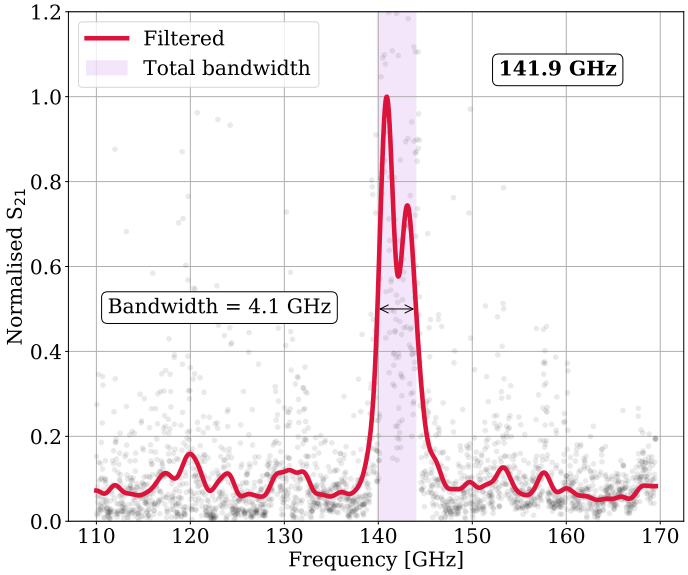

Figure 6.12: Spectral response of the detector with a narrow-band filter with an overall bandwidth is 4.1 GHz. The grey points represent the raw data, whereas the red solid line is the filtered response which has been smoothed using a low pass filter.

Moving from low frequency to high and considering the FWHM of each peak to determine the bandwidth from figure 6.11, the first peak has a bandwidth of around 3.4 GHz centred at 127.9 GHz; the central pass band has a bandwidth of around 4.5 GHz with a central frequency of 139.6 GHz, and the third peak has a bandwidth of 2.9 GHz centred at 153.8 GHz.

With so many features within the broad-band filter profile, it is tricky to estimate the total bandwidth without further modelling. From using the low- and high-pass edges of the outer peaks, a upper estimate can be determined and this sets the total bandwidth to $\sim$ 29.1 GHz centred at 140.7 GHz. The total bandwidth is represented by the shaded pink region in figure 6.11.

6.3.3 Narrow-band filter

Next the narrow-band filter was measured and the spectrum obtained is shown in figure 6.12, with the raw data as grey points and the data smooth via a low pass filter as a solid red line. Comparing figures 6.12 and 6.10 further indicates that the filter is working, as here the filter has clearly rejected the out-of-band antenna response, reducing the signal level to $\sim$ 10% of the peak filter response.

Smoothing the data in figure 6.12 revealed several features, a peak located at 140.8 GHz, a dip located at 142.1 GHz and a second, lower peak at 143.0 GHz. Including all of these features as the total filter profile determined a central of 141.9 GHz for the narrow-band filter with a bandwidth of 4.1 GHz which, although at the incorrect frequency, suggested a signal had been measured which resembled the narrow-band filter.

6.4 Comparing the results with simulations

The spectral results, when compared to a filter-less detector, suggest the on-chip, in-line filters are limited the frequencies reaching the detectors but are not to the intended specification. For example, both the broad- and narrow-band filters are centred below 140 GHz. This is likely an due to differences between intended and actual microstrip parameters once fabricated, including differences in dielectric thickness and kinetic inductance. To investigate these differences, a combination of measure-

ments and additional Sonnet simulations are required. This investigation focuses on the narrow-band filter because it has a bandwidth close to the predicted bandwidth with fewer additional features in the profile.

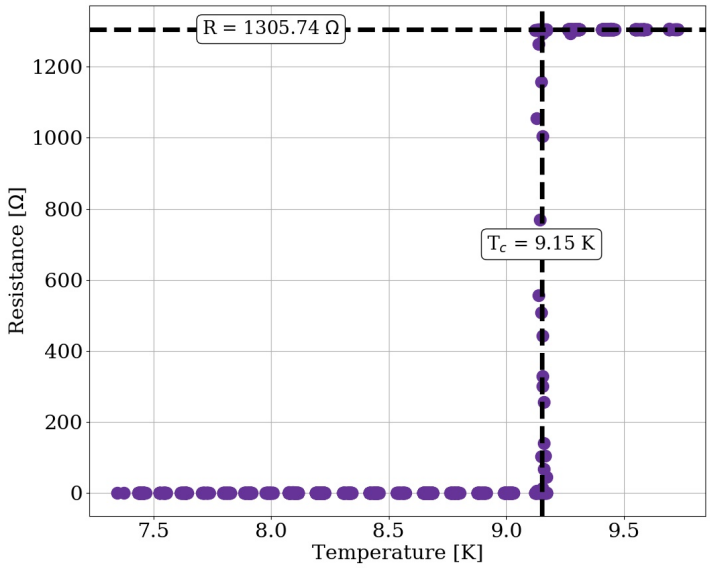

Figure 6.13: Resistance as a function of temperature for niobium as it transitions through its critical temperature. Here, T_c was measured to be 9.15 K and the normal-state resistance was 1305.74 Ω.

To estimate the kinetic inductance of the film, the physical dimensions of the devices were measured using a dektak profilometer. The thickness of the niobium and dielectric were measured from the variation in vertical profile across the feedline. Measurements indicate the dielectric, SiN_x, is 550 nm and with 260-nm thick layer of niobium. Next, the resistance of the feedline was measured as a function of temperature to determine the transition temperature, T_c, of the niobium and the normal-state conductivity, σ_n. This is shown in figure 6.13 and resulted in a T_c of 9.15 K and a normal-state resistance, R_n of 1305.74 Ω. The feedline on device 2 is $\sim$ 67 mm long, 16 μm wide is 260 nm thick. Thus, the normal resistivity, ρ, of niobium is given by

$$\rho = \frac{R_n A}{l} = \frac{1}{\sigma_n} \tag{6.11}$$

where R_n is the normal-state resistance, A is cross-sectional area of the feedline which is product of its width and thickness and l is its length. For the feedline

in question, the resistivity is 8.11x10^{-8} Ω/m. The normal conductivity of niobium, σ_n, can be calculated from the inverse of its resistivity and it was found to be 1.23x10^7 S/m. Combining σ_n with values of conductivity determined from Mattis-Bardeen conductivity, presented in chapter 2 to determine the kinetic inductance for the film. For a 260-nm film, the predicted kinetic inductance value is 0.07 pH/□. The material parameters were inputted into Sonnet, the narrow-band filter was re-simulated and the resulting S_{21} filter transmission is shown in figure 6.14. The new simulation is well matched the to measured filter profile and is further evidence that the narrow-band filter is functioning.

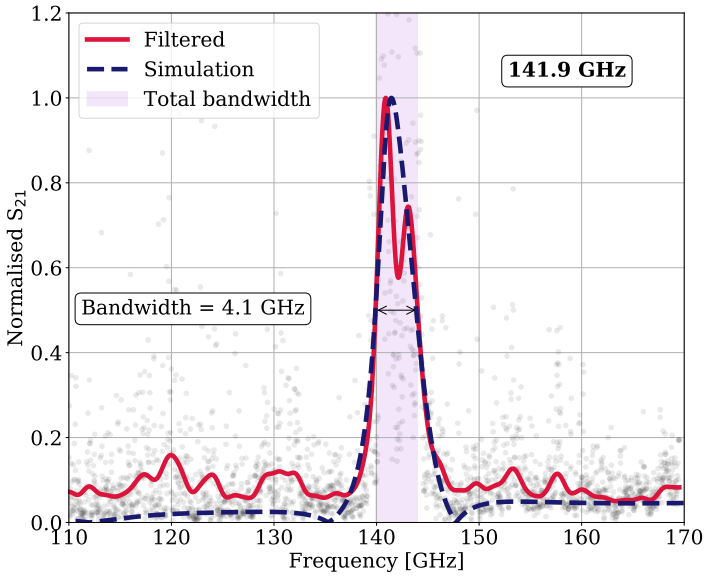

Figure 6.14: The spectral response of the narrow-band filtered KID. The raw data is in grey, and the smoothed, filtered data is the red solid line. A dashed blue line represented the sonnet simulation results from setting the kinetic inductance to 0.07 pH/□.

Although preliminary in design and measurement, the first iteration of on-chip filters in series with antenna-coupled LEKIDs has produced some promising spectral results. However a lot of noise is present in the data, but this is likely due to a sub-optimal experimental set up and, as discussed in the next chapter, possible stray light issues with the array. Moreover, the spectral results suggest the design process is robust, meaning future devices are easy to realise if the material properties are

known before design.

6.5 Summary

The next step required to realise a multi-chroic pixel, suitable for CMB experiments, is to utilise the length of microstrip, between the antenna and detector, to define the band of frequencies which reach the detector via on-chip filtering structures. Therefore, this chapter has detailed the theory and design process of filters comprised of resonating stubs.

Moreover, preliminary results obtained from measuring the spectral performance of single-colour prototypes have been presented in this chapter. The first iteration of on-chip filters coupled with mc-LEKIDs has produced some promising spectral results. However, a lot of a noise is present which make the spectral profiles difficult to extract and the filters are shifted to a lower frequency than designed. The possibly of stray light, which may have been a source of noise in these measurements, is presented in the next chapter.

7

Optical Results

With the dielectric requirement met and on-chip, in-line filters designed, the remaining component to consider for the single-colour prototype array is the optical performance of the mc-LEKIDs. The results presented in this chapter include the frequency response of the mc-LEKIDs to both temperature and optical power, and exploration of stray light issues with this device architecture. Data from device 2 are presented here. The radiation patterns were simulated by P.S. Barry.

7.1 Device 2

Device 2 is an array of nineteen detectors with seven antenna-coupled KIDs, seven non-antenna-coupled KIDs and five detectors which sit outside of the footprint of the lenslet array. Here, only fourteen of the detectors are functioning, resulting in a yield of 73.6%. The layout of this device is presented in figure 4.7 and the different layers of the device are shown in figure 4.8.

7.1.1 Experimental set up

To investigate how the performance of the detectors are impacted by the addition of in-line filters, the dark and optical response of the resonators was explored. Here, dark refers to having no optical load whilst changing the temperature of the baseplate which the sample sits on and optical refers to a changing optical load. The prototype device was placed in a gold-plated OFHC copper sample box and is installed on the 240-mK baseplate of a cryostat, as seen in figure 7.1, Alongside thermal and LPE filters at 8 and 9 cm^{-1}, a 150-GHz band-pass (BP) filter was placed in front of the detectors to limit the optical loading. The transmission profiles of the filters are shown in figure 7.2.

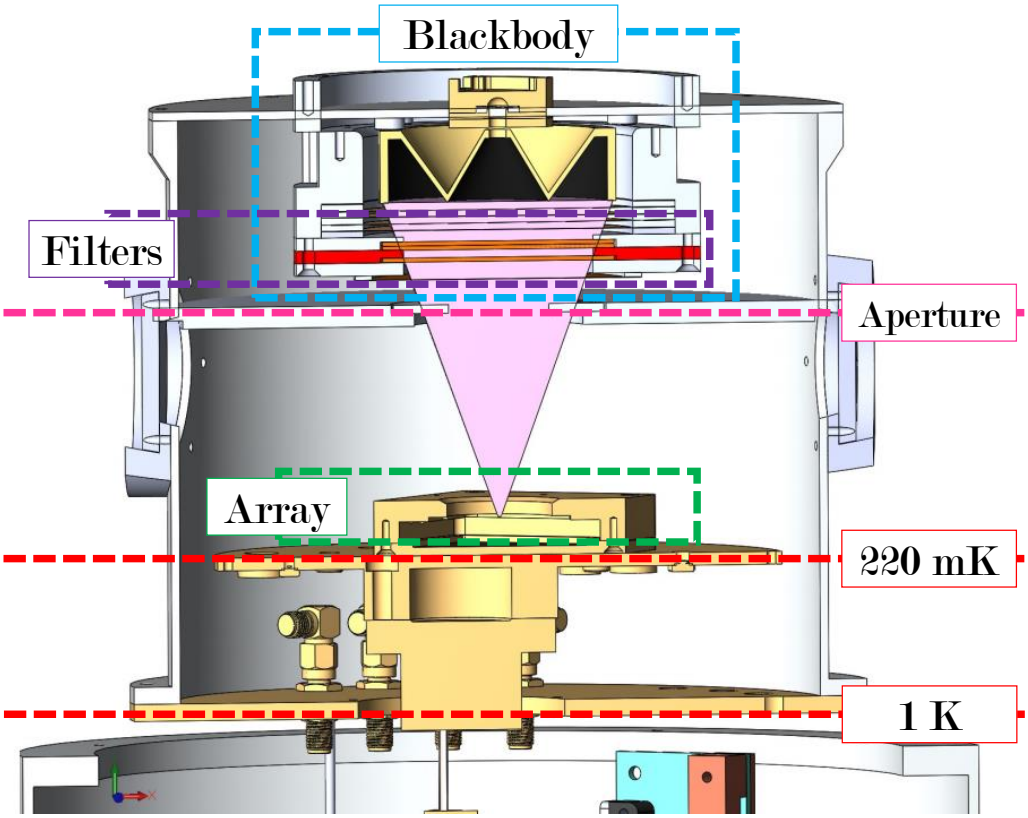

Figure 7.1: A schematic of the coldest two temperature stages of the cryostat, Elmo. The device array sits on the coldest stage, with the detectors pointing towards an aperture of the stage's can. The blackbody module is composed of a heating element located behind filters to limit the frequencies reaching the detector array.

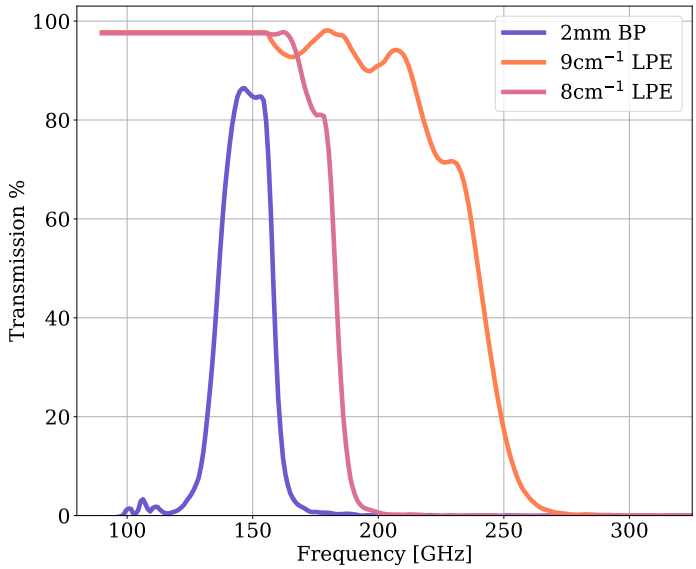

Figure 7.2: Filter transmission of the physical, metal-mesh filters placed within the cryostat system. The 8 and 9 cm^{-1} low-pass-edge filters are built into the blackbody stack, whereas the 2-mm band-pass filter is directly in front of the lenslet wafer.

As described in chapter 5, dark measurements are used to investigate the detector response to temperature. Here, each KID is driven at its optimal power and S_{21} is measured as the temperature of the base plate is varied between 240 – 350 mK. The optimal drive power is determined by the bifurcation point described in figure 5.3. To extract the resonator parameters, including Q_i and resonant frequency, the S_{21} data was fitted following the procedure outlined in Khalil et al. [84].

To measure the response of a KID to an optical source requires installing the array on the coldest stage of the cryostat, shown in figure 7.1, with the lenslet array facing up towards the blackbody module, composed of a heating element and the two LPE filters shown in figure 7.2 – the 8 and 9 cm^{-1}. The temperature of the heating element is varied between 10 and 75 K and the resonant frequency is measured using the VNA.

7.1.2 Scaling detector response

Due to differences in the absorbing volume of the KIDs on device 2, a scaling factor was calculated for each resonator to compensate for any additional response that

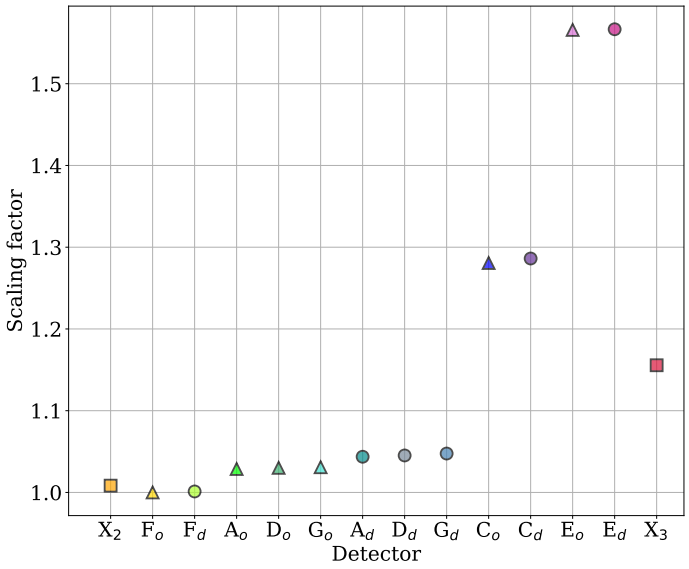

Figure 7.3: The scale factor, as determined from two Sonnet simulations, calculating the fractional frequency shift for each resonator and dividing it by the least responsive resonator in Sonnet, F_o.

was measured because of this. To determine the scaling factor, two sonnet simulations were created for each resonator, including an simulation to accurately reflect the expected response of the resonator and a second with the kinetic inductance value increased slightly in the absorbing Aluminium meander, mimicking the KID responding to an optical load. A scaling factor was calculated from the two sonnet simulations to compare the resonant frequencies from the two simulations. First, the fractional frequency shift was calculated, $(f - f_0)/f$, to account for differences in frequency response due to resonant frequency. Next, each fractional frequency shift value is divided by the resonator which moved the least, in this case F_o, to determine a scale factor.

Figure 7.3 details the scale factors calculated for each resonator, and the values are generally indicative of detector volume - the smaller the volume, the higher the scale factor. The F detectors have the largest absorbing meander volume, where V_{Al} = 1254 μm^3, which is why it is the least responsive detector and acts as a baseline for scaling. In descending order of volume, next are devices A, D, G and X, with a V_{Al} of 1214 μm^3, followed by B and C with V_{Al} = 1014 μm^3. The most responsive

devices, which has the smallest volume of 914 μm^3, are E.

7.1.3 Dark response

In the top plot of figure 7.5, which shows the dark fractional frequency shift of the antenna-coupled resonators, we observe that the detectors all respond similarly, regardless of location on the array and the addition of filters. This is also true for the dark detectors shown in figure 7.4. The most notable features include devices E_o and E_d being the most responsive, but this is to be expected because both detectors also have the smallest inductor volumes.

To account for the differences in response due to detector volume, each resonator was scaled according to the values presented in figure 7.3. The scaled frequency response is the lower plot in figures 7.5 and 7.4. Overall, the scale factor reduces the range of fractional frequency shift values in both the dark and antenna-coupled devices.

Furthermore, the quality factors extracted from our dark data exceed 10^5 for all detectors which demonstrates that adding in-line filters has a minimal, if any, impact on Q_i (see figure 7.6). This is an important result as high quality factors are beneficial for realising the large MUX ratios desired for future CMB observations, as it enables more resonators to fit within the bandwidth of the readout without overlap.

7.1.4 Optical response

Although relatively low in magnitude compared to the base temperature response, the fractional frequency response to the optical blackbody source in figure 7.7 is revealing. In terms of responsivity, the KIDs optically coupled to light via an antenna respond more to optical power than dark KIDs. This suggests there is at least some optical coupling, but further analysis is required to fully quantify the optical efficiency.

Furthermore, the detector with a broad-band filter is responding more than the detector connected to the narrow-band filter. This is further evidence which indicates the narrow-band filter is functional, as it has limited the optical response of the detector. However, the optical response has also been reduced to a level only

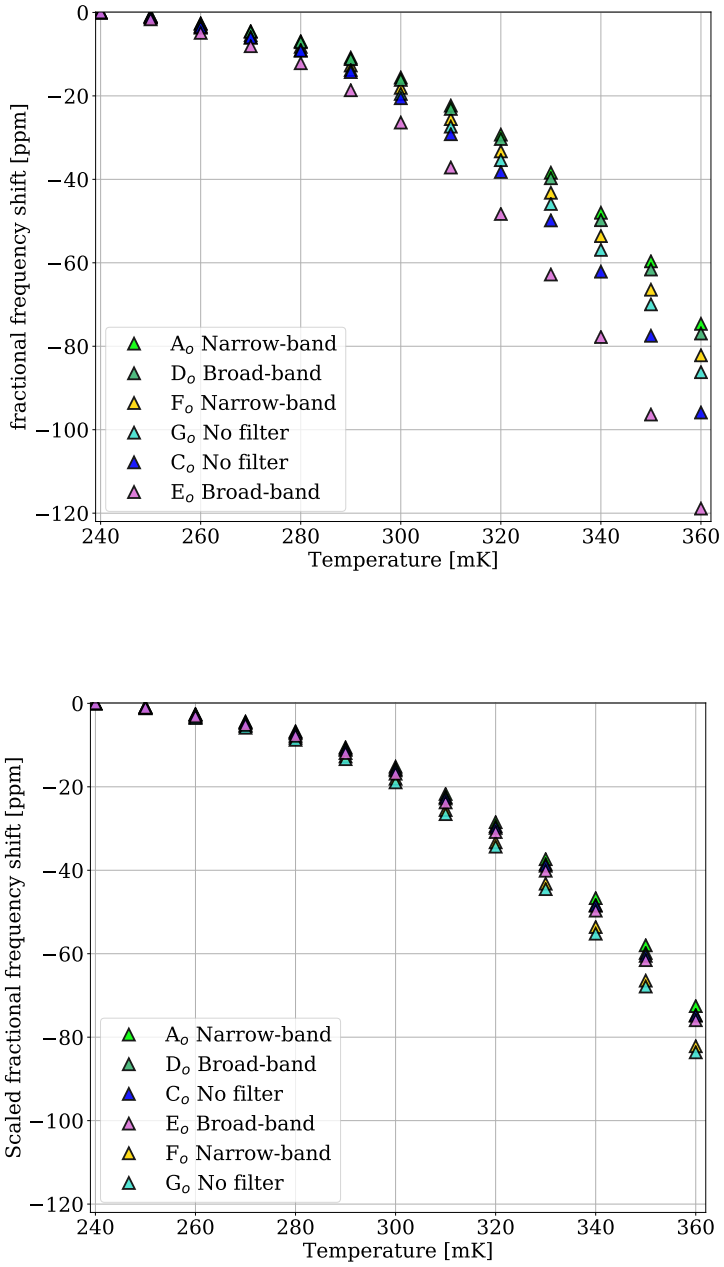

Figure 7.4: The dark frequency response of the antenna-coupled detectors marked by triangles. Each detector is also labelled in accordance to which on-chip filter is included, as discussed in chapter 6, from no filter and broad-band to narrow-band. The legend is organised in order of response, from lowest to highest. Each resonator in the lower plot has been scaled by the factor given in figure 7.3.

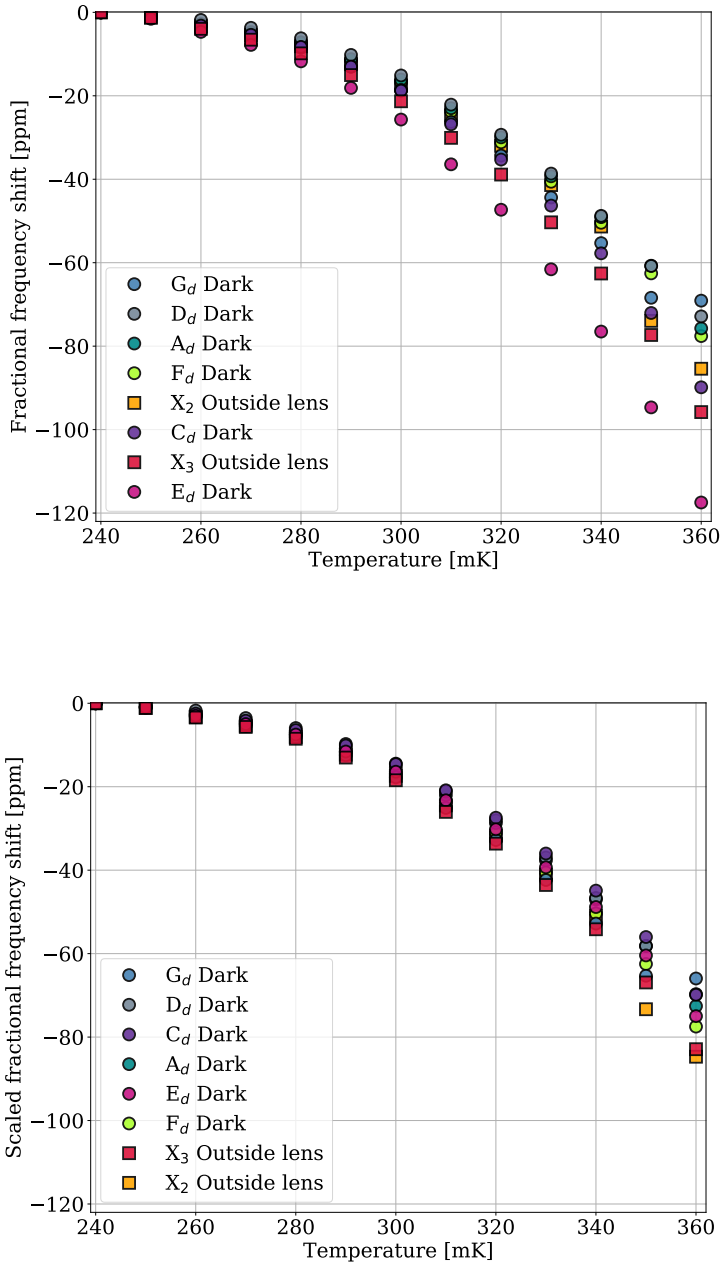

Figure 7.5: The dark frequency response of the dark, non-antenna-coupled detectors marked by circles. The squares represent detectors sitting outside the footprint of the lenslets. The legend is organised in order of response, from lowest to highest. Each resonator in the lower plot has been scaled by the factor given in figure 7.3.

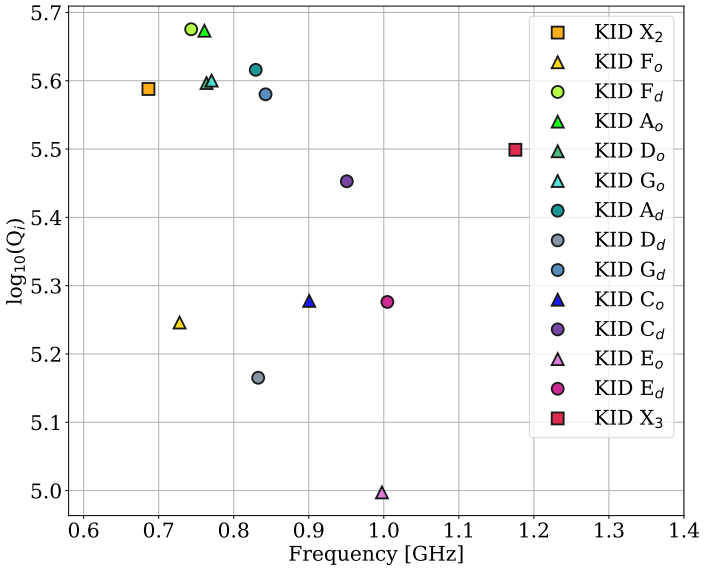

Figure 7.6: The intrinsic quality factor, Q_i, extracted from fitting S_{21} for each resonator in the array [84].

marginally higher than the dark detectors. The most responsive detector, E_o in figure 7.7, is only responding twice as much as most responsive dark detector, X_3 in figure 7.8.

Like the dark measurements of detectors, it is important to scale the frequency response of each resonator by the factor previously determined (see figure 7.3). This is shown in the lower plot in figure 7.7 and re-orders the detector response closer to the expected response due to on-chip filters. Here, the most responsive KIDs are C_o and G_o which are the filter-less KIDs. Next are the resonators coupled to a broad-band filter, detectors D_o and E_o, followed by the narrow-band resonators A_o and F_o. The scaled frequency response of the antenna-coupled LEKIDs on device 2 is indicative of on-chip filters responding and limiting the band of frequencies reaching the detector in agreement with the design of the filters.

7.2 Aperture testing of Device 2

Throughout the testing of device 2 the dark, non-optically-coupled resonators are responding considerably to our blackbody source. This is evident in figure 7.7 and

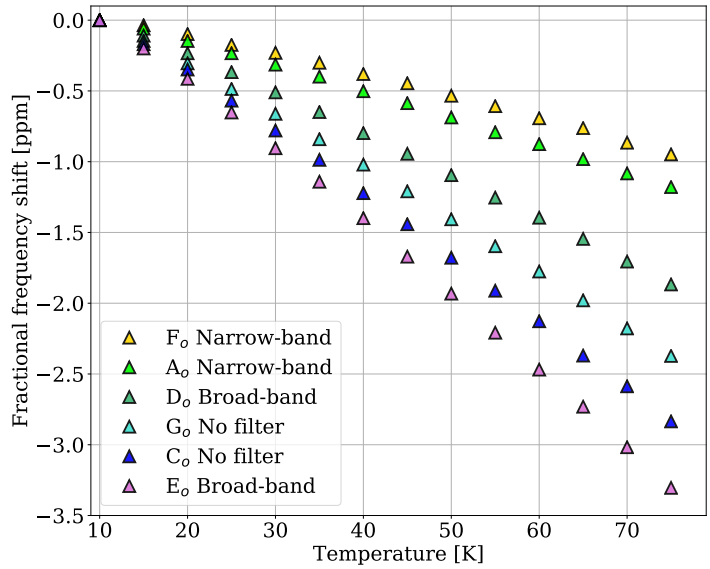

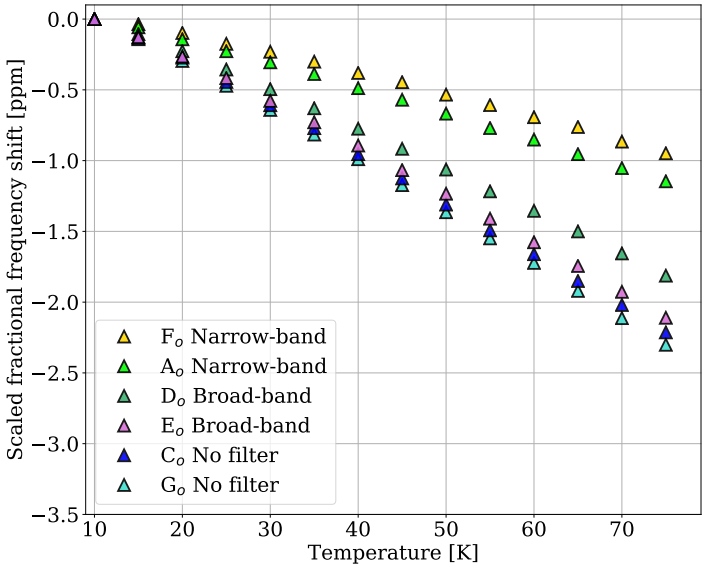

Figure 7.7: The frequency response to optical power of the antenna-coupled detectors marked by triangles. Each detector is also labelled by which on-chip filter is included, as discussed in chapter 6, from no filter and broad-band to narrow-band. The legend is organised in order of response, from lowest to highest. Each resonator in the lower plot has been scaled by the factor given in figure 7.3.

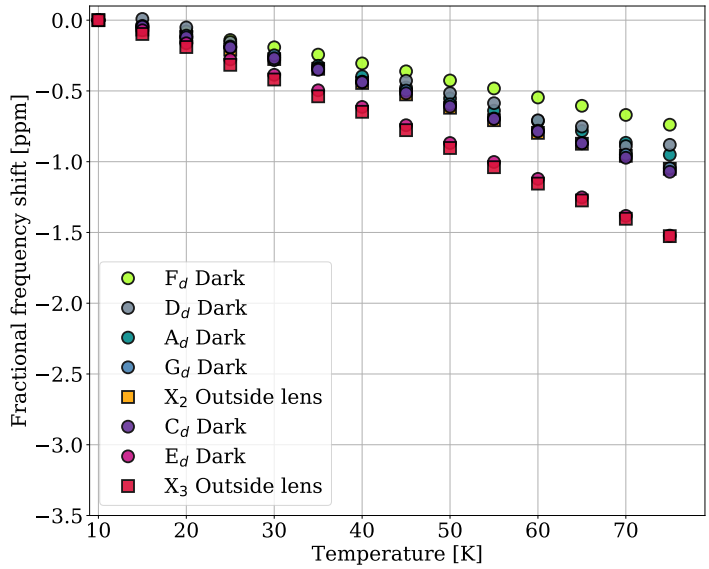

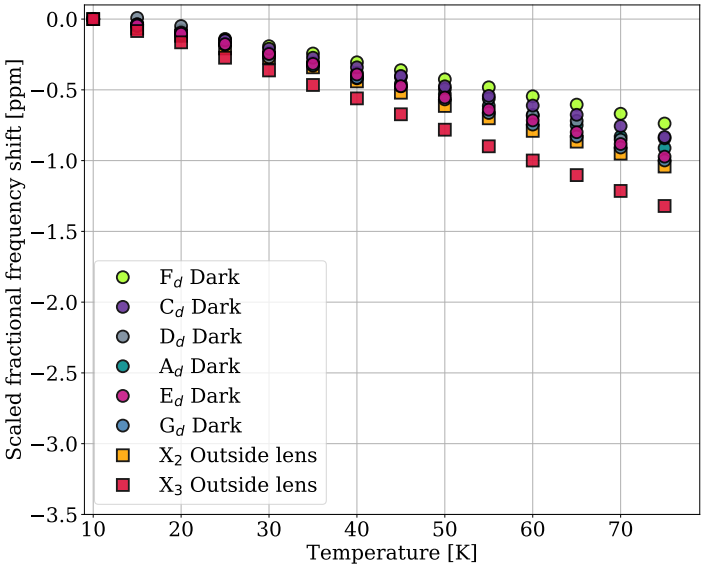

Figure 7.8: The frequency response to optical power of the dark, non-antenna-coupled detectors marked by circles. The squares represent detectors sitting outside the footprint of the lenslets. The legend is organised in order of response, from lowest to highest. Each resonator in the lower plot has been scaled by the factor given in figure 7.3.

7.8. Two possible explanations include poor optical efficiency and stray light, where light is getting between the lens and the wafer, causing dark detectors to respond. The latter occurs when light is directly being absorbed by the meander, essentially bypassing the antenna. This is depicted in figure 7.9 by the yellow optical path, which differs from the intended optical path in green. To test the theory of stray light, a physical aperture, with a diameter to match the size of the lenslet, was placed in front of the lenslet array to limit the light reaching the detectors.

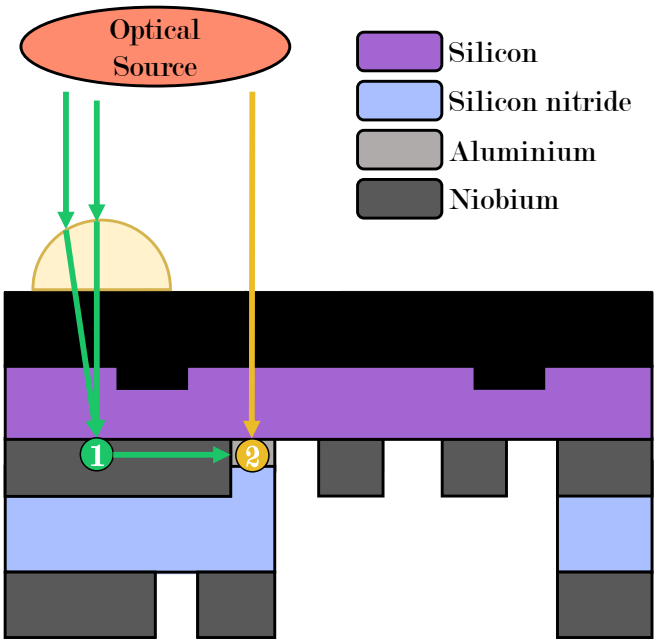

Figure 7.9: A diagram depicting how stray light could be reaching the detectors. The anticipated path of light in the lens-antenna-microstrip system is shown in green, where light travels from the optical source, is focused onto the antenna (1) before travelling down Niobium microstrip towards the Aluminium absorbing element of the KID (2). Instead light could hitting the Silicon wafer (yellow) and being absorbed directly by the Aluminium section (2).

7.2.1 Single aperture

To test the stray light theory, an aperture was placed over the centre lens only, illuminating the lens in front of optically-coupled detector, D_o and dark detector, D_d. This is shown in figure 7.10. We repeated the blackbody-response tests undertaken

Figure 7.10: The physical aperture plate placed in front of the lenslet array, limiting the light reaching the detectors. The 2-mm band-pass filter was placed in front of this aperture plate before testing to minimise detector loading.

without the aperture plate to see how it impacted detector response and compared the results as a ratio. The results of which are shown in the upper plot of figure 7.11.

Clearly, in the upper plot in figure 7.11, the optical detector sat underneath the aperture has maintained the most response. D_o response is 52% of its original value. Every other detector's response has been reduced to less than 10% of its original value, including D_d. This is an important observation because when stray light is reduced, via the aperture, the optical detector signal is much bigger than the dark detector. This is further evidence that light is reaching the detectors via the antenna.

7.2.2 Multiple apertures

The results obtained using a single aperture were encouraging, thus a further two apertures were opened up - exposing the optical and dark detectors under lenses E and F. Like before, the fractional frequency response to our blackbody source was measured as a function of blackbody temperature. The results are shown in the lower plot of figure 7.11.

It is very difficult to draw conclusions from the three-aperture response in figure 7.11 as it shows no clear trend in response. The dark detectors have started responding almost as much as the optical detectors, and the optical detectors which

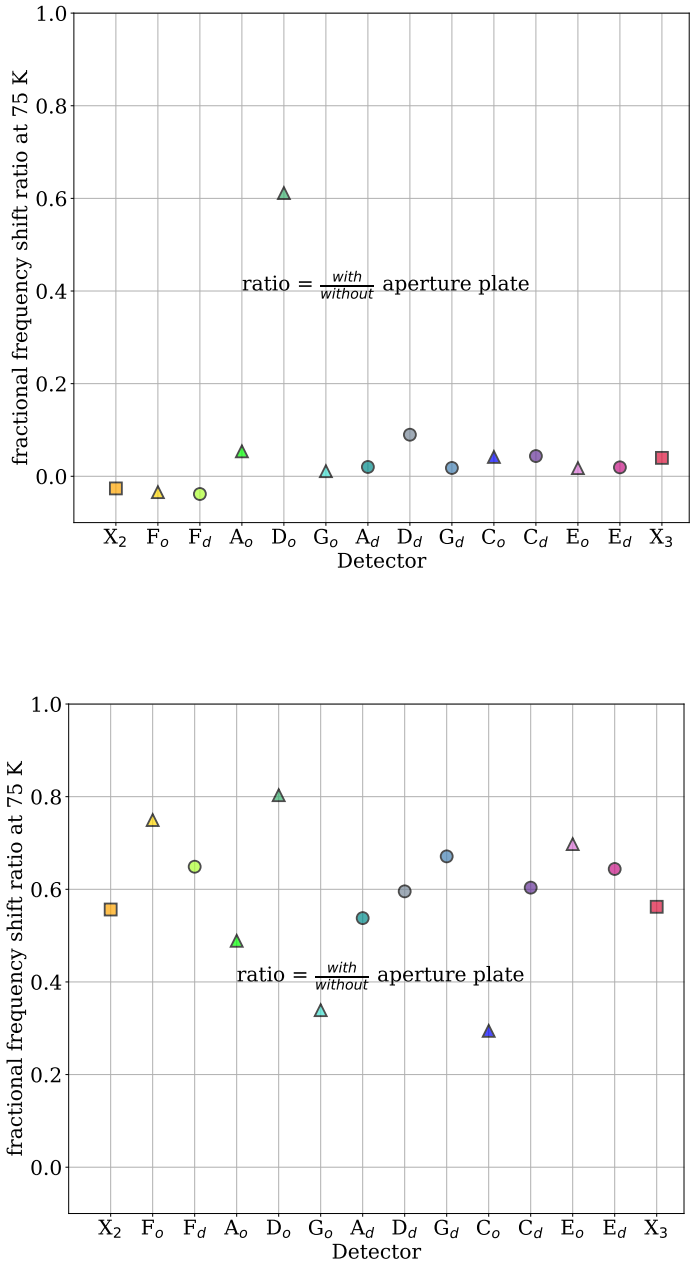

Figure 7.11: The ratio of the fractional frequency response of detectors in device array up to a blackbody source temperature of 75 K for with to without the addition of an aperture plate. The results of the single aperture is shown in the upper plot, whilst the lower plot is for multiple apertures. Square markers are for detectors which sit outside of the lens footprint, triangle markers are for antenna-coupled LEKIDs and circle markers are for dark, non-optically-coupled LEKIDs.

should be shielded from illumination have a response comparable to the detectors with open apertures. To determine whether detector location had an impact, further figures were created.

7.2.3 Impact of detector location

To investigate the impact of detector location, circle plots were created to highlight where each detector sits on the array and to help identify differences between the dark and optically-coupled detectors. The fractional frequency response at a given temperature, normalising the 75 K response to an initial temperature of 10 K, was compared before and after the aperture afterwards and this was turned into a ratio, as shown in figure 7.11. This is then turned into a percentage.

For the dark map of detectors, there are nine circles where the central seven are under lenslets - these are labelled A,B,C,D,E,F and G. Outside of the lenslet array sit several detectors and these are labelled X. For the following plots, device B did not yield and is therefore indicated by a black circle. The devices sitting underneath the aperture are highlighted by a black annulus.

In the upper plot of figure 7.12, the detector frequency response has been reduced to 8% or below of its original value. In fact, the devices hidden underneath the aperture plate have reduced to a response of 4% and below. This suggests the aperture plate is playing an important role in reducing the light being directly absorbed by dark, non-antenna-coupled resonators.

For the map of optically-coupled detectors, there are seven circles representing the seven optically-coupled detectors - these are labelled A,B,C,D,E,F and G. Like before, in the upper plot of figure 7.12, the devices sitting underneath the aperture are highlighted by a black annulus and device B did not yield and is therefore indicated by a black circle.

In the lower plot of figure 7.12 the frequency response of all detectors has been reduced significantly - even the detector currently exposed to optical power via the aperture. The response of each of the hidden detectors, A,C,E,F and G, has been reduced to 5% or less of their original, aperture-less value. The response of the exposed KID, detector D, has been reduced to 61% of its original value. This is still a strong detector response, but this would suggest light was getting in via

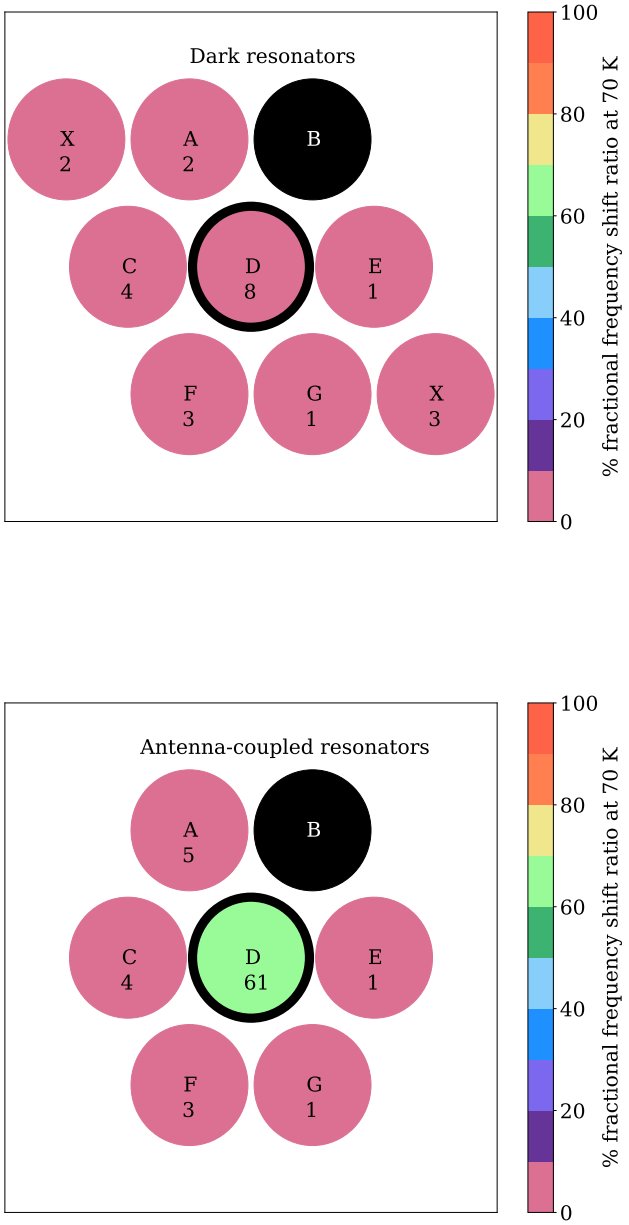

Figure 7.12: Aperture plot exploring the impact of detector location on response to stray light. The upper plot presents dark detectors, which are not coupled to detectors, whilst the lower plot presents data from antenna-coupled LEKIDs. Here, each detector is dark and is not optically coupled to a detector. The black annulus around lens D represent the physical aperture.

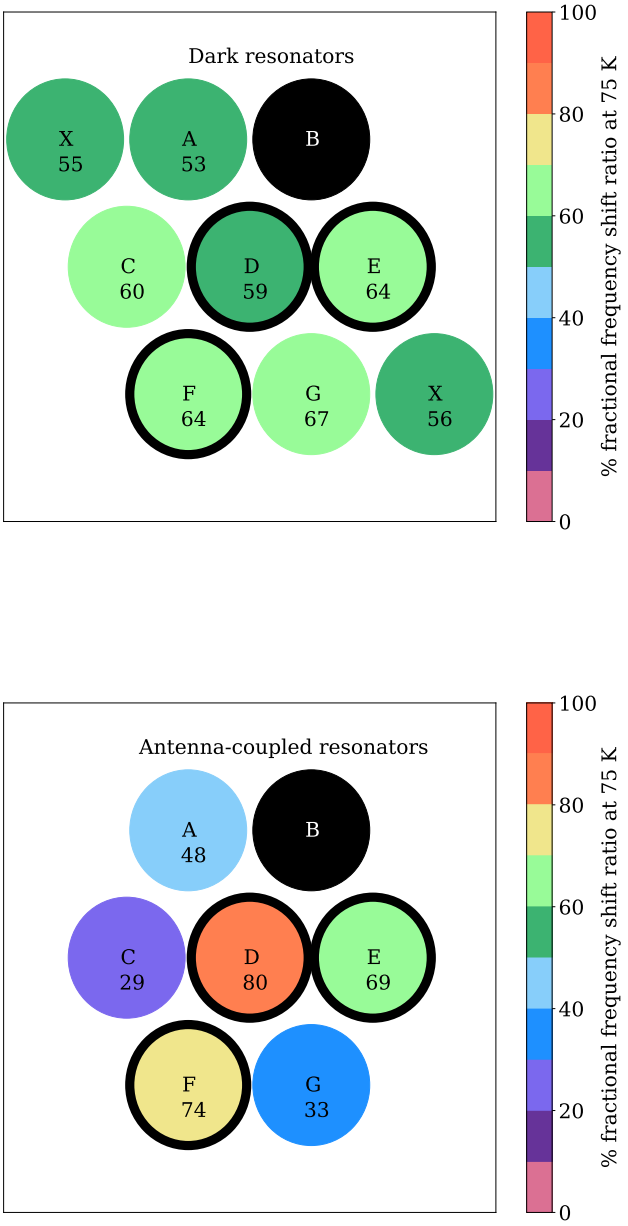

Figure 7.13: Aperture plot exploring the impact of detector location on response to stray light. The upper plot presents dark detectors, which are not coupled to detectors, whilst the lower plot presents data from antenna-coupled LEKIDs. Here, each detector is dark and is not optically coupled to a detector. The black annulus around lenses D, E and F represent the physical aperture.

mechanisms other than the antenna.

Opening up two additional apertures produced some interesting results, as shown in upper plot of figure 7.13. Now, each dark detector has a response of 67 % of its original value or less. This is a huge increase compared to opening one aperture. In fact, one of the hidden, dark detectors, detector G, is responding the most compared to the aperture-less results at 67 %.

For the antenna-coupled KIDs in the lower plot of figure 7.13, the detector sitting underneath the apertures still responded the most at 80%, 69% and 74% for detectors D,E and F. The hidden detectors had a response of 48% or lower which is still significant.

7.3 Simulations

One question that remains is whether the additional reduction in the detector response is purely due to the mitigation of stray light with the aperture, or if the aperture is truncating the beam, reducing the width of beam of the antenna/lenslet system. To determine the impact of the aperture on the beam, simulations were completed using the 3D electromagnetic (EM) simulation software, HFSS. The resulting simulations with and without an aperture plate are in figure 7.14.

The upper plot in figure 7.14 is of the radiation pattern in the XY and YZ plane of the antenna/lenslet system, whilst the lower plot includes the single-aperture plate shown in figure 4.6. Although adding the aperture to the system causes the radiation pattern to narrow, this is more notable when the signal is lower and therefore has a negligible impact. The 3 dB point, which represents the half-power point, is 11.20° and 12.66° at 0° and 90° without the aperture, and 12.28° and 12.57° with.

Moreover, with respect to the antenna, the angular size of the blackbody source is $\sim 15°$, thus the beam of the antenna is well within the beam of the blackbody both with and without the aperture plate. When the beams are 15° in width, the gain is -5.26 and -4.17 dB at a ϕ of 0° and 90° without the aperture, and -5.24 and -4.85 dB at a ϕ of 0° and 90° without the aperture. This translates to the aperture plate reducing the gain of the system by 5.5% angular size of the black body source.

To estimate the contribution of stray light to the overall signal, the dark device

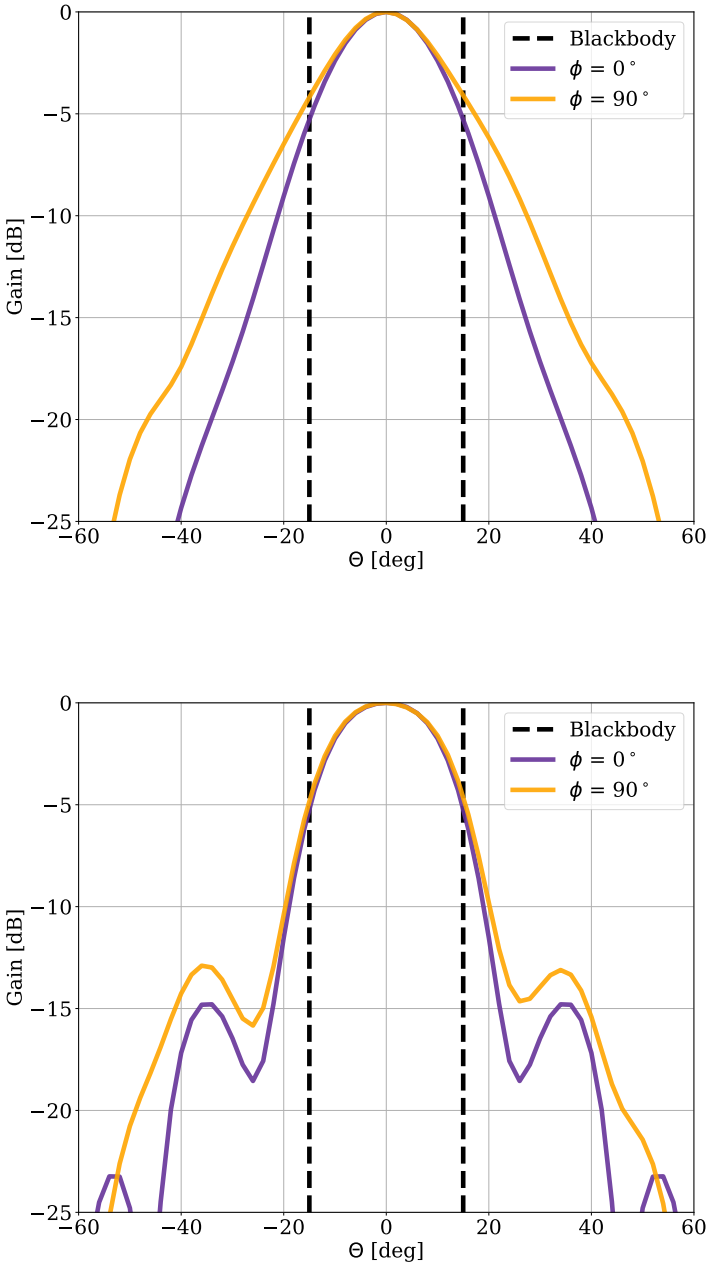

Figure 7.14: HFSS Simulations of the antenna/lenslet beam system with (upper) and without (lower) the single-aperture plate with a ϕ of 0 and 90°, representing the radiation pattern in the XY and YZ planes, respectively, as a function of angular distance from the antenna/lenslet system, Θ.

response with and without the aperture can be used to determine the stray light contribution from the rest of the chip. The scaled frequency response of detectors D_d (figure 7.8) and D_o (figure 7.7) are -0.84 and -1.81 at at blackbody temperature of 75 K. The stray light contribution from just the aperture can be determined from figure 7.11, where the response of D_d is reduced to 9% of its original response once the single-aperture plate is added, at 75 K. This equal to 0.076 in frequency response units of D_d's response and is therefore subtracted from D_d to get a frequency response of 0.764. Here, the stray light contribution from the aperture has been subtracted, thus this represents the remaining stray light response for device D_d and is assumed to be the stray light response for both detectors. Overall, the remaining frequency response of D_d is equal to 42.2% of D_o, which suggests stray light accounts for 42.2% of D_o to an optical load at 75 K. Recall, the measured response of detector D_o is reduced by $\sim$ 39% by the addition of the aperture plate. Therefore, this estimation of the stray-light contribution to the response of detector D_o of 42.2% supports the proposed stray-light mechanism within the detector architecture.

7.4 Summary

With the dielectric requirement satisfied in chapter 5 and the design and measured spectral performance of on-chip, in-line filters in chapter 6, this chapter focused on the optical performance of the mc-LEKIDs presented in the previous chapter - device 2. Both dark and optical measurements of the fractional frequency response yielded interesting results - especially the optical results of resonators coupled to an antenna.

For example, in figure 7.7, there is further evidence of the on-chip filters functioning because the response of resonators is ordered by the width of the on-chip filter. Here, the resonators with narrow-band filters responds the least, next are the resonators with broad-band filters followed by the filter-less resonator which is the most responsive. This is a promising result for a mc-LEKID coupled to an on-chip filter.

However, an obvious stray light issue has been identified through initial experiments exploring optical performance, and further confirmed through studying the

impact of an aperture on detector response. Although the results cannot conclusively target the source of stray light, the results do agree with the mechanism proposed in figure 7.9.

8

Future Work and Conclusion

As explored throughout the introduction, in chapter 1, the detection of primordial B-modes (a polarised component of the CMB) are critical to testing models of inflation. Current experiments, based on arrays of TESs, operate at the photon-noise limit, therefore to increase the sensitivity of instruments, more detectors are required. Moreover, observations at multiple frequencies are needed to characterise and remove contaminating foregrounds. To maximise the efficiency of focal planes, each pixel on the focal plane must be multi-chroic with dual-polarisation sensitivity and comprised of at least four detectors. Although this pixel architecture is already employed using TESs, the detectors numbers required by the next generation of CMB experiments presents a significant technical challenge. Therefore, this thesis proposes exchanging TESs for KIDs and a schematic of this pixel is shown in figure 1.1.

KIDs are superconducting resonators whose resonant frequency and quality factor are modified by optical power absorption. Large arrays of KIDs can be constructed without the need for additional multiplexing components, significantly re-

ducing the complexity of the cryogenics and detector readout in an experiment. To take advantage of existing CMB pixel architecture, and the separated inductive and capacitive elements of a LEKID, the mc-LEKID has been developed to reliably couple a microstrip transmission line and LEKID. The principle theory which describes LEKIDs, and their response to an optical load, is presented in chapters 2 and 3, alongside a discussion of noise sources.

To explore the feasibility of mc-LEKIDs, two types of arrays were designed during this research project – (i) the dielectric device and (ii) the filter-coupled device. First, a non-optically-coupled array was designed and tested to explore the impact of meeting the dielectric requirements of the mc-LEKID on detector performance. Next, an array of antenna-coupled and dark detectors, with some coupled to on-chip filters was realised to determine whether we could couple a LEKID to a microstrip and filtering structures. The designed, predicted and measured S_{21}, fabrication and experimental procedures needed to characterise the performance of both devices is discussed in chapter 4.

The impact of adding a dielectric to the mc-LEKID architecture was measured using of an array of bare, partially-covered and covered resonators, the results of which form the basis of chapter 5. Back-bending, where the resonant frequency first increases with temperature before decreasing, was observed in the covered devices which is indicative of TLSs, but is not as discernible for partially-covered and bare devices. The product of the fill factor and dielectric loss tangent, $F\delta_0$, was extracted from fitting the resonant frequency response to temperature and was found to be, on average, 16 times lower across the partially-covered and bare resonators when compared to their covered counterparts (see figure 5.9).

Furthermore, the fractional frequency noise (df/f_0) of each detector at a modulation frequency was measured to compare detector noise in the flat region of the noise power spectral density. The average noise level is $3.8\text{x}10^{-18}\text{Hz}^{-1}$ for the covered detectors, which is 25 times higher than partially-covered detectors and 22 times higher than bare detectors. This indicated the addition of dielectric to the absorbing meander only does not result in excess noise. The dark detector NEP was also calculated to be $(5.73\pm0.12)\text{x}10^{-18}$ $\text{WHz}^{-1/2}$ for an example covered resonator, $(1.85\pm0.03)\text{x}10^{-18}$ $\text{WHz}^{-1/2}$ for a partially-covered resonator and $(1.28\pm0.02)\text{x}10^{-18}$

$WHz^{-1/2}$ for a bare resonator.

There are two clear avenues to explore from the results presented in chapter 5 – the low-frequency regime of the noise power spectrum to ensure to characterise the anticipated $1/f^x$ slope indicative of TLSs, and creating a device which closer matches the schematics of the optical devices. This requires the addition of a ground plane over the absorbing meander and dielectric, and will impact overall performance of the LEKID.

The focus of chapter 6 was to utilise the length of microstrip, between the antenna and detector, to incorporate on-chip filters which define the band of frequencies travelling towards the detector. This work is inspired by the on-chip filters already utilised by ground-based CMB experiments [3, 4, 5]. In chapter 6, the theory required to understand the fundamental principles of filtering structures, known as resonant stubs, were presented alongside details of the procedure followed to design two filters close to the peak CMB frequency – a narrow-band and broad-band filter centred at 140 GHz. The filter designs were coupled to the detectors on device 2.

Preliminary results of the narrow-band filter produced a spectral profile that can be matched up to simulation using the measured material parameters to determine the kinetic inductance of the niobium. Here, the narrow-band filter has a central frequency of 141.9 GHz with a bandwidth of 4.1 GHz, compared to a simulated central frequency of $\sim$ 138 GHz with a bandwidth of 4 GHz. The broad-band filter did span a bandwidth of $\sim$ 29.1 GHz centred at 140.7 GHz, but also contained several unwanted features. To continue the development of the on-chip filters presented in chapter 6 require an improved experimental set up to measure the transmission profile of the filters that is less susceptible to noise.

With the dielectric requirement met and on-chip, in-line filters designed, the remaining component to consider is the optical performance of the mc-LEKIDs of device 2. The frequency of the mc-LEKIDs to both temperature and optical power are explored in chapter 7, alongside the unfortunate issue of stray light. In terms of a scaled frequency response to optical power, the filter-less KIDs responded the most, followed by the broad-band-filtered KIDs, the narrow-band-filtered KIDs and the dark KIDs. This is secondary evidence of the filters presented in 6 limiting the frequencies reaching the detectors and are, thus, operating as intended.

As discussed in chapter 7, there is a stray light issue with the current architecture. The mechanism which seems to explain the results is light is getting between the lens and the wafer, causing dark detectors to respond because light is being directly absorbed by the meander. The inclusion of an aperture only reducing the frequency response of the exposed optical detector, D_o, by $\sim 40\%$ is evidence of light being coupled into the detector, via the antenna. Going forward, a simple solution to the stray light problem is to utilise horn-coupling, instead of an lenslet array, as horns can be designed to accept fewer transverse electric modes and detectors are therefore less susceptible to stray light. Additionally, reducing the impact of stray light should reduce the noise present in measurements of on-chip filters.

However, lens-coupling should not be ruled out from inclusion in future pixel designs because it may be possible to solve the stray-light problem through a modified detector architecture or addition of an absorbing layer. Such improvements were in the design phase before the COVID-19 pandemic. Moreover, it may soon be possible to create arrays of flat lenses at Cardiff to couple light into the antennas. Flat lenses are advantageous over lenslet arrays that require each lenslet to be glued into place. Moreover, it is possible to replace the twin-slot antenna with a sinuous antenna or planar orthomode transducer (OMT), which is capable of coupling to a wider band of frequencies. Both coupling architectures have already been utilised in many ground-based CMB experiments [89, 5, 90, 91, 92].

Throughout this thesis, several developments have been presented, including coupling a KID to an antenna and microstrip which is made possible by the separated inductor and capacitor of a KID, enabling dielectric to be placed over the inductor only which reduces the detectors susceptibility to the noise created by two-level systems. With the dielectric requirements of the microstrip met, the section of microstrip between the antenna and KID can be utilised to introduce on-chip filtering structures to limit the band of frequencies reaching the detector. Although certain studies presented in this thesis have been more successful than others, the work presented here is a good foundation to realising the large arrays of multi-chroic, polarisation-sensitive detectors which will be beneficial to future CMB experiments.

Bibliography

[1] P. A.R. Ade et al. "Planck intermediate results: XXXVIII. E- and B-modes of dust polarization from the magnetized filamentary structure of the interstellar medium". In: *Astronomy and Astrophysics* 586 (Feb. 2016). ISSN: 14320746. DOI: 10.1051/0004-6361/201526506.

[2] Stephan J. Huber and Thomas Konstandin. "Production of gravitational waves in the nMSSM". In: *Journal of Cosmology and Astroparticle Physics* 2008.5 (May 2008), p. 017. ISSN: 14757516. DOI: 10.1088/1475-7516/2008/05/017. URL: https://iopscience.iop.org/article/10.1088/1475-7516/2008/05/017%20https://iopscience.iop.org/article/10.1088/1475-7516/2008/05/017/meta.

[3] P. A.R. Ade et al. "Joint Analysis of BICEP2/Keck Array and Planck Data". In: *Physical Review Letters* 114.10 (Mar. 2015), pp. 1–17. ISSN: 10797114. DOI: 10.1103/PhysRevLett.114.101301. URL: https://journals.aps.org/prl/abstract/10.1103/PhysRevLett.114.101301.

[4] B. A. Benson et al. "SPT-3G: a next-generation cosmic microwave background polarization experiment on the South Pole telescope". In: *Millimeter, Submillimeter, and Far-Infrared Detectors and Instrumentation for Astronomy VII*. Ed. by Wayne S. Holland and Jonas Zmuidzinas. Vol. 9153. SPIE, July 2014, 91531P. DOI: 10.1117/12.2057305. URL: http://proceedings.spiedigitallibrary.org/proceeding.aspx?doi=10.1117/12.2057305.

[5] M. D. Niemack et al. "ACTPol: A polarization-sensitive receiver for the Atacama Cosmology Telescope". In: *Millimeter, Submillimeter, and Far-Infrared Detectors and Instrumentation for Astronomy V* 7741 (June 2010), 77411S.

DOI: 10.1117/12.857464. URL: http://arxiv.org/abs/1006.5049%20http://dx.doi.org/10.1117/12.857464.

[6] Peter K. Day et al. "A broadband superconducting detector suitable for use in large arrays". In: *Nature* 425.6960 (Oct. 2003), pp. 817–821. ISSN: 00280836. DOI: 10.1038/nature02037. URL: https://www.nature.com/articles/nature02037.

[7] Simon Doyle et al. "Lumped element kinetic inductance detectors". In: *Journal of Low Temperature Physics* 151.1-2 PART 1 (Apr. 2008), pp. 530–536. ISSN: 00222291. DOI: 10.1007/s10909-007-9685-2. URL: https://link.springer.com/article/10.1007/s10909-007-9685-2.

[8] P.S. Barry et al. "Design and Performance of the Antenna-Coupled Lumped-Element Kinetic Inductance Detector". In: *Journal of Low Temperature Physics* 193.3-4 (2018). ISSN: 15737357. DOI: 10.1007/s10909-018-1943-y.

[9] W. A. Phillips. "Tunneling states in amorphous solids". In: *Journal of Low Temperature Physics* 7.3-4 (May 1972), pp. 351–360. ISSN: 00222291. DOI: 10.1007/BF00660072. URL: https://link.springer.com/article/10.1007/BF00660072.

[10] P. W. Anderson, B. I. Halperin, and C. M. Varma. "Anomalous low-temperature thermal properties of glasses and spin glasses". In: *Philosophical Magazine* 25.1 (1972), pp. 1–9. ISSN: 00318086. DOI: 10.1080/14786437208229210. URL: https://www.tandfonline.com/doi/abs/10.1080/14786437208229210.

[11] A. L. Hornsby et al. "Reducing the Susceptibility of Lumped-Element KIDs to Two-Level System Effects". In: *Journal of Low Temperature Physics* (July 2020), pp. 1–8. ISSN: 15737357. DOI: 10.1007/s10909-020-02501-7. URL: https://doi.org/10.1007/s10909-020-02501-7.

[12] Ludwig Boltzmann. "Ableitung des Stefan'schen Gesetzes, betreffend die Abhängigkeit der Wärmestrahlung von der Temperatur aus der electromagnetischen Lichttheorie". In: *Annalen der Physik* 258.6 (Jan. 1884), pp. 291–294. ISSN: 15213889. DOI: 10.1002/andp.18842580616. URL: https://onlinelibrary.wiley.com/doi/full/10.1002/andp.18842580616%20https://onlinelibrary.

wiley.com/doi/abs/10.1002/andp.18842580616%20https://onlinelibrary.wiley.com/doi/10.1002/andp.18842580616.

[13] J Stefan. "Über die Beziehung zwischen der Wärmestrahlung und der Temperatur." In: *Aus der k.k. Hof-und Staatsdruckerei, 391-428.* 79 (1879), pp. 391–428. URL: https://www.scirp.org/(S(i43dyn45teexjx455qlt3d2q))/reference/ReferencesPapers.aspx?ReferenceID=2259621.

[14] A K T Assis and M C D Neves. *History of the 2.7 K Temperature Prior to Penzias and Wilson.* Tech. rep. 3. 1995.

[15] A. S. Eddington and A. S. "The Internal Constitution of the Stars". In: *ics* (1926). URL: https://ui.adsabs.harvard.edu/abs/1926ics..book.....E/abstract.

[16] E. P. Hubble. "Extragalactic nebulae." In: *The Astrophysical Journal* 64 (Dec. 1926), p. 321. ISSN: 0004-637X. DOI: 10.1086/143018. URL: https://ui.adsabs.harvard.edu/abs/1926ApJ....64..321H/abstract.

[17] G Gamow. *The Creation of the Universe - George Gamow - Google Books.* Viking Press, 1961. URL: https://books.google.co.uk/books?id=5awirwgmvAoC&pg=PA40&lpg=PA40&redir_esc=y#v=onepage&q&f=false.

[18] H Kragh. *Cosmology and controversy : the historical development of two theories of the universe.* Princeton, NJ : Princeton University Press, 1999. URL: https://archive.org/details/cosmologycontrov00helg.

[19] R. H. Dicke et al. "Cosmic Black-Body Radiation." In: *The Astrophysical Journal* 142 (July 1965), p. 414. ISSN: 0004-637X. DOI: 10.1086/148306.

[20] A. A. Penzias and R. W. Wilson. "A Measurement of Excess Antenna Temperature at 4080 Mc/s." In: *The Astrophysical Journal* 142 (July 1965), p. 419. ISSN: 0004-637X. DOI: 10.1086/148307.

[21] A Liddle. *An Introduction to Modern Cosmology.* Wiley, 2007. URL: https://books.google.co.uk/books/about/An_Introduction_to_Modern_Cosmology.html?id=zZg3AQAAIAAJ&source=kp_book_description&redir_esc=y.

[22] D. J. Fixsen. "The Temperature of the Cosmic Microwave Background". In: *Astrophysical Journal* 707.2 (Nov. 2009), pp. 916–920. DOI: 10.1088/0004-637X/707/2/916. URL: http://arxiv.org/abs/0911.1955%20http://dx.doi.org/10.1088/0004-637X/707/2/916.

[23] H.-G. Schöpf. "Mehra, J. / Rechenberg, H., The Historical Development of Quantum Theory. Vol. 1, Part 1 & 2: The Quantum Theory of Planck, Einstein, Bohr and Sommerfeld: Its Foundation and the Rise of Its Difficulties, 1900–1925. Berlin-Heidelberg-New York, Springer-Verlag 1982. Part 1: XLVII, 372 S., DM 75, —. US $ 31.30. ISBN 3-540-90642-8, Part 2: VI, 506 S., DM 85, —. US $ 34.00. ISBN 3-540-90667-3". In: *ZAMM - Zeitschrift für Angewandte Mathematik und Mechanik* 63.10 (Jan. 1983), pp. 522–522. ISSN: 00442267. DOI: 10.1002/zamm.19830631018. URL: http://doi.wiley.com/10.1002/zamm.19830631018.

[24] G. F. Smoot, M. V. Gorenstein, and R. A. Muller. "Detection of anisotropy in the cosmic blackbody radiation". In: *Physical Review Letters* 39.14 (Oct. 1977), pp. 898–901. ISSN: 00319007. DOI: 10.1103/PhysRevLett.39.898. URL: https://journals.aps.org/prl/abstract/10.1103/PhysRevLett.39.898.

[25] R. Adam et al. "Planck 2015 results: I. Overview of products and scientific results". In: *Astronomy and Astrophysics* 594 (Oct. 2016), p. 39. ISSN: 14320746. DOI: 10.1051/0004-6361/201527101. URL: http://healpix.sourceforge.net/html/intronode6.htm.

[26] P. J. E. Peebles and J. T. Yu. "Primeval Adiabatic Perturbation in an Expanding Universe". In: *The Astrophysical Journal* 162 (Dec. 1970), p. 815. ISSN: 0004-637X. DOI: 10.1086/150713. URL: https://ui.adsabs.harvard.edu/abs/1970ApJ...162..815P/abstract.

[27] M. J. Rees. "Polarization and Spectrum of the Primeval Radiation in an Anisotropic Universe". In: *The Astrophysical Journal* 153.3 (July 1968), p. L1. ISSN: 0004-637X. DOI: 10.1086/180208. URL: https://ui.adsabs.harvard.edu/abs/1968ApJ...153L...1R/abstract.

[28] Alan H. Guth. "Inflationary universe: A possible solution to the horizon and flatness problems". In: *Physical Review D* 23.2 (Jan. 1981), pp. 347–356. ISSN: 05562821. DOI: 10.1103/PhysRevD.23.347. URL: https://journals.aps.org/prd/abstract/10.1103/PhysRevD.23.347.

[29] A. A. Starobinskiĭ, Starobinskiĭ, and A. A. "Spectrum of relict gravitational radiation and the early state of the universe". In: *JETPL* 30 (1979), p. 682. ISSN: 0021-3640. URL: https://ui.adsabs.harvard.edu/abs/1979JETPL..30..682S/abstract.

[30] Kevork N. Abazajian et al. "CMB-S4 Science Book, First Edition". In: (Oct. 2016). URL: http://arxiv.org/abs/1610.02743.

[31] P. A.R. Ade et al. "Constraints on Primordial Gravitational Waves Using Planck, WMAP, and New BICEP2/ Keck Observations through the 2015 Season". In: *Physical Review Letters* 121.22 (Nov. 2018), p. 221301. ISSN: 10797114. DOI: 10.1103/PhysRevLett.121.221301. URL: https://journals.aps.org/prl/abstract/10.1103/PhysRevLett.121.221301.

[32] Kevork Abazajian et al. "CMB-S4 Science Case, Reference Design, and Project Plan". In: (July 2019). URL: http://arxiv.org/abs/1907.04473.

[33] P. A.R. Ade et al. "Joint Analysis of BICEP2/Keck Array and Planck Data". In: *Physical Review Letters* 114.10 (Mar. 2015), pp. 1–17. ISSN: 10797114. DOI: 10.1103/PhysRevLett.114.101301. URL: https://ui.adsabs.harvard.edu/abs/2015PhRvL.114j1301B/abstract.

[34] Planck Collaboration et al. "Planck 2015 results. X. Diffuse component separation: Foreground maps". In: (Feb. 2015). DOI: 10.1051/0004-6361/201525967. URL: https://arxiv.org/abs/1502.01588.

[35] Planck Collaboration et al. "Planck 2018 results. IV. Diffuse component separation". In: (July 2018). URL: https://arxiv.org/abs/1807.06208.

[36] D. T. Chuss et al. "Cosmology Large Angular Scale Surveyor (CLASS) Focal Plane Development". In: *Journal of Low Temperature Physics* 184.3-4 (Aug. 2016), pp. 759–764. ISSN: 15737357. DOI: 10.1007/s10909-015-1368-9. URL: https://link.springer.com/article/10.1007/s10909-015-1368-9.

[37] K. Arnold et al. "The bolometric focal plane array of the POLARBEAR CMB experiment". In: *Millimeter, Submillimeter, and Far-Infrared Detectors and Instrumentation for Astronomy VI*. Ed. by Wayne S. Holland. Vol. 8452. SPIE, Sept. 2012, p. 84521D. DOI: 10.1117/12.927057. URL: http://proceedings.spiedigitallibrary.org/proceeding.aspx?doi=10.1117/12.927057.

[38] R. Datta et al. "Horn coupled multichroic polarimeters for the atacama cosmology telescope polarization experiment". In: *Journal of Low Temperature Physics* 176.5-6 (Feb. 2014), pp. 670–676. ISSN: 15737357. DOI: 10.1007/s10909-014-1134-4. URL: https://link.springer.com/article/10.1007/s10909-014-1134-4.

[39] P. A.R. Ade et al. "Antenna-coupled TES bolometers used in BICEP2, keck array, and spider". In: *Astrophysical Journal* 812.2 (Oct. 2015), p. 176. ISSN: 15384357. DOI: 10.1088/0004-637X/812/2/176. URL: https://iopscience.iop.org/article/10.1088/0004-637X/812/2/176%20https://iopscience.iop.org/article/10.1088/0004-637X/812/2/176/meta.

[40] C. M. Posada et al. "Fabrication of large dual-polarized multichroic TES bolometer arrays for CMB measurements with the SPT-3G camera". In: *Superconductor Science and Technology* 28.9 (Sept. 2015), p. 094002. ISSN: 13616668. DOI: 10.1088/0953-2048/28/9/094002. URL: https://iopscience.iop.org/article/10.1088/0953-2048/28/9/094002%20https://iopscience.iop.org/article/10.1088/0953-2048/28/9/094002/meta.

[41] Lei Zhu, Sheng Sun, and Rui Li. *Microwave Bandpass Filters for Wideband Communications | Wiley*. 2012, p. 240. URL: https://www.wiley.com/en-us/Microwave+Bandpass+Filters+for+Wideband+Communications-p-9780470876619.

[42] Sam Rowe et al. "A passive THz video camera based on lumped element kinetic inductance detectors". In: *Review of Scientific Instruments* 87.3 (Nov. 2015). DOI: 10.1063/1.4941661. URL: http://arxiv.org/abs/1511.06011%20http://dx.doi.org/10.1063/1.4941661.

[43] A. N. Bender et al. "Integrated performance of a frequency domain multiplexing readout in the SPT-3G receiver". In: *Millimeter, Submillimeter, and Far-*

Infrared Detectors and Instrumentation for Astronomy VIII. Ed. by Wayne S. Holland and Jonas Zmuidzinas. Vol. 9914. SPIE, July 2016, p. 99141D. DOI: 10.1117/12.2232146. URL: http://proceedings.spiedigitallibrary.org/proceeding.aspx?doi=10.1117/12.2232146.

[44] K. Rotermund et al. "Planar Lithographed Superconducting LC Resonators for Frequency-Domain Multiplexed Readout Systems". In: *Journal of Low Temperature Physics* 184.1-2 (July 2016), pp. 486–491. ISSN: 15737357. DOI: 10.1007/s10909-016-1554-4. URL: https://link.springer.com/article/10.1007/s10909-016-1554-4.

[45] D. Barron et al. "Development and characterization of the readout system for POLARBEAR-2". In: *Millimeter, Submillimeter, and Far-Infrared Detectors and Instrumentation for Astronomy VII*. Ed. by Wayne S. Holland and Jonas Zmuidzinas. Vol. 9153. SPIE, July 2014, p. 915335. DOI: 10.1117/12.2055611. URL: http://proceedings.spiedigitallibrary.org/proceeding.aspx?doi=10.1117/12.2055611.

[46] John F. Cochran and D. E. Mapother. "Superconducting Transition in Aluminum". In: *Physical Review* 111.1 (1958), pp. 132–142. ISSN: 0031899X. DOI: 10.1103/PhysRev.111.132. URL: https://ui.adsabs.harvard.edu/abs/1958PhRv..111..132C/abstract.

[47] R. Barends et al. "Contribution of dielectrics to frequency and noise of NbTiN superconducting resonators". In: *Applied Physics Letters* 92.22 (June 2008), p. 223502. ISSN: 00036951. DOI: 10.1063/1.2937837. URL: http://aip.scitation.org/doi/10.1063/1.2937837.

[48] Jiansong Gao et al. "Experimental evidence for a surface distribution of two-level systems in superconducting lithographed microwave resonators". In: *Applied Physics Letters* 92.15 (Apr. 2008), p. 152505. ISSN: 00036951. DOI: 10.1063/1.2906373. URL: http://aip.scitation.org/doi/10.1063/1.2906373.

[49] R. Barends et al. "Reduced frequency noise in superconducting resonators". In: *Applied Physics Letters* 97.3 (July 2010), p. 033507. ISSN: 00036951. DOI:

10.1063/1.3467052. URL: http://aip.scitation.org/doi/10.1063/1.3467052.

[50] M. Molina-Ruiz et al. "Origin of Mechanical and Dielectric Losses from Two-Level Systems in Amorphous Silicon". In: (Aug. 2020). URL: http://arxiv.org/abs/2008.07489.

[51] H. Kamerlingh Onnes. "Further experiments with Liquid Helium. G. On the Electrical Resistance of Pure Metals, etc. VI. On the Sudden Change in the Rate at which the Resistance of Mercury Disappears." In: Springer, Dordrecht, 1991, pp. 267–272. DOI: 10.1007/978-94-009-2079-8{_}17. URL: https://link.springer.com/chapter/10.1007/978-94-009-2079-8_17.

[52] S. Noguchi and A. Ishiyama. "Optimal design method for MRI superconducting magnets with ferromagnetic shield". In: *IEEE Transactions on Magnetics* 33.2 (Mar. 1997), pp. 1904–1907. ISSN: 00189464. DOI: 10.1109/20.582660. URL: http://ieeexplore.ieee.org/document/582660/.

[53] Jiasu Wang et al. "The first man-loading high temperature superconducting Maglev test vehicle in the world". In: *Physica C: Superconductivity and its Applications*. Vol. 378-381. PART 1. North-Holland, Oct. 2002, pp. 809–814. DOI: 10.1016/S0921-4534(02)01548-4.

[54] W. Meissner and R. Ochsenfeld. "Ein neuer Effekt bei Eintritt der Supraleitfähigkeit". In: *Die Naturwissenschaften* 21.44 (Nov. 1933), pp. 787–788. ISSN: 00281042. DOI: 10.1007/BF01504252. URL: https://link.springer.com/article/10.1007/BF01504252.

[55] Jiansong Gao. "The Physics of Superconducting Microwave Resonators". PhD thesis. 2008.

[56] Benjamin Mazin. "Microwave Kinetic Inductance Detectors". PhD thesis. 2005. DOI: 10.7907/GZ72-V784.

[57] Jonas Zmuidzinas. "Superconducting Microresonators: Physics and Applications". In: *Annual Review of Condensed Matter Physics* 3.1 (Mar. 2012), pp. 169–214. ISSN: 1947-5454. DOI: 10.1146/annurev-conmatphys-020911-125022. URL: http://www.annualreviews.org/doi/10.1146/annurev-conmatphys-020911-125022.

[58] Peter Barry. "On the development of SuperSpec: a fully integrated on-chip spectrometer for far-infrared astronomy". PhD thesis. 2014. URL: http://orca.cf.ac.uk/id/eprint/71562.

[59] Josie Parrianen. "Study of the limits of single-photon detection in lumped element kinetic inductance detectors". PhD thesis. 2018. URL: http://orca.cf.ac.uk/id/eprint/123522.

[60] C Kittel. *Introduction to Solid State Physics*. Wiley, 2004. URL: https://www.wiley.com/en-gb/Introduction+to+Solid+State+Physics%2C+8th+Edition-p-9780471415268.

[61] M Tinkham. *Introduction to Superconductivity*. Science, 2004. URL: https://www.sciencedirect.com/book/9780080216515/introduction-to-superconductivity.

[62] Leon N. Cooper. *Bound electron pairs in a degenerate fermi gas [1]*. Nov. 1956. DOI: 10.1103/PhysRev.104.1189. URL: https://journals.aps.org/pr/abstract/10.1103/PhysRev.104.1189.

[63] F London and H London. "The electromagnetic equations of the supraconductor". In: *Proceedings of the Royal Society of London. Series A - Mathematical and Physical Sciences* 149.866 (Mar. 1935), pp. 71–88. ISSN: 0080-4630. DOI: 10.1098/rspa.1935.0048. URL: https://royalsocietypublishing.org/doi/10.1098/rspa.1935.0048.

[64] John Bardeen. "Two-fluid model of superconductivity". In: *Physical Review Letters* 1.11 (Dec. 1958), pp. 399–400. ISSN: 00319007. DOI: 10.1103/PhysRevLett.1.399. URL: https://journals.aps.org/prl/abstract/10.1103/PhysRevLett.1.399.

[65] D. C. Mattis and J. Bardeen. "Theory of the anomalous skin effect in normal and superconducting metals". In: *Physical Review* 111.2 (July 1958), pp. 412–417. ISSN: 0031899X. DOI: 10.1103/PhysRev.111.412. URL: https://journals.aps.org/pr/abstract/10.1103/PhysRev.111.412.

[66] J. Bardeen, L. N. Cooper, and J. R. Schrieffer. "Theory of superconductivity". In: *Physical Review* 108.5 (Dec. 1957), pp. 1175–1204. ISSN: 0031899X. DOI:

10.1103/PhysRev.108.1175. URL: https://journals.aps.org/pr/abstract/10.1103/PhysRev.108.1175.

[67] Bernhard Mühlschlegel. "Die thermodynamischen Funktionen des Supraleiters". In: *Zeitschrift für Physik* 155.3 (1959), pp. 313–327. ISSN: 00443328. DOI: 10.1007/BF01332932. URL: https://link.springer.com/article/10.1007/BF01332932.

[68] Jiansong Gao et al. "Equivalence of the effects on the complex conductivity of superconductor due to temperature change and external pair breaking". In: *Journal of Low Temperature Physics* 151.1-2 PART 1 (Apr. 2008), pp. 557–563. ISSN: 00222291. DOI: 10.1007/s10909-007-9688-z. URL: https://link.springer.com/article/10.1007/s10909-007-9688-z.

[69] Simon Doyle. "Lumped element Kinetic Inductance Detectors". PhD thesis. 2008. URL: http://orca.cf.ac.uk/id/eprint/54728.

[70] S. B. Kaplan et al. "Quasiparticle and phonon lifetimes in superconductors". In: *Physical Review B* 14.11 (Dec. 1976), pp. 4854–4873. ISSN: 01631829. DOI: 10.1103/PhysRevB.14.4854. URL: https://journals.aps.org/prb/abstract/10.1103/PhysRevB.14.4854.

[71] P.J. De Visser. "Quasiparticle dynamics in aluminium superconducting microwave resonators". PhD thesis. 2014. URL: https://repository.tudelft.nl/islandora/object/uuid%3Aeae4c9fc-f90d-4c12-a878-8428ee4adb4c.

[72] D Pozar. *Microwave Engineering*. 4th. Wiley, 2004. URL: https://www.wiley.com/en-gb/Microwave+Engineering%2C+4th+Edition-p-9781118298138.

[73] J Rautio. *Sonnet Software*. URL: https://www.sonnetsoftware.com/.

[74] Charles R. Harris et al. *Array programming with NumPy*. Sept. 2020. DOI: 10.1038/s41586-020-2649-2. URL: https://doi.org/10.1038/s41586-020-2649-2.

[75] John D. Hunter. "Matplotlib: A 2D graphics environment". In: *Computing in Science and Engineering* 9.3 (2007), pp. 90–95. ISSN: 15219615. DOI: 10.1109/MCSE.2007.55.

[76] Pauli Virtanen et al. "SciPy 1.0: fundamental algorithms for scientific computing in Python". In: *Nature Methods* 17.3 (Mar. 2020), pp. 261–272. ISSN: 15487105. DOI: 10.1038/s41592-019-0686-2. URL: https://doi.org/10.1038/s41592-019-0686-2.

[77] P. D. Mauskopf et al. "Photon-noise limited performance in aluminum LEKIDs". In: *Journal of Low Temperature Physics*. Vol. 176. 3-4. Springer New York LLC, Jan. 2014, pp. 545–552. DOI: 10.1007/s10909-013-1069-1. URL: https://link.springer.com/article/10.1007/s10909-013-1069-1.

[78] C. M. Wilson, L. Frunzio, and D. E. Prober. "Time-Resolved Measurements of Thermodynamic Fluctuations of the Particle Number in a Nondegenerate Fermi Gas". In: *Physical Review Letters* 87.6 (Aug. 2001), pp. 67004–1. ISSN: 10797114. DOI: 10.1103/PhysRevLett.87.067004. URL: https://journals.aps.org/prl/abstract/10.1103/PhysRevLett.87.067004.

[79] P. J. De Visser et al. "Generation-recombination noise: The fundamental sensitivity limit for kinetic inductance detectors". In: *Journal of Low Temperature Physics*. Vol. 167. 3-4. Springer, June 2012, pp. 335–340. DOI: 10.1007/s10909-012-0519-5. URL: https://link.springer.com/article/10.1007/s10909-012-0519-5.

[80] *KLayout Layout Viewer And Editor*. URL: https://www.klayout.de/.

[81] Q. Y. Tang et al. "Fabrication of antenna-coupled KID array for Cosmic Microwave Background detection". In: *Journal of Low Temperature Physics* 193.3-4 (Oct. 2017), pp. 149–156. DOI: 10.1007/s10909-018-1941-0. URL: http://arxiv.org/abs/1710.11255%20http://dx.doi.org/10.1007/s10909-018-1941-0.

[82] G Teleberg. "Sorption-cooled miniature dilution refrigerators for astrophysical applications". PhD thesis. 2006. URL: http://orca.cf.ac.uk/56123/.

[83] L J Swenson et al. *Operation of a titanium nitride superconducting microresonator detector in the nonlinear regime*. Tech. rep. 2013.

[84] M. S. Khalil et al. "An analysis method for asymmetric resonator transmission applied to superconducting devices". In: *Journal of Applied Physics* 111.5

(Aug. 2011). DOI: 10.1063/1.3692073. URL: http://arxiv.org/abs/1108.3117%20http://dx.doi.org/10.1063/1.3692073.

[85] C. R. H. McRae et al. "Materials loss measurements using superconducting microwave resonators". In: *Review of Scientific Instruments* 91.9 (Sept. 2020), p. 091101. ISSN: 0034-6748. DOI: 10.1063/5.0017378. URL: http://aip.scitation.org/doi/10.1063/5.0017378.

[86] J. Burnett et al. "Slow noise processes in superconducting resonators". In: *Physical Review B - Condensed Matter and Materials Physics* 87.14 (Apr. 2013), p. 140501. ISSN: 10980121. DOI: 10.1103/PhysRevB.87.140501. URL: https://journals.aps.org/prb/abstract/10.1103/PhysRevB.87.140501.

[87] J. Baselmans et al. "Noise and sensitivity of aluminum kinetic inductance detectors for sub-mm astronomy". In: *Journal of Low Temperature Physics* 151.1-2 PART 1 (Apr. 2008), pp. 524–529. ISSN: 00222291. DOI: 10.1007/s10909-007-9684-3. URL: https://link.springer.com/article/10.1007/s10909-007-9684-3.

[88] *LAMBDA - CMB Experiments*. URL: https://lambda.gsfc.nasa.gov/product/expt/.

[89] S. W. Henderson et al. "Advanced ACTPol Cryogenic Detector Arrays and Readout". In: *Journal of Low Temperature Physics* 184.3-4 (Aug. 2016), pp. 772–779. ISSN: 15737357. DOI: 10.1007/s10909-016-1575-z. URL: https://link.springer.com/article/10.1007/s10909-016-1575-z.

[90] Thomas Essinger-Hileman et al. "CLASS: the cosmology large angular scale surveyor". In: *Millimeter, Submillimeter, and Far-Infrared Detectors and Instrumentation for Astronomy VII*. Ed. by Wayne S. Holland and Jonas Zmuidzinas. Vol. 9153. SPIE, July 2014, p. 91531I. DOI: 10.1117/12.2056701. URL: http://proceedings.spiedigitallibrary.org/proceeding.aspx?doi=10.1117/12.2056701.

[91] Aritoki Suzuki et al. "Multichroic dual-polarization bolometric detectors for studies of the cosmic microwave background". In: *23rd International Symposium on Space Terahertz Technology 2012, ISSTT 2012*. Ed. by Wayne

S. Holland. Vol. 8452. International Society for Optics and Photonics, Oct. 2012, 84523H. DOI: 10.1117/12.924869. URL: http://proceedings.spiedigitallibrary.org/proceeding.aspx?doi=10.1117/12.924869.

[92] Roger OBrient et al. "A Dual-polarized Broadband Planar Antenna and Channelizing Filter Bank for Millimeter Wavelengths". In: *Applied Physics Letters* 102.6 (Feb. 2013). DOI: 10.1063/1.4791692. URL: http://arxiv.org/abs/1302.0325%20http://dx.doi.org/10.1063/1.4791692.